



**SAARLAND
UNIVERSITY**

Department of Neuroanatomy,
Theoretical Medicine and Biosciences,
Faculty of Medicine
Saarland University, Homburg (Saar)

**DYSREGULATION OF CALCIUM SIGNALING IN
PHOTORECEPTOR SYNAPSES OF EAE MICE, A
MULTIPLE SCLEROSIS ANIMAL MODEL**

A thesis submitted to the Faculty of Medicine in fulfilment of the requirements
for the degree of
Doctor of Philosophy (PhD)

Submitted by
Amrita Mukherjee
Germany, 2019

Supervisor:

Co-supervisor:

Declaration

I hereby declare that the Ph.D. thesis entitled “**Dysregulation of calcium signaling in photoreceptor synapses of EAE mice, a multiple sclerosis animal model**” is a presentation of my original research work. All external sources of information have been acknowledged. No portion of this thesis work has been submitted in support of any other degree or qualification.

Homburg,

28.2.2019

AMRITA MUKHERJEE

*Dedicated to my parents,
husband,
brother
and my in-laws*

Acknowledgements

I truly appreciate the opportunity to express my gratitude to all those who had directly and indirectly contributed to completion of this thesis. Starting with my family, first of all I would like to thank my mother, Late Dr. Jaba Mukherjee for making my dream of achieving a doctoral degree, her dream. I also treasure my father, Mr. Aniruddha Mukherjee's support, encouragement and understanding for my doctoral work especially after my mother's demise. I am also extremely grateful to my father in law, Mr. Manoj Kumar Saha Roy for his moral support and especially to my sister in law, Dr. Madhumita Basu for her profound unwavering belief in me. Finally, I would like to thank the most important person in my life, my husband, Dr. Rishiraj Saha Roy who has always been by my side and has inspired me and helped me in every possible way during my PhD. Last of all, I would like to express my love for my brother, Arnab whose very presence fills me with strength and positivity.

Besides my family, I am grateful to my PhD supervisor Prof. Dr. med. Frank Schmitz for granting me the opportunity to do my PhD work in his lab and guiding me through it at every step. I would also like to extend my thanks to Prof. Dr. Jens Rettig and Prof. Dr. Dieter Brun's for their insightful comments and discussions during the synapse club seminars. Additionally, I would like to acknowledge Prof. Dr. Veit Flockerzi and his lab members for supplying me with valuable antibodies for my PhD work. I express my gratitude to Dr. Elmar Krause for acclimatizing me with the SR-SIM, which proved instrumental to my PhD work. I would also like to thank Dr. Martin Jung for generating the invaluable MOG₃₅₋₅₅ peptide and the polyclonal antibodies.

Coming to my lab members, I would like to first thank Dr. Karin Schwarz for her contributions at various stages of my PhD work (EAE induction in mice and retinal embedding preparation among various other things). I am also thankful for her helpful suggestions during the lab meetings. I would like to further extend my gratitude to my senior lab members Dr. Rashmi Katiyar, Dr. Mayur Dembla, Dr. Ekta Dembla and Dr. Shweta Suiwal for their suggestions, scientific discussions and help in every day lab work. Special thanks are also due to Soni Shankhwar and Ajay Kesharwani for providing a positive, friendly atmosphere of work in the laboratory.

Last but not the least; I would like to thank all the technicians for their efficient and constant support: Sylvia Brundaler for her incredible lab management skills, Sabine Schmidt and Ines Krüger for their help at the animal house and beyond and Gabi Kiefer for providing me with innumerable sections for immunofluorescence experiments.

Table of Contents

SUMMARY.....	1
ZUSAMMENFASSUNG.....	3
1 INTRODUCTION.....	6
1.1 Anatomy of the mammalian eye	6
1.2 Retinal structure and function.....	7
1.3 Retinal synaptic pathways.....	10
1.4 Morphology and function of ribbon synapses.....	11
1.5 Molecular composition of ribbon synapses.....	15
1.6 Rab3 interacting molecules in photoreceptor synapses.....	17
1.7 Voltage gated Ca ²⁺ channels in photoreceptor synapses.....	18
1.8 Key players in maintenance of calcium homeostasis in photoreceptor synapses	21
1.9 Multiple sclerosis and its retinal pathology	23
1.10 Experimental autoimmune encephalitis as a multiple sclerosis model	25
1.11 Retinal pathology in experimental autoimmune encephalitis	29
1.12 Working hypothesis	30
2 MATERIALS AND METHODS.....	31
2.1 Materials	31
2.1.1 Antibodies.....	31
2.1.1.1 Primary antibodies use in immunofluorescence assays	31
2.1.1.2 Secondary antibodies used in immunofluorescence assays	32
2.1.1.3 Primary antibodies used in Western blot assays	32
2.1.1.4 Secondary antibodies used in Western blot assays.....	33
2.1.2 Reagents and chemicals.....	33
2.1.3 Cell line.....	35
2.1.4 Plasmid vectors (previously cloned).....	35
2.1.5 Buffers and media	36
2.1.6 Laboratory instruments and consumable materials	40
2.2 Methods.....	41
2.2.1 Induction of experimental autoimmune Encephalitis (EAE)	41
2.2.2 Isolation of mouse retina and initial processings	42
2.2.3 Light microscopy	42

2.2.3.1	Embedding of Epon resin sections	42
2.2.3.2	Immunolabeling of 0.5 and 1.5 μm thin resin sections	42
2.2.3.3	Immunolabeling with primary antibodies generated in same species	43
2.2.3.4	Blocking of antibodies (preabsorption experiments)	43
2.2.3.5	Confocal laser scanning microscopy	44
2.2.3.6	Super-resolution structured illumination microscopy (SR-SIM)	45
2.2.4	Western blot assays	46
2.2.4.1	Protein quantification	46
2.2.4.2	SDS PAGE	47
2.2.5	Calcium imaging of retinal slices of CFA and MOG/CFA injected mice	48
2.2.5.1	Making of retinal slices	48
2.2.5.2	Loading of retinal slices with FURA2-AM	49
2.2.5.3	Baseline fluorescence and Ca^{2+} influx measurement with FURA2-AM	49
2.2.5.4	Analyses of FURA2-AM baseline fluorescence and imaging on depolarization	50
2.2.6	Overexpression in HEK293T cells to check antibody specificity	51
2.2.6.1	Plasmid purification	51
2.2.6.2	Sub-culturing of HEK293T cells	52
2.2.6.3	Transfection of HEK293T cells	52
2.2.6.4	Western blot of transfected HEK293T cells	52
3	RESULTS	54
3.1	$\text{Ca}_v1.4 \alpha 1\text{F}$ expression in photoreceptor synapses of MOG/CFA-injected (EAE) and CFA-injected (control) mice	54
3.1.1	$\text{Ca}_v1.4$ alpha C-term immunolabeling and analyses	54
3.1.2	Verification of $\text{Ca}_v1.4\alpha$ data with a second independent antibody ' $\text{Ca}_v1.4\alpha$ N-term' ...	56
3.1.3	High resolution analyses of $\text{Ca}_v1.4$ alpha punctas by super resolution structured illumination microscopy (SR-SIM)	57
3.1.4	Western blot analyses of $\text{Ca}_v1.4\alpha$ expression in EAE and control retinas	58
3.2	$\text{Ca}_v\beta 2$ expression in photoreceptor synapses of MOG/CFA-injected (EAE) and CFA-injected (control) mice	60
3.2.1	Immunolabeling and quantification of $\text{Ca}_v\beta 2$ antibody (No.1) in EAE retina	60
3.2.2	Second independent $\text{Ca}_v\beta 2$ antibody (No.2) corroborates previous $\text{Ca}_v\beta 2$ data	62
3.2.3	High resolution analyses of contour length of $\text{Ca}_v\beta 2$ punctas by super resolution structured illumination microscopy (SR-SIM)	63

3.2.4	Western blot analyses of $Ca_v\beta 2$ expression in EAE and control mice retinas	64
3.3	Evaluation of depolarization-evoked Ca^{2+} influx in EAE mice retina	65
3.3.1	Depolarization-evoked Ca^{2+} influx measurement on day9 after induction	66
3.3.2	Analysis of depolarization-evoked Ca^{2+} influx at earlier time points (days 7 and 8 after immunization).....	67
3.3.3	Comparing amplitudes and time constants of MOG/CFA depolarization-evoked Ca^{2+} influx responses over days 7, 8 and 9.....	69
3.3.4	Confirmation of the results with a commercially available EAE injection system.....	70
3.4	Analyzing RIMs, main regulators of Ca_v channels in EAE photoreceptor terminals.....	74
3.4.1	Coimmunolabeling of EAE retinal synapses with antibodies against RIM2 and PSD95..	74
3.4.2	Verifying reduced immunofluorescence of RIM2 (4F7) with a second RIM2 antibody... ..	76
3.4.3	Western blot analysis of RIMs in EAE mice retinal lysates	78
3.5	Comparing intracellular calcium concentration in retinal slices of EAE and control mice ..	79
3.6	Pre-clinical effect of EAE on calcium efflux mechanism in mice photoreceptor synapses..	82
3.7	Testing of specificity of antibodies	85
3.7.1	$Ca_v1.4$ alpha antibodies	85
3.7.2	$Ca_v\beta 2$ antibodies	86
3.7.3	RIM2 mouse monoclonal antibodies	88
3.7.4	RIM1,2 rabbit polyclonal antibody.....	90
4	DISCUSSION.....	91
5	REFERENCES	98
6	LIST OF FIGURES.....	117
7	LIST OF ABBREVIATIONS.....	120
8	CURRICULUM VITAE	124

SUMMARY

Ribbon synapses are specialized chemical synapses. Unlike conventional chemical synapses, they remain continuously active, responding tonically in a graded fashion to varying strengths of the relevant stimuli, over a broad range of intensities. Sustained continuous vesicle release in ribbon synapses is ascribed to a special electron-dense presynaptic structure, called the ribbon. In photoreceptor ribbon synapses light-induced changes in membrane potential are transformed into graded continuous neurotransmitter release.

The main building component of the synaptic ribbon is the protein RIBEYE. The ribbon is anchored at the active zone and associated with many release-ready vesicles. Depolarization-induced opening of Ca_v channels, at the active zone, triggers synaptic vesicle exocytosis and the subsequent release of neurotransmitter contents into the synaptic cleft. Various active zone proteins, including the RIMs, control Ca_v channel localization and function. ER-resident SERCA pump and plasma membrane-resident Ca^{2+} ATPases (PMCAs) play a crucial role in maintaining Ca^{2+} homeostasis in the presynaptic terminal by extruding elevated Ca^{2+} levels from the cytosol in an ATP-dependent manner. Ca^{2+} homeostasis is important for controlling the basal sustained neurotransmitter release at ribbon synapses.

Multiple sclerosis (MS) is a severe neuroinflammatory, degenerative disease of the central nervous system (CNS), in which the immune system attacks the myelin sheath of myelinated axons, leading to demyelination. However, the damage is not restricted to white matter alone. Evidences of early grey matter cortical lesions in the brain and retinal layer thinning indicate a more complex immunopathology. The retina is also an unmyelinated tissue. Experimental autoimmune encephalitis (EAE), a well established mouse model of MS, shows retinal ganglion cell death and retinal nerve fibre layer (RNFL) thinning in its preclinical stage. Interestingly Dembla et al., 2018 observed a significantly decreased synaptic vesicle cycling in photoreceptor synapses in EAE mice at a pre-clinical phase. Since Ca^{2+} ions play a crucial role in synaptic vesicle cycling, I analysed for possible malfunctions in Ca^{2+} signaling in photoreceptor ribbon synapses of EAE mice in its preclinical stage.

Immunofluorescence assay of $Ca_v1.4 \alpha1F$, the pore forming subunit, show decreased fluorescence intensity at photoreceptor synapses in the OPL of MOG/CFA (EAE) mice retinal sections in comparison to control sections with no significant reduction in the number of punctas in a defined length of the OPL. However, the average size of the Ca_v punctas in EAE was significantly smaller as judged by super-resolution structured illumination microscopy (SR-SIM). Similar results were also

SUMMARY

obtained for the β subunits of $Ca_v1.4$ channels. These findings indicate that although the number of Ca_v channel clusters remain unaltered in EAE preclinical phase, the number of channels in each cluster decrease. Western blot analyses using CFA and MOG/CFA mice retinal lysates showed similar levels of $\alpha1F$ protein in the two groups, implying that it is clustering of the $Ca_v1.4$ channels, which is primarily affected and not the total expression of the Ca_v protein. Interestingly $Ca_v\beta2$ shows a significant reduction in EAE in Western blot analyses. Recent studies show that β subunits can also operate as a separate entity independent of the other Ca_v subunits, which might explain the different changes of $Ca_v1.4$ alpha and beta relative to each other. Immunofluorescence assay for RIMs that are crucially important for Ca_v channel localization and regulation showed a similar finding as the $Ca_v1.4$ proteins. RIM2 immunosignals (at the active zone of photoreceptor synapses) exhibited a highly significant reduction in their intensities in MOG/CFA photoreceptor synapses with the count for the number of punctas remaining unchanged compared to the control (CFA). Western blot analyses also exhibited a highly significant loss in total protein content of RIMs 1 and 2 in EAE retinal lysates. Thus, Ca_v channels and their regulators, RIMs, both are found to be adversely affected in photoreceptor synapses of EAE mice at a preclinical stage.

Ca^{2+} influx measurements in CFA and MOG/CFA retinal slices using FURA2-AM, showed that depolarization-evoked Ca^{2+} influx at the OPL in MOG/CFA slices was reduced in amplitude and slowed in kinetics of Ca^{2+} increase. During my Fura2 imaging studies, I found additional alterations of Ca^{2+} homeostasis. The basal Ca^{2+} concentrations were elevated in preclinical EAE mice photoreceptor synapses. To find possible mechanisms for the increased basal Ca^{2+} , I analyzed key components of Ca^{2+} extrusion mechanisms in photoreceptor terminals. PMCA2, the more efficient PMCA isoform with higher Ca^{2+} affinity, showed a significant reduction in its synaptic expression in EAE retina. The decreased synaptic expression of PMCA2 could result in a decreased cytosolic Ca^{2+} clearance and thus to the observed increase in basal Ca^{2+} . PMCA1 and another protein PSD95, a photoreceptor presynaptic marker for synaptic integrity, remained unaltered in immunofluorescence studies. Thus, in preclinical phase of EAE, synaptic Ca^{2+} signaling is affected at various levels and could contribute to the recently discovered dysfunctions of synaptic vesicle cycling.

ZUSAMMENFASSUNG

Ribbonsynapsen sind spezialisierte chemische Synapsen. Im Gegensatz zu herkömmlichen chemischen Synapsen sind sie kontinuierlich aktiv und reagieren über eine enorme Bandbreite an Reizintensitäten mit graduierten Antworten. Die Fähigkeit zur kontinuierliche Vesikelfreisetzung der Ribbonsynapsen wird einer speziellen elektronendichten präsynaptischen Struktur, dem sogenannten Ribbon, zugeschrieben. In Photorezeptorribbonsynapsen werden lichtinduzierte Änderungen des Membranpotentials in abgestufte kontinuierliche Neurotransmitterfreisetzung umgewandelt.

Der Hauptbestandteil des Ribbons ist das Protein RIBEYE. Der Ribbon ist in der aktiven Zone verankert und mit vielen, Freisetzungskompetenten Vesikeln verbunden. Die durch Depolarisation induzierte Öffnung von Cav- Kanälen in der aktiven Zone löst die Exozytose aus und setzt Neurotransmitter aus den synaptischen Vesikeln in den synaptischen Spalt frei. Verschiedene Proteine der aktiven Zonen, einschließlich der RIM-Proteine, steuern die Lokalisierung und Funktion dieser Ca_v Kanälen. Weiterhin spielen eine am ER-befindliche SERCA-Pumpe und in der Plasmamembran lokalisierte Ca^{2+} -ATPasen (PMCA's) eine entscheidende Rolle bei der Aufrechterhaltung der Ca^{2+} -Homöostase in der präsynaptischen Terminale. PMCA's schleusen Ca^{2+} ATP-abhängig aus der präsynaptischen Terminale. Die Aufrechterhaltung der Ca^{2+} Homöostase ist für die Steuerung der basalen verzögerten Freisetzung an den Ribbonsynapsen wichtig.

Die Multiple-Sklerose (MS) ist im Wesentlichen eine neuroinflammatorische, degenerative Erkrankung des Zentralnervensystems (ZNS), bei der das Immunsystem die Myelinscheide von Axonen angreift, was zu der Demyelinisierung der Axone führt. Der Schaden ist jedoch nicht ausschließlich auf die weiße Substanz des ZNS beschränkt. Wachsende Hinweise auf frühe Schädigungen der grauen Substanz, wie z.B. kortikale Gehirnläsionen oder die Dickenabnahme der Netzhautschichten deuten auf eine deutlich komplexere Immunopathologie hin. Die Netzhaut ist ein nicht-myelinisierter Abschnitt des ZNS. Die experimentelle autoimmune Encephalomyelitis (EAE), ein gut etabliertes Mausmodell für MS, zeigt das Absterben retinaler Ganglienzellen und das Ausdünnen der RNFL (retinalen Nervenfaserschicht) bereits in der präklinischen Phase. Interessanterweise beobachteten Dembla et al., 2018, einen signifikant verringerten synaptischen Vesikelzyklus in Photorezeptor-Synapsen von EAE-Mäusen in der vorklinischen Phase. Da Ca^{2+} Ionen eine entscheidende Rolle beim synaptischen Vesikelzyklus spielen, untersuchte ich mögliche Störungen des Ca^{2+} Signals in Photorezeptor-Synapsen von EAE-Mäusen im präklinischen Stadium.

ZUSAMMENFASSUNG

Immunfluoreszenzuntersuchungen der porenbildenden Kanaluntereinheit $Ca_v1.4 \alpha1F$ zeigten verringerte Immunsignale in Netzhautschnitten von behandelten (MOG/CFA) im Vergleich zu solchen von Kontrolltieren (CFA alleine), wobei die Anzahl der Immunsignale je gegebener Länge OPL unverändert war. Wie durch hochauflösende strukturierte Beleuchtungsmikroskopie (SR-SIM) gezeigt werden konnte, war die durchschnittliche Größe der Ca_v Immunsignale unter EAE-Bedingungen signifikant geringer, als die der Kontrolltiere. Ähnliche Ergebnisse wurden auch für die β Untereinheiten der $Ca_v1.4$ -Kanäle erhalten. Diese Ergebnisse zeigen, dass die Anzahl der Ca_v Kanal-Cluster in der präklinischen Phase der EAE unverändert bleibt, die Anzahl der Kanäle in dem Cluster jedoch abnimmt. Western-Blot-Analysen von Retina-Lysaten der CFA und MOG/CFA-Mäusen zeigten vergleichbare Mengen an $\alpha1F$ -Protein in den beiden Gruppen. Dies deutet darauf hin, dass weniger die Proteinexpression (gleiche Menge an Gesamtprotein) als vielmehr die Clusterbildung der $Ca_v1.4$ Kanäle betroffen ist. Im Gegensatz dazu zeigten Western Blot Analysen der $Ca_v\beta2$ -Untereinheit eine deutlich reduzierte Proteinmenge unter EAE-Bedingungen. Neuere Studien zeigen, dass die $Ca_v\beta2$ -Untereinheiten auch als eigenständige Einheit unabhängig von den anderen Ca_v -Untereinheiten, arbeiten kann, was möglicherweise die Unterschiede in der Gesamtproteingehalt von $Ca_v1.4\alpha$ und $Ca_v\beta2$ relativ zueinander unter EAE-Bedingungen erklärt. Immunfluoreszenzuntersuchungen der RIM Proteine, die für die Lokalisierung und Regulation von Ca_v Kanälen von entscheidender Bedeutung sind, führten zu ähnliche Ergebnisse wie für die $Ca_v1.4$ -Proteine gezeigt. RIM2-Immunsignale (in der aktiven Zone der Photorezeptor-Synapsen) zeigten eine sehr signifikante Verringerung ihrer Intensitäten in MOG/CFA-Photorezeptor-Synapsen, wobei die Anzahl der Signale gegenüber der Kontrolle (CFA) unverändert blieb. Western-Blot-Analysen zeigten eine sehr deutliche Reduktion des Gesamtproteingehalts an RIMs 1 und 2 in EAE-Retina-Lysaten. Somit konnte ich zeigen, dass sowohl die Ca_v Kanäle als auch ihre Regulatoren, die RIMs, beide bereits in der vorklinischen EAE Phase nachteilig beeinflusst werden.

Ca^{2+} -Messungen mittels FURA2AM in CFA- und MOG/CFA-Retina-Schnitten zeigten, dass der durch Depolarisation hervorgerufene Ca^{2+} -Einstrom in der OPL von MOG/CFA Retina-Schnitten in der Amplitude verringert war und die Kinetik des Ca^{2+} Anstiegs reduziert war. Während meiner Fura2-Untersuchungen fand ich zusätzliche Veränderungen der Ca^{2+} -Homöostase. Die basalen Ca^{2+} -konzentrationen waren bei präklinischen EAE-Mäuse-Photorezeptor-Synapsen erhöht. Um mögliche Mechanismen für das erhöhte Basal Ca^{2+} zu finden, analysierte ich Schlüsselkomponenten der Ca^{2+} -Extrusionsmechanismen in Fotorezeptorendgeräten. PMCA2, die effizientere PMCA-Isoform mit höherer Ca^{2+} Affinität, zeigte eine signifikante Reduktion der synaptischen Expression in der EAE-Retina. Die verminderte synaptische Expression von PMCA2 könnte zu einer

ZUSAMMENFASSUNG

verminderten zytosolischen Ca^{2+} -Clearance und damit zu einer beobachteten Erhöhung des Basal Ca^{2+} führen. PMCA1 und ein anderes Protein PSD95, ein präsynaptischer Photorezeptor-Marker für die synaptische Integrität, blieb in Immunfluoreszenzstudien unverändert. In der präklinischen Phase der EAE können die gestörten Ca^{2+} -Signale zu den kürzlich entdeckten Funktionsstörungen des synaptischen Vesikelzyklus beitragen.

1 INTRODUCTION

Visual perception is one of the primary sensory functions which detects light and processes it to furnish us with the gift of sight. It provides us with a wealth of information about our surroundings like its texture, color, depth and context. The eye receives light and transmits it to the retina. A circuit of neuronal cells in the retina processes it into biological signals and sends them to the visual processing areas of the brain creating the perception of vision (Kolb, 2007; Willoughby et al., 2010).

1.1 Anatomy of the mammalian eye

Eye, the prime organ of vision, is one of the most complex organs of the body. It is a three-layered fluid filled tissue: the outer region consisting of cornea and sclera, the middle layer of iris, ciliary body and choroid, and retina making up the innermost layer (Fig. 1).

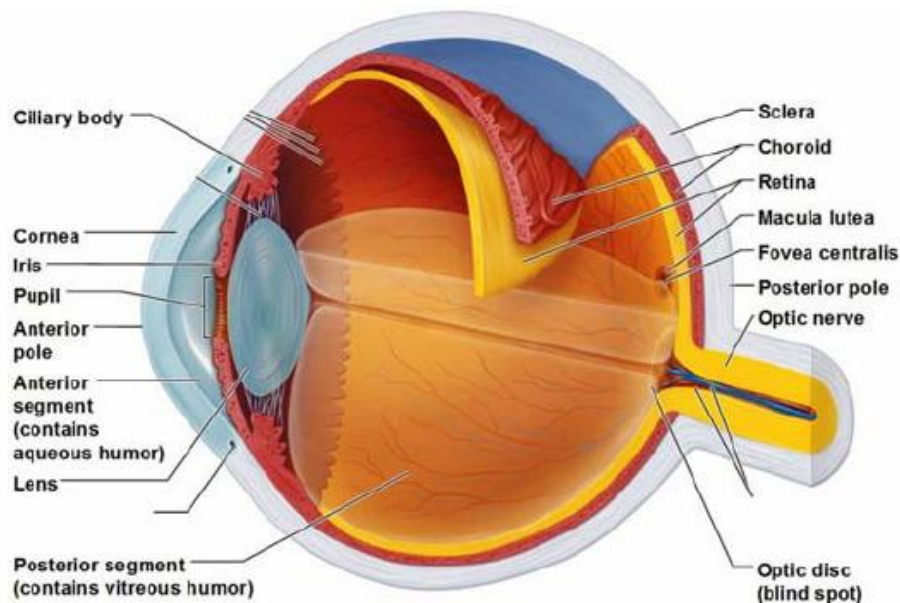


Figure 1: Section through the adult human eye

Adapted from Tahoun, 2015.

Besides acting as a protective outer layer, the cornea refracts and transmits light onto the retina via the lens. The iris in turn constricts/dilates the pupil controlling the amount of light reaching the retina in bright/dim light. The retina despite its peripheral location is actually an extended part of the central nervous system. The process of conversion of light to vision through the retina comprises of three basic steps: reception, transduction and coding. In reception the retinal photoreceptor cells receive and absorb photons of light. Subsequently, they also start the process of transduction by

INTRODUCTION

converting electromagnetic nature of light energy into electrochemical form of nerve impulses. Finally, the retinal neuronal circuit codes the spatial and temporal information of the visual signals into nerve impulses and transmits them to the primary visual cortex of the cerebrum via the optic nerve (Kolb, 1995; Purves, et al., 2001).

1.2 Retinal structure and function

The mature mammalian retina has two distinct components: the retinal pigmented epithelium and the neural retina. The retinal neuronal cells are organized in layers from the photoreceptors responsible for receiving light to the ganglion cells that transmit the visual information to the brain. In the vertebrate retina five major types of neuronal cells (i.e. photoreceptors, bipolar cells, amacrine cells, horizontal cells, and ganglion cells) are arranged in a fashion such that the cell bodies and the neuronal processes are in an alternating sequence. The cell bodies are located in the outer nuclear, inner nuclear and ganglion cell layers while the dendritic processes and synaptic contacts are located in the outer plexiform and inner plexiform layers (OPL and IPL respectively) (Dowling & Werblin, 1971; Kolb, 1995) (Fig 2).

Visual perception begins when photons are detected by the rod and cone photoreceptors of the vertebrate retina. Photoexcited visual pigments of the photoreceptor cells initiate a signal transduction cascade called the phototransduction. The process results into consequent hyperpolarization of the cell membrane and an electrochemical signal cascade (Yau & Hardie, 2009). In photoreceptors, the membrane potential ranges from around -40 mV in darkness, to -60 or -70 mV in bright light (Barnes & Kelly, 2002). The bipolar, horizontal and amacrine cells with their cell bodies lying in the inner nuclear layer (INL) just next to the photoreceptor terminals receive and transmit the processed information to the ganglion cells. The retinal ganglion cells (RGCs) are the output neurons of the retina (Fig. 2). Their projecting axons transmit the information to specific parts of the brain via the optic nerve allowing for extraction of features from the visual field such as luminance, contrast, color, and movement.

INTRODUCTION

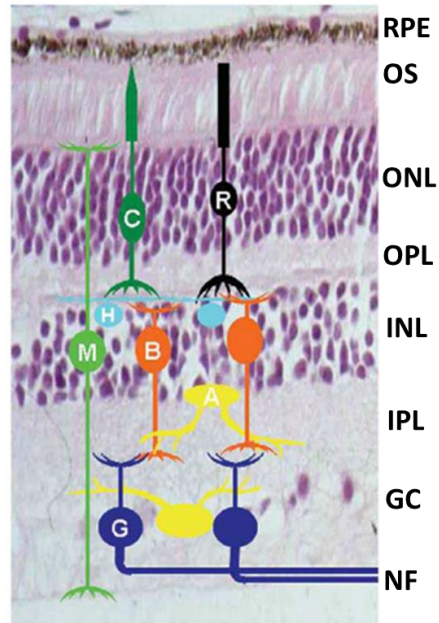


Figure 2: Histological image and schematic diagram of retinal layers of an adult mammalian retina

Abbreviations: a-amacrine neurons, b-bipolar neurons, c-cone photoreceptors, g-ganglion cell, gc-ganglion cell layer, h-horizontal neurons, inl-inner nuclear layer, ipl-inner plexiform layers, m-müller glial cell, nf-nerve fiber layer, onl-outer nuclear layer, os-outer segments, r-rod photoreceptors, rpe-retinal pigment epithelium. Adapted from (Wallace, 2011).

Besides the retinal neurons there also exist the Müller glial cells, with its cell bodies in the INL and its processes interspersing the entire retina. The Müller cells provide support to the retina and also help to maintain a homeostatic environment (Fig. 2). Furthermore the retina is also known to comprise of astrocytes, microglia and cells of retinal vasculature. Many of the retinal neurons also have a number of morphological and functional subtypes (Wohrer, 2008; Stenkamp, 2015).

Phototransduction takes place in the outer segments of photoreceptors where photons absorbed are converted into electrical responses and relayed onto adjoining neural layers across synapses. The outer segments are rich in visual pigments (rhodopsin in rods and cone opsins in cones) and signaling proteins (Shichida & Matsuyama, 2009). In all vertebrate and invertebrate photoreceptors phototransduction is based on a heterotrimeric G protein signaling cascade. Photoactivation of rhodopsins lead to activation of the G-protein transducin. Activated GTP bound α subunit of transducin in turn activates phosphodiesterase (PDE). Activated PDE hydrolyzes cGMP to 5'GMP which leads to a subsequent decrease in cGMP concentration. As a result, cGMP-sensitive cation channels in the plasma membrane close, hyperpolarizing the cell. This hyperpolarization causes the voltage gated calcium channels in the photoreceptor synaptic terminals to close bringing about a transient decrease in glutamate neurotransmitter release. Decrease in the concentration of

INTRODUCTION

glutamate release signals the number of photons absorbed by the photoreceptors to the rest of the visual system (Fig.3).

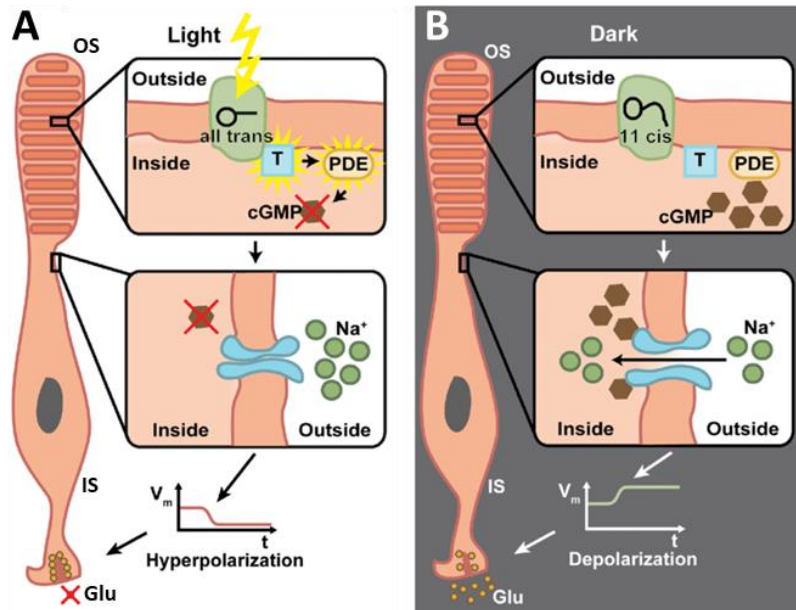


Figure 3: Phototransduction cascade in vertebrate rod photoreceptors

(A) Upon light absorption in the rod photoreceptor outer segments, conformational change of 11-cis retinal to all-trans retinal releases rhodopsin. Free rhodopsin activates transducin, which in turn activates PDE. Activated PDE hydrolyzes cGMP to 5'-GMP effectively lowering cGMP concentration (upper panel). This leads to the closure of cGMP mediated cation channels (middle panel). Thus, the inner segments are hyperpolarized and glutamate exocytosis from the photoreceptor terminals is stopped (lower panel). (B) In dark, regenerated rhodopsin remains bound to 11-cis retinal which is located inside the membrane of the outer segment's (OS) discs. As a consequence, G-protein transducin (T) and phosphodiesterase (PDE) remain inactive (upper panel). Recovered cGMP triggers opening of the cation channels in photoreceptor disc membrane mediating Na⁺ and Ca²⁺ influx (middle panel). This in turn depolarizes the membrane potential of the inner segments triggering the release of glutamate (Glu) in photoreceptor synapses (lower panel). Abbreviations: PDE-Phosphodiesterase, cGMP-cyclic guanosine mono phosphate, T-transducin, OS-outer segments, IS-inner segments, Na⁺-Sodium, Ca²⁺-calcium. Adapted from (Klapper et al.,2016).

Interestingly, photoreceptors detect both dim light (single photons in case of rods) and bright light (photopic high acuity colored vision in cones). Phototransduction is followed by a series of steps involving deactivation of the phototransduction cascade. In transition from light to dark phase, low calcium concentration in photoreceptor inner segments induces recovery of cGMP, inactivation of activated proteins such as transducin and regeneration of rhodopsin photopigment. Increased cGMP concentration triggers opening of the membrane associated cation channels depolarizing the cell. Finally, the photoreceptors return back to their dark state, restoring Ca²⁺ current through the

voltage gated calcium channels and tonic glutamate release in the photoreceptor terminals (Sung & Chuang, 2010) (Fig. 3).

1.3 Retinal synaptic pathways

Specialized contacts at which neurons transmit signals are called synapses. Neurons of similar nature make up each layer in the retinal organization. Adjoining cells from different layers are linked to one another through electrochemical synapses, where the presynaptic neurons secrete neurotransmitters at the synapses that are detected by the postsynaptic neurons. These retinal synapses are of two natures: excitatory and inhibitory. The former are the ones in which the presynaptic terminals release excitatory neurotransmitters that depolarize and thus excite the post synaptic cells. In the latter ones, inhibitory neurotransmitters are released that hyperpolarize the post synaptic cells. The photoreceptor, bipolar and ganglion cells are the excitatory cells while the amacrine and horizontal cells are the inhibitory ones. Synaptic transmission occurs both radially and laterally in the retina. A direct excitatory pathway exists from the photoreceptors radially through the bipolar cells to the ganglion cells. While, lateral synaptic transmission takes place from horizontal cells onto bipolar cells in the outer retina; in the inner retina amacrine cells form lateral synapses onto bipolar/ganglion cells. Through these feedback connections the inhibitory neurons are able to control and modify transmission down the direct excitatory pathway. In the outer plexiform layer (OPL) the photoreceptors interact with the horizontal and bipolar cells. The OPL acts as the first filtering structure mediating spatial oppositions that allows the retinal output to enhance image edges. The inner plexiform layer (IPL) provides additional spatio-temporal shaping of the visual signal through interaction of the bipolar, amacrine and ganglion cells (Wohrer, 2008; (Wu, 2010). Besides electrochemical synapses, neighboring cells in a particular layer of the retina also communicate through pure electrical synapses called gap junctions. These are small direct bidirectional cell to cell pathways for electric currents and small ions and molecules (Sakai & Naka, 1983; Wohrer, 2008).

Light increments and decrements are coded through two parallel paths in the vertebrate retina, the ON and OFF pathways (Fig. 4). The segregation of the two pathways first appears at the level of the bipolar cells. In the dark state the ON bipolar cells remain inhibited (hyperpolarized) while the OFF bipolar cells are activated (depolarized). Cone photoreceptors synapse with both ON and OFF bipolar cells, whereas rod bipolar cells are primarily of ON type. Besides rod bipolar cells, rods have also been found to synapse with cone OFF bipolar cells (Li, Keung, & Massey, 2004). Similarly some mammalian rod bipolar cells (DBC_{R2}) synapse with both rods and cones (Pang et al., 2018).

INTRODUCTION

Unlike cone bipolar cells (ON and OFF), rod bipolar cells do not make synaptic contacts directly with ganglion cells, rather they synapse onto amacrine (AII) cells which in turn make gap junctions with ON cone bipolar cells. Lateral interactions from the horizontal and amacrine cells make up the base of our sensitivity for contrast vision. Finally, the ON and OFF ganglion cell dendrites receive the information from bipolar and amacrine cells and transmit it to the brain via their axons (Sakai & Naka, 1983; Bloomfield & Dacheux, 2001; Popova, 2014).

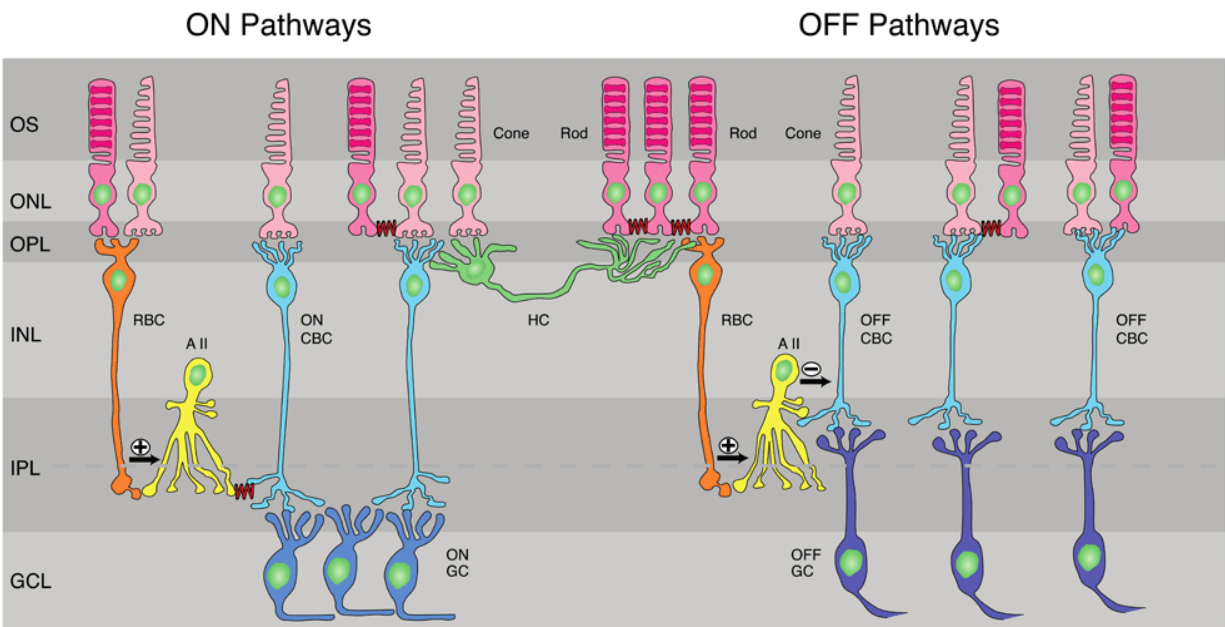


Figure 4: Rod and cone synaptic pathways in mammalian retina (on/off pathways)

Rod bipolar cells (RBC) receive input mainly from rods though some also synapse with cones. Subsequently, RBCs synapse onto AII amacrine cells, which in turn connect to ON cone bipolar cells (ON CBCs) through gap junctions (squiggly lines). The ON CBCs then synapse onto ON-type ganglion cells (ON GCs). (Center) Rods also make gap junctions onto other rods and cones (squiggly lines), and the cones then carry rod signals to ON CBCs. Mouse horizontal cell (HC) dendrites contact exclusively cone terminals while their axons contact exclusively rods. (OFF pathways) AII amacrine cells after receiving input from RBCs make inhibitory glycinergic synapses onto OFF cone bipolar cells (OFF CBCs) which in turn synapse onto OFF ganglion cells (OFF GCs). Cones also receive rod signals through gap junctions which they transmit through OFF CBCs onto OFF GCs. Abbreviations: GCL-ganglion-cell layer, INL-inner nuclear layer; ONL, outer nuclear layer, OPL-outer plexiform layer, IPL-inner plexiform layer, OS-outer segments of photoreceptors, RBC-rod bipolar cell, CBC-cone bipolar cell, AII-Amacrine (II) cells, GC-ganglion cell, HC-horizontal cell. Adapted from Fain & Sampath, 2018.

1.4 Morphology and function of ribbon synapses

In both outer and inner plexiform layers, chemical synaptic junctions exist primarily in two forms. The more common or the so called conventional synapses exist between the bipolar, horizontal and the interplexiform cells (Dowling & Werblin, 1971; Sakai & Naka, 1983). These synapses are similar to chemical synapses seen elsewhere in the vertebrate nervous system, characterized by an

INTRODUCTION

aggregation of vesicles close to the presynaptic membrane. The second type of chemical synapses in the retina is the ribbon synapse which is characterized by an electron dense bar-shaped presynaptic process called the ribbon (Dowling & Werblin, 1971; Sakai & Naka, 1983) (Fig. 5).

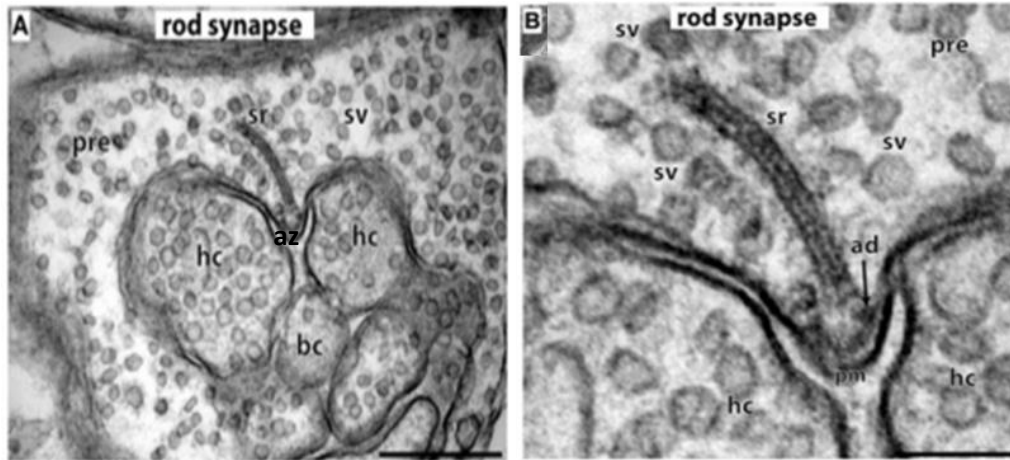


Figure 5: Rod photoreceptor ribbon synapses

In A and B, transmission electron microscopy images show rod photoreceptor ribbon synapses. (A) exhibits a large presynaptic rod photoreceptor terminal filled with numerous synaptic vesicles (sv). The synaptic ribbon (sr) extends from the active zone (az) into the cytoplasm. A large number of synaptic vesicles are found tethered to the ribbon. Opposite to the active zone, there is a pair of horizontal cell (hc) dendritic tips with a bipolar cell (bc) dendrite sandwiched between them. The dendritic tips invaginate into the presynaptic terminal. (B) represents a zoomed-in view of the synaptic ribbon with its tethered synaptic vesicles. Besides the ribbon, there is another electron dense structure at its base in the active zone, called the arciform density (ad) to which the ribbon is anchored. Abbreviations: sr-synaptic ribbon, sv-synaptic vesicles, ad-arciform density, az-active zone, pre-presynaptic terminal, hc-dendritic tips of horizontal cells, bc-dendritic tips of bipolar cells, pm-presynaptic plasma membrane. Scale bars: 400 nm (A), 150 nm (B). Adapted from Schmitz F., 2014.

Both photoreceptor and bipolar synapses in the retina are characterized as ribbon synapses. The ribbon looks like a plate like structure extending from the plasma membrane into the cytoplasm, anchored to the membrane by another electron dense structure called the arciform density. The arciform density is present in an invagination of the presynaptic membrane called the synaptic ridge. From the lateral view because of the arciform density, the ribbon assumes a curved 'comma' like shape (Schmitz F., 2009). The ribbon surface is covered with minute filamented particles of ≈ 5 nm diameter to which neurotransmitter glutamate filled synaptic vesicles attach to. Amongst the tethered vesicles, only the ones in contact with the plasma membrane are considered to be docked, making up the readily releasable pool (RRP). The rest of the vesicles attached to the ribbon constitute the larger slow releasable pool (SRP) (Heidelberger et al., 2005; Sterling & Matthews, 2005). Since the ribbon is associated with synaptic vesicles and is found in close vicinity to the active zone, it is believed to have a crucial role in vesicle trafficking during neurotransmitter release

INTRODUCTION

in synaptic transmission (Lenzi & Von Gersdorff, 2001). Unlike conventional synapses, ribbon synapses do not impart information in an 'all or none' fashion by firing action potentials as it restricts the amount of information transmission. Ribbon synapses are specialized in encoding changes in stimulus intensities to graded changes in neurotransmitter release (Dieck & Brandstätter, 2006).

Ribbon synapses are not only found in the retina. They are also found in the mechano-sensitive hair cells of the cochlea and vestibular cells, neurons of the pineal gland, neuromast hair cells in the lateral line of fish and in several invertebrate neuromuscular junctions (Lagnado & Schmitz, 2015). The ribbons vary in their shape, size, number and their capacity to tether synaptic vesicles in the various cell types and species (Heidelberger et al., 2005) (Fig. 6).

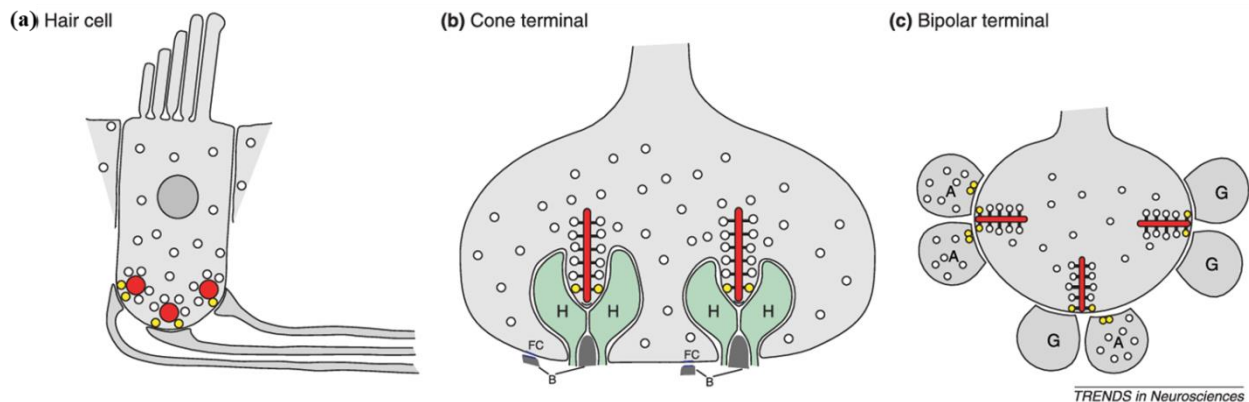


Figure 6: Various types of ribbons

(a) In a hair cell, ribbons (red) are expressed at the basal pole where they tether numerous vesicles at the presynaptic membrane (white and yellow; yellow represents docked vesicles). A hair cell typically contains 10–20 ribbons with each ribbon supplying to one postsynaptic process. (b) In a cone terminal ribbon (red) is located at the top of the invagination created by the central dendritic process of a bipolar cell (B) and the two lateral processes of two horizontal cells (H). (c) In a bipolar terminal each ribbon connects to a dyad of postsynaptic processes, comprising of two ganglion cell dendrites (G) or two amacrine processes (A) or one ganglion and one amacrine cell process. Adapted from Sterling & Matthews, 2005.

Rod photoreceptor ribbons are $\approx 1 \mu\text{m}$ high, $1\text{--}2 \mu\text{m}$ long and 30 nm thick (Fig. 7). On the other hand, the bipolar cell ribbons are smaller in size, vary from bar shaped to ellipsoidal structures and are in higher abundance than the photoreceptor ribbons. Cone photoreceptor cells like bipolar cells have smaller ribbons that are more in number. Ribbons in a mammalian cone terminal tether ≈ 3000 vesicles with a docked population of ≈ 600 , while mammalian rod ribbons have ≈ 640 tethered and ≈ 130 docked vesicles (Sterling & Matthews, 2005). In the entire population of ribbons, the hair cell ribbons morphologically vary the most in their dimensions (≈ 0.1 to $0.4 \mu\text{m}$ in length) as well as shapes (ellipsoidal, plate-like, barrel-shaped, or spherical) and can tether as high as 400 vesicles (LoGiudice & Matthews, 2009). The ribbon synapses are found to differ also in their

INTRODUCTION

post synaptic structures. The photoreceptors form a triad with horizontal cell dendrites laterally at the two sides and a bipolar cell dendrite centrally penetrating into the presynaptic membrane (Fig. 7). While the rod and cone bipolar terminals in the IPL communicate either with a pair of ganglion cell processes or a pair of amacrine cell processes or with an amacrine and a ganglion cell process (Matthews & Fuchs, 2010). A single hair cell ribbon however simply contacts a single post synaptic bouton across a 20 nm wide cleft (Sterling & Matthews, 2005) (Fig. 6).

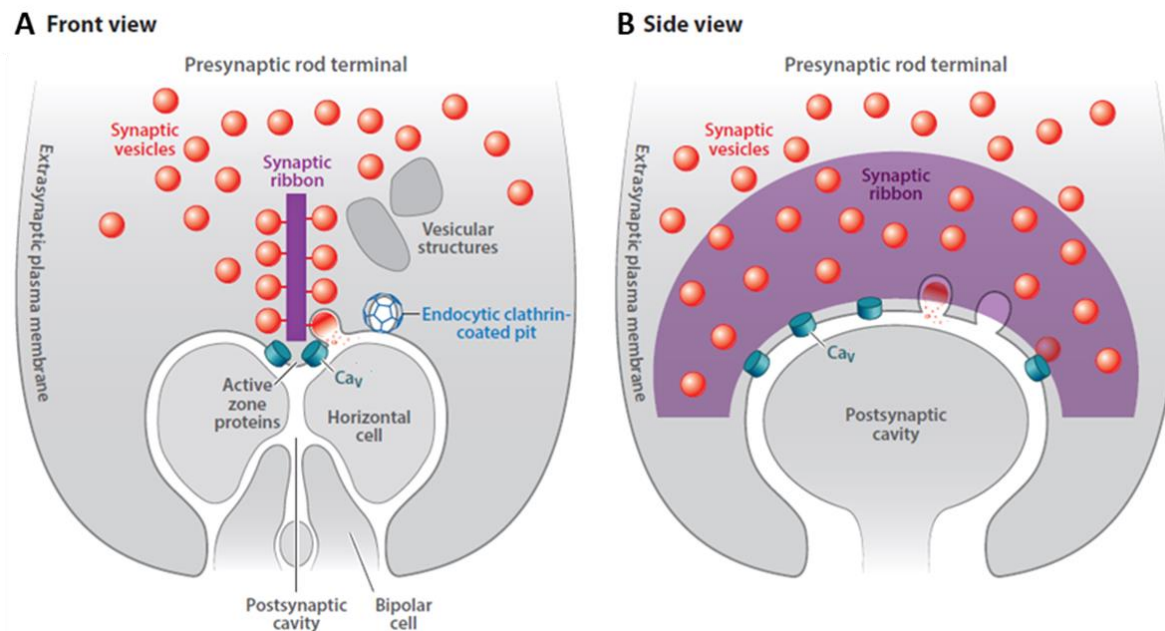


Figure 7: Detailed schematic diagrams of rod photoreceptor terminal

(A) Front-view showing rod shaped synaptic ribbon in cross section (B) side-view revealing horseshoe shaped plate-like ribbon laterally with L-type Ca_v channels at its base at the active zone. Modified from Lagnado & Schmitz, 2015.

Though the various ribbon synapses have these morphological differences, physiologically they perform almost the same purpose. All of them release neurotransmitter continuously through graded changes in membrane potential, remaining tonically active (Morgans, 2001; Schmitz, 2009). Exocytosis of neurotransmitter filled synaptic vesicles in ribbon synapses is similar to that in conventional synapses. Both are mediated via calcium influx through voltage gated calcium channels in the nerve terminals across an electrochemical gradient. In ribbon synapses arciform density that anchors the ribbon is lined with clusters of presynaptic L-type voltage-gated Ca²⁺ channels (Heidelberger et al., 2005; Lagnado & Schmitz, 2015). The presence of vesicles and Ca²⁺ channels at the ribbons suggest that they must play some crucial role in the exocytotic machinery of the tonically active ribbon synapses. Besides the ribbon associated vesicles there is also a huge pool of cytoplasmic vesicles at the ribbon synaptic terminals. These synaptic cytoplasmic vesicles

INTRODUCTION

act as a reservoir to sustain the continuous rate of exocytosis in ribbon synapses (Lagnado & Schmitz, 2015). A popular model states that the fast transient release is supported by the lowest row of synaptic vesicles docked on the ribbon at the membrane. On the other hand the subsequent slower sustained release is maintained by the upper rows of vesicles tethered to the ribbon (already primed) followed by vesicles distributed in the cytoplasm (Matthews & Fuchs, 2010; Lagnado & Schmitz, 2015). To avoid complete shut down of the system by depletion of the readily releasable vesicle pools, vesicular membranes are rapidly retrieved through endocytosis with a time constant $t=1\pm 2$ sec in bipolar cells and $t=7.5\pm 14$ sec in hair cells (Von Gersdorff & Mathews, 1994; Heidelberger, 2001; Parsons & Sterling, 2003; Moser, Brandt, & Lysakowski, 2006). Efficient synaptic transmission by rod photoreceptors even at lower frequencies requires endocytosis to restore the structural and functional integrity of the presynaptic active zone (Thoreson et al., 2004).

1.5 Molecular composition of ribbon synapses

Ribbon is primarily constituted of the protein 'RIBEYE', which was first identified, characterized and cloned by Schmitz et al., 2000. A novel proline rich A domain and a C-terminal B domain almost same as the nuclear repressor CtBP2 make up the RIBEYE protein. Though the same gene encodes RIBEYE and CtBP2, RIBEYE is expressed only in ribbon synapses (Wan et al., 2005; Magupalli et al., 2008). Both the A and B domains have RIBEYE-RIBEYE interaction sites and together act as the foundation blocks of the ribbon (Magupalli et al., 2008). A number of other proteins coexist with RIBEYE at the ribbon and also in the cytomatrix at the active zone (CAZ), helping in synaptic vesicular trafficking (Zanazzi & Matthews, 2009). Examples of proteins found on the ribbon and in the active zone of the ribbon synapse are RIM1, RIM2, bassoon, piccolo, CtBP1, ELKs/CAST, Munc 13s etc. These proteins are also found in conventional synapses. Bassoon and Piccolino (a splice variant of Piccolo present in the sensory ribbon synapses) present at the arciform density and at the ribbon respectively play crucial roles in the structural organization of the ribbon and clustering of synaptic vesicles (Dieck et al., 2005; Mukherjee et al., 2010; Regus-Leidig et al., 2013). The Rab3 interacting molecules RIM1 and RIM2 are present at the ribbon and at the active zone respectively. They play vital role in priming of synaptic vesicles (Dieck et al., 2005; Spiwoks-Becker et al., 2008; LoGiudice & Matthews, 2009). The RIMs have also been accredited with the positive regulation of the L-type $Ca_v1.4$ channels in rod photoreceptor ribbon synapses (Grabner et al., 2015). All ribbon synapses express dihydropyridone sensitive, high voltage-gated L-type calcium channels just at the base of the ribbon at the active zone (Catterall et al., 2005; Matthews & Fuchs, 2010). In contrast to calcium channels in conventional synapses, L-type calcium channels need stronger depolarization

INTRODUCTION

to activate and then inactivates over a much longer duration of time, thus allowing sustained Ca^{2+} influx during tonic release of neurotransmitters (Zanazzi & Matthews, 2009; Mercer & Thoreson, 2011; Lagnado & Schmitz, 2015) (Fig. 8).

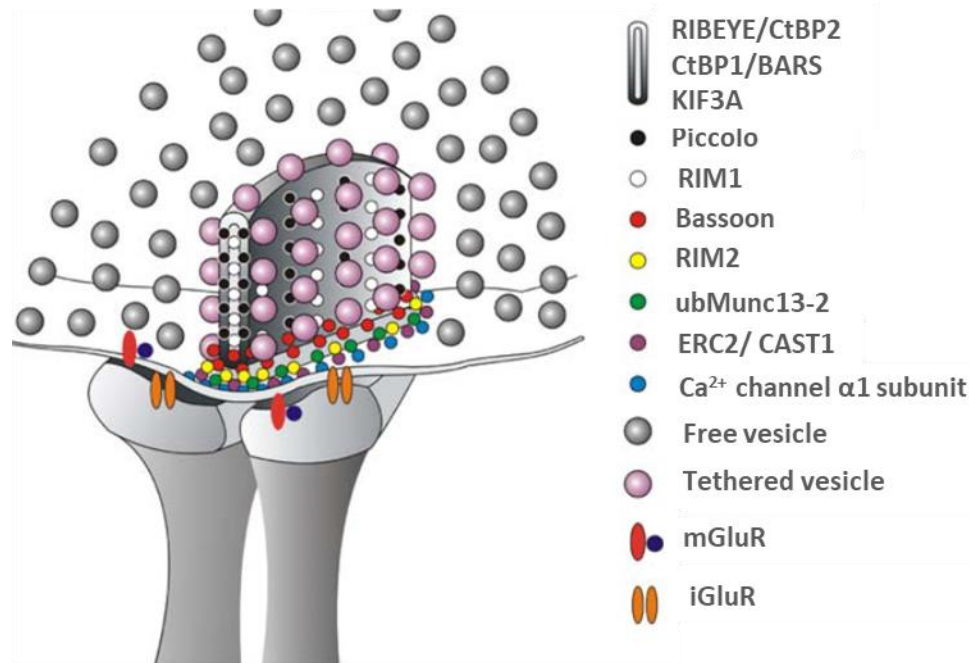


Figure 8: Molecular architecture of a retinal ribbon synapse

CAZ (cytomatrix at the active zone) proteins exist in two defined presynaptic compartments at the ribbon synapse. RIBEYE/CtBP2, CtBP1/BARS, KIF3A, Piccolo and RIM1 are confined to the ribbon-associated compartment. While, the active zone compartment comprises of RIM2, ubMunc13-2, ERC2/CAST1, and a L-type calcium channel. Bassoon is localized at the border of the two compartments in the photoreceptor synapse. Post and presynaptic glutamate receptors metabotropic (mGluR) and ionotropic (iGluR) receptors transmit the glutamate signals as it is released at the retinal ribbon synapses. Modified from Dieck & Brandstätter, 2006.

The fusion machinery in the ribbon synapses is quite similar to that of the conventional synapses. They also utilize the same vesicle (v) and target (t) SNARES (soluble NSF attachment protein receptors) except for the v-SNARE syntaxin1 which is replaced by syntaxin3b in case of retinal ribbon synapses (Zanazzi & Matthews, 2009). Complexins that regulate the SNARE complex by binding with the SNARE proteins in a Ca^{2+} dependent manner, resulting into exocytosis are also present in ribbon synapses. However, complexins 1 and 2 of conventional synapses are replaced by its isoforms 3 and 4 in retinal ribbon synapses, possibly to support the continuous mode of exocytosis (Matthews & Fuchs, 2010; Lagnado & Schmitz, 2015). There is also a high diversity in the vesicular Ca^{2+} sensors in retinal ribbon synapses. While synaptotagmins 1 and 2 (mediators of rapid phasic release in conventional synapses) are found in photoreceptors of higher vertebrates,

they are absent in goldfish and salamander photoreceptors (Von Kriegstein et al., 1999; Heidelberger et al., 2005; Thoreson, 2007). Synaptic layers of both goldfish and rodent retinas showed immunostaining evidences for synaptotagmin 3, a high affinity calcium sensor, (Berntson & Morgans, 2003). There have also been evidences of synaptotagmins 4 and 7 immunolabeling in retinal ribbon synapses (Hirano et al., 2007; Luo et al., 2015).

1.6 Rab3 interacting molecules in photoreceptor synapses

Rab3 is a neuronal GTP binding protein found on synaptic vesicles and involved in calcium mediated exocytosis. They cycle in between a vesicle associated GTP bound form and a free cytosolic GDP bound form. Rab3 interacting molecules (RIMs), localized at the presynaptic active zone, interact only with the GTP bound form of Rab3 and is proposed to regulate docked-synaptic vesicles fusion in a GTP dependent manner (Wang et al., 1997). Rab3 interacting molecules, RIMs exist in 6 isoforms encoded from 4 RIM mammalian genes (Südhof, 2012). Two RIM genes, Rims1 and Rims2 synthesize five different isoforms of RIMs from independent promoters (RIM1 α , RIM1 β , RIM2 α , RIM2 β and RIM2 γ). Additionally Rims 3 and Rims4 encode only γ isoforms. Alternative splicing further diversifies the RIM isoforms (Wang & Südhof, 2003; Kaeser & Südhof, 2005; Kaeser et al., 2008).

In photoreceptor ribbon synapses RIM1 is found on the ribbon itself, whereas RIM2 is thought to be present at the active zone (Dieck et al., 2005; Schmitz, 2009). In mature photoreceptor ribbon synapses RIM α recruits the priming protein ubMunc13-2 to the active zone and also interacts with active GTP bound Rab3A on the synaptic vesicles (Wang et al., 1997; Andrews-Zwilling et al., 2006; Cooper et al., 2012). In conventional synapses formation of the tripartite complex of Munc13-RIM α -Rab3 is considered to be crucial for synaptic vesicle priming and release (Betz et al., 2001; LoGiudice and Mathews, 2009). Therefore it is possible that RIMs play a similar role in mediating priming of synaptic vesicles leading to fusion in photoreceptor ribbon synapses as well (Andrews-Zwilling et al., 2006).

The RIMs 1 and 2 also bind to a number of CAZ proteins. Besides binding to Munc13 by its zinc finger domain, RIMs also bind to CAST family of proteins by its PDZ domain, liprins by its C2B domain, Piccolo by its C2A domain and RIM binding proteins (RBPs) via its proline rich region between C2A and C2B domains (Kaeser et al., 2011; Luo et al., 2017) (Fig 9). Besides interacting with RIMs, RBPs also interact with presynaptic L-type Ca²⁺ channels (Hibino et al., 2002). A few groups have also shown that RIM1 can directly interact with Ca_v β , an auxiliary regulatory subunit of the L type Ca_v channels (Gebhart et al., 2010; Gandini & Felix, 2011). C2 domains of RIM2 are also

seen to bind directly to the cytoplasmic loop of α subunit of L-type $\text{Ca}_v1.2$ channels (Shibasaki et al., 2003). Through these interactions RIM1,2 are proposed to function as regulators of Ca_v channel function, modulating their biophysical properties (Pangrsic et al., 2018). RIMs have been shown to positively regulate Ca^{2+} influx and exocytosis in rod photoreceptor ribbon synapses (Grabner et al., 2015).

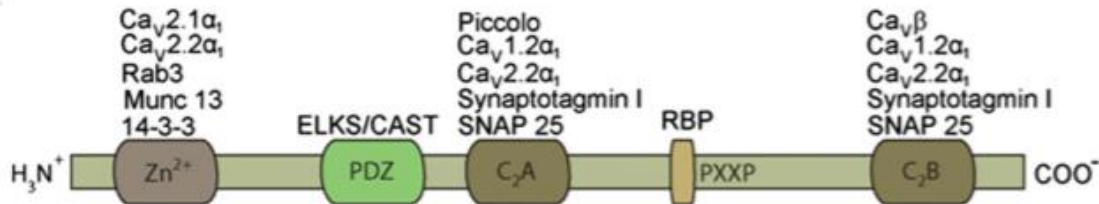


Figure 9: Molecular structure of RIM proteins

One Zn^{2+} -finger-like domain (Zn^{2+}), one PDZ domain (PDZ), two C2 domains (C2A and C2B) and a proline-rich region (PXXP) make up the RIM 1/2 α . The Zn^{2+} -finger-like domain is absent in RIMs 1/2 β while RIMs 2 γ –4 γ comprise only of the C2 domains. Modified from Gandini et al., 2011.

1.7 Voltage gated Ca^{2+} channels in photoreceptor synapses

In response to membrane depolarization voltage gated calcium channels allow influx of Ca^{2+} down its electrochemical gradient from the extracellular space. High voltage activated (HVA) calcium channels comprise of the L (Ca_v1), P/Q ($\text{Ca}_v2.1$), N ($\text{Ca}_v2.2$) and R ($\text{Ca}_v2.3$) type of channels while the T-type (Ca_v3) channels belong to the low voltage activated (LVA) family of channels (Davies & Zamponi, 2008; Gandini et al., 2011). Voltage gated calcium channels at the synapses are strongly coupled to the exocytotic machinery to facilitate controlled neurotransmission. However, calcium signaling is crucial not only in neurotransmission but also in various other intracellular processes such as gene transcription, energy production, membrane excitability, synaptogenesis, etc. where Ca^{2+} acts as an important secondary messenger (Davies et al., 2008; Kawamoto et al., 2012; Dolphin, 2016). Calcium channels are named after the permeating ion, calcium (Ca) and their principle regulator voltage (v) in its subscript, as indicated by Ca_v . The numerical identifier following Ca_v signifies the subfamily of the transmembrane pore-forming $\alpha 1$ subunit of the Ca_v channel and its order of discovery. For instance, the Ca_v1 subfamily ($\text{Ca}_v1.1$ to $\text{Ca}_v1.4$) includes channels containing pore forming subunits $\alpha 1S$, $\alpha 1C$, $\alpha 1D$, and $\alpha 1F$ which mediate L-type currents.

In rod photoreceptor terminals of mice L-type $\text{Ca}_v1.4$ channels (Lee et al., 2014), are found clustered <100 nm from vesicle release sites (Mercer & Thoreson, 2011) at the base of the ribbon, the major site of vesicle release in photoreceptors (Morgans, 2001; Dieck et al., 2005; Heidelberger et al., 2005; Lagnado & Schmitz, 2015). While $\alpha 1F$ subunit of $\text{Ca}_v1.4$ channel has been localized to

INTRODUCTION

rod photoreceptors, cone terminals have been shown to possess L-type α_1D calcium channel subunits (Morgans et al., 2005; Thoreson, 2007). The release of neurotransmitter 'glutamate' at the photoreceptor synapses is dependent on calcium entry into the terminals primarily through these voltage gated (long lasting) L-type dihydropyridone sensitive calcium channels (Schmitz & Witkovsky, 1997). In place of transient bursts of vesicular release, vertebrate photoreceptors exhibit tonic glutamate release at a membrane potential of -40 mV in dark accompanied by a constitutive L-type calcium channel activity. The tonic release property of the photoreceptors makes it necessary for its Ca^{2+} channels to provide strong resistance to voltage and calcium dependent inactivation (Thoreson et al., 2004; Doering et al., 2005; Heidelberger et al., 2005; Lagnado & Schmitz, 2015). Of the four distinct classes of β and $\alpha_2\delta$, β_2 and $\alpha_2\delta_4$ are supposed to co-assemble with the pore forming α_1F subunit to form functional $Ca_v1.4$ channels in rod photoreceptors (Ball et al., 2002; Lee et al., 2014). The major pore forming α_1F subunit is made of four repeated domains (I-IV) of 6 transmembrane spanning segments (S1-S6) each (Gandini & Felix, 2011). Biophysical and pharmacological properties of the $Ca_v1.4$ channel can be attributed to its α_1F subunit, while the auxiliary subunits, β_2 and $\alpha_2\delta_4$ determine its voltage dependence and opening kinetics. Besides regulating functional properties of the $Ca_v1.4$ channel they also help in trafficking of the α subunit to the membrane and protecting it from proteosomal degradation (Baumann et al., 2004; Lee et al., 2014) (Fig 10).

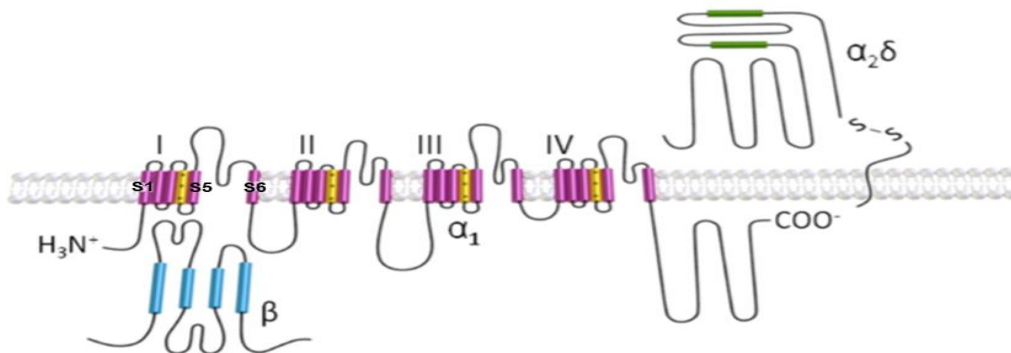


Figure 10: Molecular architecture of Ca_v channel complex

Pore forming α_1 subunit and auxiliary subunits β and $\alpha_2\delta$ make up the high voltage activated Ca_v channels. The α_1 subunit consists of four homologous membrane-spanning repeated domains (I-IV), each with six transmembrane-helices (S1-S6) and a reentrant loop between S5 and S6 making up the pore. Transmembrane helix S4 has the voltage sensor in it indicated in yellow. The $\alpha_2\delta$ subunit is primarily extracellular with a disulphide bond between α_2 and δ while the intracellular β subunit binds to the α subunit at the α -interacting domain (AID) on the intracellular loop between domains I and II. Adapted from Gandini & Felix, 2011.

INTRODUCTION

Loss of function mutations in CACNA1F gene encoding the α_1F subunit of $Ca_v1.4$ channel have been observed to cause incomplete X-linked congenital stationary night blindness. While patients with complete CSNB show moderate to severe myopia accompanied by a complete loss of rod function only (cones work normally), patients with incomplete CSNB show moderate myopia with measurable though subnormal rod and cone responses (Bech-Hansen et al., 1998; Strom et al., 1998; Baumann et al., 2004). The $Ca_v1.4$ channel proves vital not only for photoreceptor synaptic transmission but also in maturation of photoreceptor synapses and functional assembly of ribbons (Mansergh et al., 2005; Liu et al., 2013). In absence of $Ca_v1.4$ channels, presynaptic membrane proteins like PSD95 and Veli3 get abnormally expressed in photoreceptor synapses while scaffolding proteins like Bassoon and RIM2 become mislocalized after eye opening. However, vesicle associated proteins show little alterations. In $Ca_v1.4$ deficient mice rod synapses fail to mature while cone synapses maintain their developing features of synaptogenesis and sprouting even in its adulthood (Zabouri & Haverkamp, 2013).

CACNAB2 gene encodes $Ca_v\beta_2$ subunit of the $Ca_v1.4$ channel (Fig. 11). It has proved to be vital for proper expression and targeting of α_1F subunit in the OPL (Ball et al., 2002). $Ca_v\beta_2$ is also found to be extremely necessary for the morphological and functional integrity of the rod photoreceptor synapses. Its loss also affects cone mediated signaling, though the cone and bipolar cell morphology remains unaltered (Ball et al., 2002; Katiyar et al., 2015). Moreover, mutations in CACNA2D4 gene (Fig. 11) result into functional loss of $\alpha_2\delta_4$ subunit protein of the $Ca_v1.4$ channel. $\alpha_2\delta_4$ mutations are also associated with a form of night blindness in humans (Wycisk et al., 2006a). In $\alpha_2\delta_4$ mutant mice a significant reduction in the number of rod cells is evident with no cone cell degeneration till 6 weeks of age (Wycisk et al., 2006b).

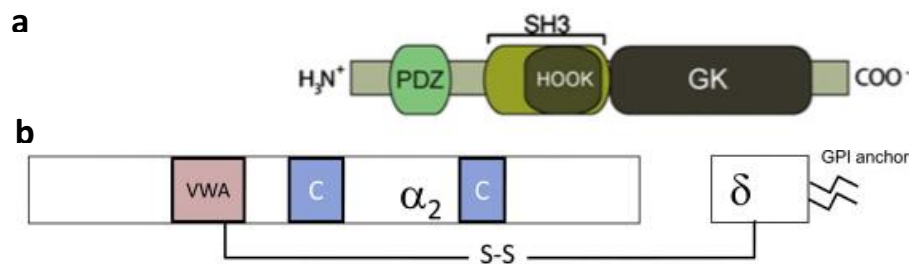


Figure 11: Domain structure of $Ca_v\beta$ and $Ca_v\alpha_2\delta$ subunits

(a) $Ca_v\beta$ is comprised of 3 conserved domains: PDZ, SH3 (Scr homology 3) and GK (guanylate kinase). It interacts with the $Ca_v\alpha_1$ pore-forming subunit via its β -interaction domain (BID). (b) The mature $\alpha_2\delta$ protein is cleaved into α_2 and δ joined by a intersubunit disulfide bond; besides it there are multiple intrasubunit disulfide bonds. The α_2 part has 1 VWA (von-Willebrand factor typeA) and 2 bacterial chemosensory domains and the δ subunit has a GPI (glycosylphosphatidyl inositol) anchor. Modified from Gandini & Felix, 2011; Dolphin, 2013.

1.8 Key players in maintenance of calcium homeostasis in photoreceptor synapses

The tonic release of glutamate in darkness from rod photoreceptor synapses is not brought about exclusively through the continuous calcium influx through L-type calcium channels (Szikra & Križaj, 2006; Suryanarayanan & Slaughter, 2006). Calcium influx triggering a calcium induced calcium release (CICR) response from intracellular calcium stores like the ER at rod photoreceptor terminals appears to maintain tonic synaptic release over long periods of depolarization (Cadetti et al., 2006; Suryanarayanan & Slaughter, 2006; Babai et al., 2010). The calcium release channels on the ER belong to two classes, one can bind ryanodine (ryanodine receptors, RyR) and the second one binds to inositol 1,4,5-triphosphate (IP3 receptors, IP3R) (Križaj & Copenhagen, 2002; Suryanarayanan & Slaughter, 2006; Križaj, 2012). Calcium store depletion is in turn replenished by the mechanism of store operated calcium entry (SOCE), also called capacitative calcium entry (Fig. 12). The STIM1 protein on the ER senses the decreased calcium concentration in the ER and translocates to the plasma membrane binding to the ORAI1 protein which in turn activates TRPC channels bringing about calcium entry (Szikra et al., 2009; Molnar et al., 2012). While there are no hard evidences of CICR in cone photoreceptor synaptic release, SOCE is evidently present in these first order retinal synapses (Szikra et al., 2009; Van Hook & Thoreson, 2015).

During continuous calcium influx in the dark, the intracellular calcium levels need to be kept under tight regulation not only to maintain accuracy of the transmitted visual signals but also for viability of the photoreceptors and down the path neurons (Cadetti et al., 2006). Processes like calcium sequestration, buffering and extrusion help to keep cytoplasmic calcium overload in check. While SERCA (smooth endoplasmic reticulum calcium ATPases) pumps remove extra cytoplasmic calcium by pumping it into the ER, the mitochondria are also claimed to play a part in calcium clearance in ribbon synapses. However, calcium sequestration in the mitochondria is observed only in case of large calcium overloads or in case of inhibition of plasma membrane extrusion (Zenisek & Matthews, 2000; Dartt, 2010). Calcium binding proteins like CaBP, calbindin, calretinin, calmodulin, etc act as cytoplasmic calcium buffers by rapidly removing free calcium ions (Križaj & Copenhagen, 2002; Dartt, 2010). The two final modes of calcium extrusion in photoreceptor synaptic terminals are the Na/Ca exchangers (NCX) and the PMCA (Plasma membrane calcium ATPases) (Fig.12).

INTRODUCTION

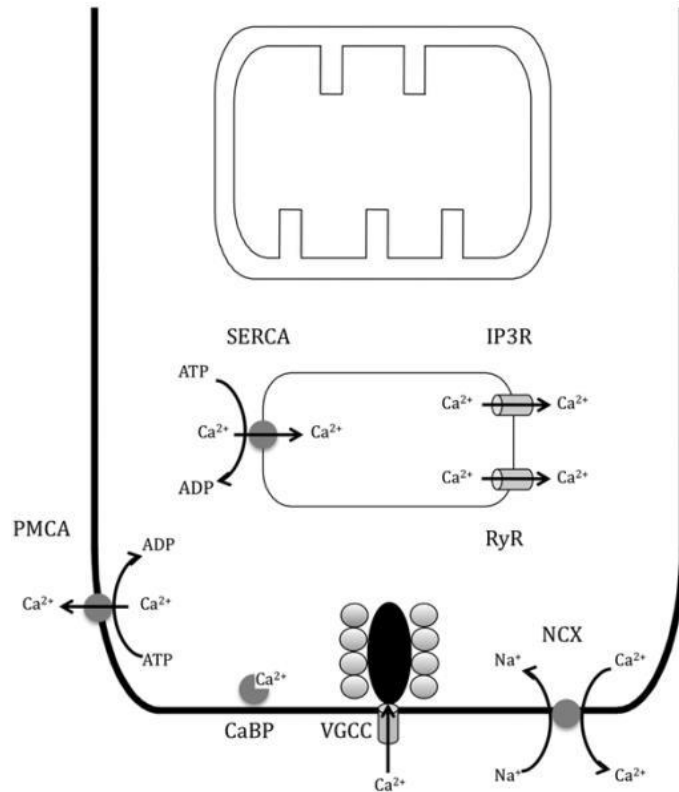


Figure 12: Key players of calcium homeostasis maintenance at ribbon presynaptic terminals

Calcium enters into the ribbon presynaptic terminal primarily through L-type voltage-gated calcium channels (VGCC) found at the active zone below the ribbon. Calcium buffering proteins like CaBP bind to the free Ca²⁺ limiting its spread. Extra calcium is sequestered into endoplasmic reticulum (ER) by sarco/endoplasmic reticulum ATPases (SERCAs). Calcium is released from ER stores through ryanodine receptor (RyR) and inositol 1,4,5-trisphosphate receptor (IP3R) channels. Plasma membrane calcium ATPases (PMCA) located on the lateral walls of the presynaptic ribbon terminal are the principal mode of calcium extrusion in photoreceptor terminals but the sodium-calcium exchanger (NCX) also contribute in Ca²⁺ efflux to maintain homeostasis. Adapted from (Zanazzi & Matthews, 2009).

PMCA function as the chief mode of calcium extrusion in photoreceptor terminals. They have higher calcium affinity though lower binding capacity compared to NCXs. PMCA are found to be more abundant and more efficient in calcium extrusion compared to NCXs in photoreceptor terminals (Zenisek & Matthews, 2000; Križaj & Copenhagen, 2002; Duncan et al., 2006; Herchuelz et al., 2007). PMCA pump out one calcium ion at the expense of one ATP (Morgans et al., 1998). During sustained calcium influx in prolonged darkness the rate of presynaptic calcium extrusion by the PMCA plays a crucial role in governing the rate of tonic synaptic release (Duncan et al., 2006; Križaj & Copenhagen, 2002; Križaj et al., 2002). The mammalian PMCA family comprises of four isoforms PMCA 1–4. ~80% of the PMCA transcript in the mouse retina is comprised of PMCA1 and the rest ~20% by PMCA2, PMCA 3 and 4 are much less abundant (Duncan et al., 2006). Excessive

INTRODUCTION

calcium influx or release from the ER stores or disturbances in cytoplasmic calcium buffering and extrusion can lead to a pathological cytoplasmic calcium concentration overload, triggering apoptosis in the photoreceptors. Increased intracellular calcium is supposed to cause photoreceptor cell death in diseases like autosomal cone dystrophy, retinitis pigmentosa, diabetic retinopathy and so on (Križaj & Copenhagen, 2002; Szikra & Križaj, 2007). On the other hand suboptimal Ca_v channel function as in case of CSNB2 leads to reduced synaptic transmission and visual impairment (Strom et al., 1998; Liu et al., 2013). Thus, here lies the significance of a strictly regulated calcium homeostatic environment.

1.9 Multiple sclerosis and its retinal pathology

Multiple sclerosis is a seriously debilitating neurodegenerative disease affecting 2.5 million people world wide, particularly young adults. The role of autoimmunity in MS is well established (Trapp & Nave, 2008; Dendrou et al., 2015). Inflammation, demyelination and neurodegeneration are the three main aspects of MS. However, the sequence in which they occur still remains debatable (Frohman et al., 2006; Tatomir et al., 2017). Multiple sclerosis is classified into 3 main categories: the relapsing remitting MS (RRMS), secondary progressive MS (SPMS) and primary progressive MS (PPMS). Unlike RRMS, PPMS does not show a higher incidence in females. 80% of patients with RRMS proceed to SPMS while only 10% of MS patients are of the PPMS class (Ortiz et al., 2014; Tatomir et al., 2017). The exact cause of multiple sclerosis is still a mystery. However studies suggest that genetic susceptibility along with environmental factors, driving an autoimmune inflammatory reaction against self CNS antigens, triggers the disease (Alvarez et al., 2011; Ortiz et al., 2014). It is postulated that autoreactive T cells, secondary to an encounter with pathogens, sharing epitopes similar to CNS proteins, are activated. The blood brain barrier (BBB) restricts entry of immune cells in the CNS. In CNS diseases like MS, a transient breakdown of the BBB is supposed to provide the first impetus for disease progression. The interaction of CD4+ T cells with CNS myelin antigens induce a massive inflammatory response. It leads to further proliferation of T cells, B cells and macrophages and subsequent complement system activation along with secretion of inflammatory cytokines and chemokines (Minagar & Alexander, 2003; Dendrou et al., 2015; Tatomir et al., 2017) (Fig. 13). Breakdown of the blood brain barrier (BBB) and inflammatory demyelinating lesions in the brain and spinal cord in various stages of degeneration form the primary neuropathology of multiple sclerosis. Motor dysfunction, vision and speech impairment, muscular weakness and paralysis, loss of balance, cognitive impairment are the various clinical symptoms of MS (Minagar & Alexander, 2003; Matthews et al., 2016).

INTRODUCTION

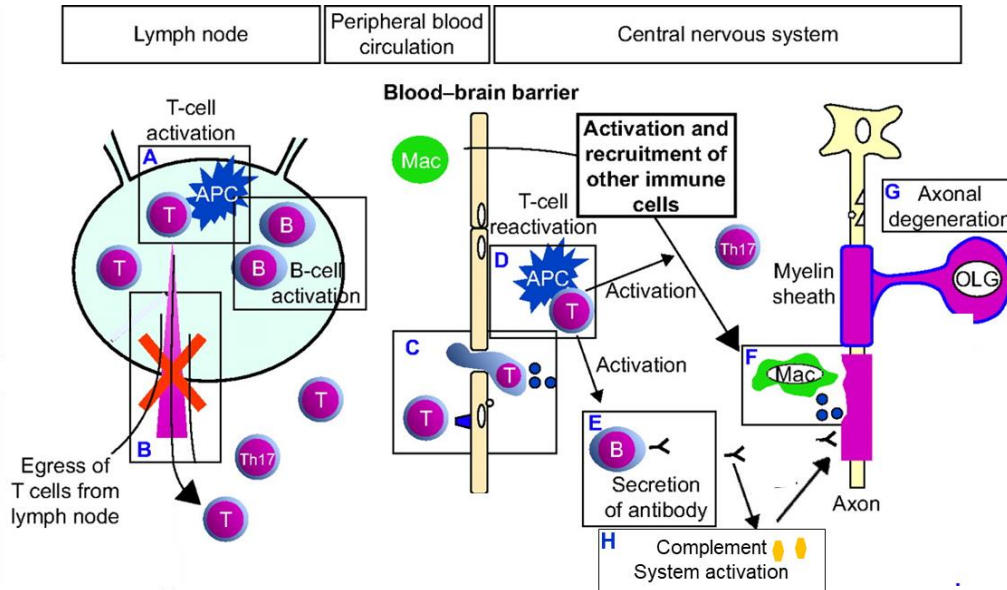


Figure 13: Immunopathogenesis of multiple sclerosis (MS)

The first event is hypothesized to be the activation of peripheral T cells by pathogenic antigens presented by antigen presenting cells (APCs) in secondary lymphoid organs (A). It is followed by egress of the activated T cells from the lymph nodes (B) and transendothelial migration into the central nervous system (CNS) across the temporarily weakened blood brain barrier (BBB), (C). In CNS the T cells on reencountering specific CNS antigens are reactivated (D). Subsequently, the activated T cells induce a massive inflammatory reaction (E, F, H) bringing about axonal degeneration and impulse conduction block (G). Activated macrophages (M θ) phagocytose myelin directly and also release inflammatory cytokines and chemicals along with T cells and glia cells (F). Infiltrating B cells on activation by T cells secrete anti-myelin antibodies (E) and also initiate a complement system cascade bringing about further damage to the myelin containing CNS regions (H). Abbreviations: T-T lymphocytes, Th-T helper cells, Mac-macrophages, APC-antigen presenting cells, OLG-oligodendrocytes, B-B lymphocytes. Adapted from Mehling et al., 2011.

Secondary inflammatory changes in the retina, with the eye being an extension of the CNS are expected in MS. Acute optic neuritis (AON) with inflammatory demyelination of the optic nerve and painful gradual loss of vision is a well established early sign of multiple sclerosis (Atkins et al., 2006; Garrett et al., 2016; Kale, 2016). However, recently retinal nerve fibre layer (RNFL) injury along with changes in the deeper retinal layers have been observed in patients of multiple sclerosis with or without optic neuritis (Saidha, et al., 2011) (Oberwahrenbrock, et al., 2013) (Petzold, et al., 2017). The finding is of great interest because retina is an unmyelinated tissue and so far scientists have ascribed myelin as the target antigen for the disease. Due to accessibility reasons and also availability of techniques, scientists feel that investigation of retinal changes can provide clue towards progression of MS in suspected as well as clinically diagnosed patients (Calabresi et al., 2010; Saidha et al., 2011; Martínez-Lapiscina et al., 2014). Through optical coherence tomography

INTRODUCTION

studies various groups have shown a thinning of the RNFL and ganglion cell-inner plexiform layer (GC-IPL) in MS patients (Behbahani et al., 2017; Petzold et al., 2017). The link of optic neuritis to outer retinal changes is however under much discussion in the scientific community currently (Calabresi et al., 2010; Saidha et al., 2011; Oberwahrenbrock et al., 2013; Al-Louzi et al., 2016; Petracca, et al., 2017). Saidha et al., 2011 have observed that a subpopulation of MS patients who presented primarily with macular thinning rather than RNFL thinning showed a specific thinning of the outer and inner nuclear layers of the retina. Behbahani et al., 2017 also saw that patients with progressive MS show more degeneration of the INL and ONL compared to patients with relapsing remitting type. Moreover, in accordance with the original belief that optic neuritis brings about retinal changes, Al-Louzi et al., 2015 observed a reversible thickening of the ONL and photoreceptor segments and INL+OPL along with thinning of the GC-IPL in the early months after AON in patients with RRMS. Thus, a close investigation of retinal changes correlated with grey and white matter lesion progression can go a long way to deciphering the different pathophysiological mechanisms of various types of multiple sclerosis.

1.10 Experimental autoimmune encephalitis as a multiple sclerosis model

Multiple sclerosis is essentially a human CNS disease, however a number of animal models have been developed that mimic the immunopathological features of MS. Immune-mediated, viral, toxin-mediated and genetic animal models are used not only to better understand the pathogenesis of the disease but also to develop new modes of treatment. While virus-induced animal models are used to evaluate the role of environmental viral pathogens in triggering of the disease (Mecha et al., 2013), toxin mediated induction eg. with cuprizone helps in studying of development and advancement of T cell independent demyelinating CNS lesions (Torkildsen et al., 2008).

Amongst all the MS models, EAE (experimental autoimmune encephalitis) developed by Rivers in 1933 is the most widely used one. EAE can be induced by administration of CNS homogenates or myelin protein or peptide/adjuvant combination (MBP, PLP, MOG, MOBP, MAG, OSP, Nogo-A, CNPase) or through transfer of encephalitogenic T cells into a naïve recipient. It is chiefly a CD4+ T cell mediated autoimmune disease. In active immunization encephalitogenic antigens induce highly polarized Th1, Th2 and Th17 cells specific to the neuroantigen in naïve wild type mice. The activated T cells through enhanced expression of surface integrins and adhesion molecules migrate into the CNS. There, on encountering the neuroantigen against which it was primed, they initiate a local inflammatory cascade. Besides generating myelin damaging inflammatory mediators and cytokines, they activate resident microglial cells and produce chemokines to bring in more immune

INTRODUCTION

cells to carry on the inflammatory cascade (Miller et al., 2007; Matsui, 2008; Constantinescu et al., 2011; Robinson et al., 2014). Disease course and severity however varies with the method of induction and the mouse strains used (Miller et al., 2007; Krishnamoorthy & Wekerle, 2009; Kuerten & Lehmann, 2011; Robinson et al., 2014). The most common models of EAE in mice utilize MBP/PLP/MOG (myelin basic protein/myelin proteolipid protein/myelin oligodendrocytic protein) etc. encephalotogenic peptides along with CFA (complete Freund's adjuvant) as adjuvant and pertussis exotoxin to initiate the infection process (Bittner et al., 2014; Kuerten et al., 2011; Bittner et al., 2014; Dembla, et al., 2018). The adjuvants role in induction of the disease process is in no way lesser than that of the antigen itself. The adjuvants influence differentiation of the naïve T cells into specific cytokine effector lines. While CFA induces a mixed Th1/Th17 immune response in absence of Th2 immunity, incomplete Freund's adjuvant (IFA) triggers primarily a Th2 immunity, and CpG adjuvant a unipolar Th1 immunity (Cribbs, et al., 2003; Kuerten et al., 2011).

ADJUVANT	INDUCED TH CELLS	CYTOKINE PROFILE	EAE/ DTH
IFA	TH2	IL-2, IL-4, IL-5	---
CpG	TH1	IFN- γ , IL-2	---
CFA	TH1/TH17	IFN- γ , IL-2, IL-17	+++

Figure 14: Illustration of type of Th cells and cytokines induced by neuroantigens in various adjuvants
 CFA alone induces a Th1/Th17 response bringing about a DTH reaction and consequently EAE. IL-17 acts as the most crucial cytokine in EAE development. Abbreviations: IFA-incomplete Freund's adjuvant, CpG- short single-stranded synthetic DNA molecule containing cytosine triphosphate deoxynucleotide ("C") followed by a guanine triphosphate deoxynucleotide ("G"), CFA-complete Freund's adjuvant, TH-T-helper cells, IL-interleukin, IFN-interferon, DTH-delayed type hypersensitivity, EAE-experimental autoimmune encephalitis. Modified from Kuerten et al., 2011.

Pertussis toxin injected subsequent to the neuroantigen/adjuvant combination renders the BBB permeable to malevolent CD4+ T cells. Besides that, it also modulates the interaction of the innate and adaptive immune systems to the auto-neuronal antigen to initiate the disease process (Hofstetter et al., 2002; Chen & Oppenheim, 2014). It is also claimed to act as a Th1/Th17 primed adjuvant (Kuerten et al., 2011). Pertussis toxin has also been shown to suppress the protective activity of Treg (Th-regulatory) cells against the disease in vivo, though its mechanism still remains to be elucidated (Chen et al., 2006). For quite a long time, it was believed that the Th1 cells were the principal causal element behind EAE. However, Tigno-Aranjuez et al., 2009 showed that CpG activated T cells, with its Th1 biased response, failed to induce a delayed type hypersensitivity (DTH) reaction. Neither did it demonstrate any histopathological or clinical signs of EAE. Besides that, immunization of neuroantigen with CFA, which is known to develop EAE reliably through Th1

INTRODUCTION

and Th17 activation, when injected with an IL-17 antibody fails to develop the disease (Hofstetter et al., 2002). Moreover, IL-23 knock out mice that can produce Th1 cells but not Th17 cells are found to be resistant towards EAE (Cua et al., 2003; Chang et al., 2010). Thus proving the prerequisite role of IL-17 producing CD4⁺ Th17 cells in autoimmune inflammation of the CNS (Fig.11). Neuroantigen in IFA (incomplete Freund's adjuvant) induces a Th2 immunity in absence of DTH and fails to trigger EAE. Not only that, such a mode of immunization renders the mice resistant to subsequent EAE inducing immunizations (Kuerten et al., 2011).

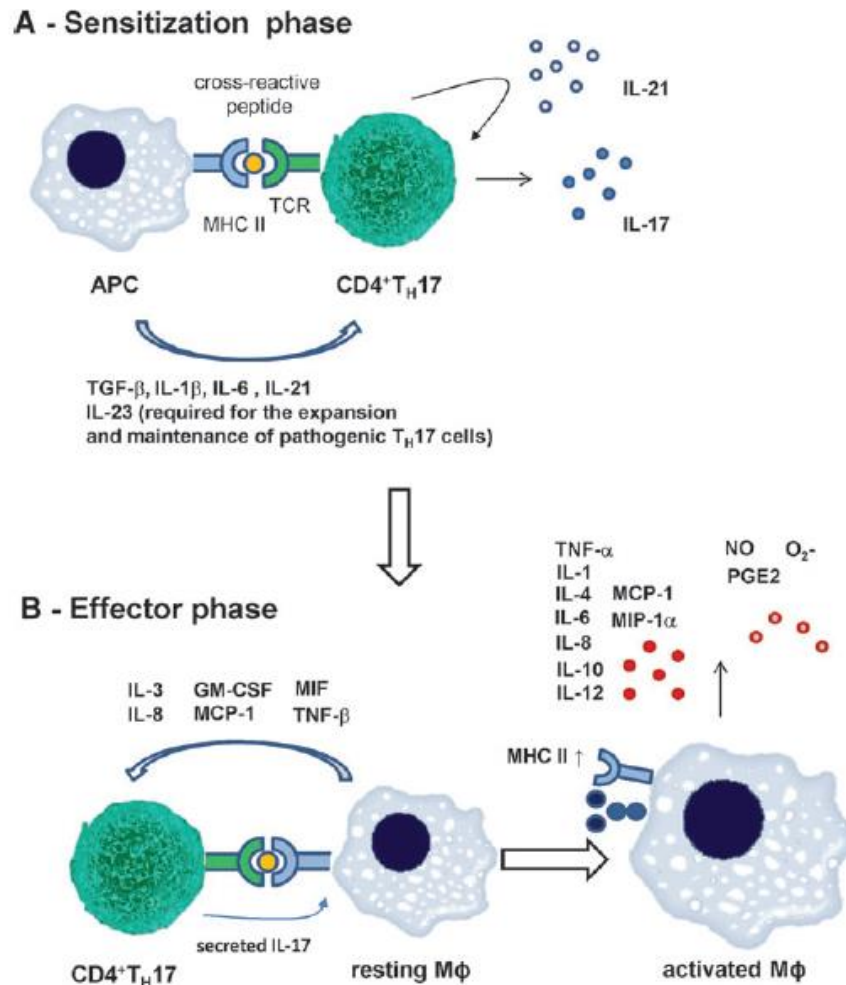


Figure 15: EAE induction through neuroantigen mediated differentiation of CD4⁺ T cells

The sensitization phase takes place in the secondary lymphoid tissues where the naïve CD4⁺ T cells encounter the neuroantigen presented to it by an APC. It leads to proliferation and differentiation of the T cells. Depending upon the adjuvant if an ideal microenvironment of cytokines, TGF-β, IL-1β, IL-6, IL-21, and IL-23 is provided, IL-17 producing Th17 cells are generated. Within 5 to 10 days these effector cells distribute through the entire organism. In the CNS they come in contact with the endogenous neuroantigen and start the effector phase. They activate the resident microglial cells and release chemokines and other cytokines and inflammatory mediators recruiting and activating macrophages and other immune cells. A full blown delayed type hypersensitivity reaction (DTH) ensues. In the entire cascade of events, IL-17 probably plays the most crucial role as it initiates the reaction. Abbreviations: APC-antigen presenting cell, CNS-central

INTRODUCTION

nervous system, DTH-delayed-type hypersensitivity, EAE-experimental autoimmune encephalomyelitis, GM-CSF-granulocyte/monocyte colony-stimulating factor, IL-interleukin, MCP-1-macrophage/monocyte chemo attractant protein-1, MHC-major histocompatibility complex, MIF-macrophage migration inhibitory factor, MIP-macrophage inflammatory protein, NO-nitric oxide, PGE-prostaglandine, TCR-T cell receptor, TNF-tumor necrosis factor, TNFR-tumor necrosis factor receptor. Adapted from Kuerten et al., 2011.

Interestingly, all mice strains do not react in the same way to a specific neuroantigen. In C57BL/6 mice, immunized with myelin basic protein (MBP) or proteolipid protein (PLP), the disease progresses in a chronic fashion. On the other hand, in PL/J and B10PL mice it is in its acute form with no remission, as it is the case of progressive multiple sclerosis in humans. However, SJL mice exhibit a relapsing remitting nature of the disease similar to RRMS (Miller et al., 2007). These differences can be attributed to varied genetic backgrounds and a wide spectrum of MHC haplotypes (Skundric, 2005) in the mice. Acute lethal progressive EAE is quite uncommon in mice, though MS in humans do show this trend. Interestingly, attenuation of the disease progression in mice can possibly be attributed to Th17 cells. Under a favourable cytokine environment, Th17 cells are known to be able to differentiate into inducible T regulatory cells (iTregs), which have a protective role. Another possible cause for amelioration of the disease in mice could be that macrophages cease to respond to the pro inflammatory cytokines released by the T effector cells (Krishnamoorthy & Wekerle, 2009; Kuerten & Lehmann, 2011; Chen & Oppenheim, 2014).

Oscillating nature of the antigenic response of the disease, as in RRMS, can also be explained through 'epitope spreading and its subsequent reaction'. In it, naïve T cells that enter the CNS along with the effector cells get activated on encountering new neuroantigens (different from the one used in the initial immunization action). As the first line of effector T cells undergo apoptosis in the CNS, the new wave of effector cells come over to take their place after a brief remission (Skundric, 2005; Kuerten et al., 2011; Høglund & Maghazachi, 2014).

Although EAE and MS are CD4+ T cell primed diseases, cytotoxic CD8+ T cells, B cells, NK cells, complement system all play significant roles in the pathogenesis of the diseases (Skundric, 2005; Ziemssen & Ziemssen, 2005; Hundgeburth et al., 2013). EAE does not mimic MS in every little aspect, and much is yet to be done to completely understand their similarities and dissimilarities. However, EAE has been successfully used for quite a long time to discern MS pathology and develop various drugs for the treatment of MS. Several US Food and Drug Administration (FDA)-approved MS drugs like glatiramer acetate (GA: Copaxone) and natalizumab (Tysabri), fingolimod, laquinimod, mitoxantrone were first tested in mouse EAE models (Farooqi et al., 2010; Robinson et al., 2014).

1.11 Retinal pathology in experimental autoimmune encephalitis

Similar to optic neuritis in MS patients, alterations in the optic nerve and retina were also observed in experimental autoimmune encephalitis (EAE). Retinal ganglion cell (RGC) loss through apoptosis is observed in the EAE mice model, however with no apparent change in the retinal layer thickness in histological analyses (Shindler et al., 2008; Horstmann et al., 2013). These groups hypothesized that EAE starts as an auto inflammatory disease against myelin, demyelinating the optic nerve and proceeds as a neurodegenerating disease through apoptosis of RGCs. Hein et al., 2012 were one of the firsts to show retinal nerve fibre layer thinning in a rat model of EAE using optical coherence tomography (OCT). They observed the thinning as early as day7 after immunization, before histopathological abnormalities arise in the optic nerve. Their finding was in accordance with Hobom et al., 2004 who had found that RGC death and decreased visual acuity, as measured through visual evoked potential (VEP) and electroretinogram (ERG) studies, occurred before the onset of clinical symptoms. Similarly, Fairless et al., 2012 have reported that in EAE rat model, RGC bodies were found to be lost before their axons in the preclinical phase of the disease. On the basis of EAE clinical disease scoring as per IACUC guidelines¹, Fairless et al., 2012 observed the appearance of the first clinical EAE disease symptoms at the earliest on day10 after immunization with MOG₃₅₋₅₅/CFA, marking days 1 to 9 after immunization as a pre-clinical phase (Fig. 16). These findings indicate that most likely there are factors within the retina itself that trigger retinal degeneration and are independent of optic nerve injury (Hobom et al., 2004; Fairless et al., 2012; Stojic et al., 2018). Retinal studies conducted in the EAE animal models so far are mainly focussed on the health of the retinal ganglion cells. However, outer retinal changes have also been documented in MS patients (Saidha et al., 2011; Behbahani et al., 2017) and needs to be addressed in greater detail in EAE animal models as well.

Interestingly Dembla et al., 2018 observed degenerative changes in OPL of the retina in two separate EAE mice models at a preclinical phase of the disease. Even before demyelination of the optic nerve started, they found that photoreceptor ribbon synapses in EAE mice were being targeted by an autoreactive immune system. Key ribbon associated proteins like RIBEYE, Caspr1 and Contactin were found to be lost significantly to an overactive complement system. Besides these morphological changes, they also observed a significant reduction in synaptic vesicle cycling and visual acuity of the EAE mice at a preclinical stage. However, reasons behind the diminished exocytosis at the OPL and poor optokinetic response of the EAE mice still remains to be elucidated. Thus, a lot of possibilities for further study on the retina as an early EAE pathology remain viable.

¹ <https://bit.ly/2DL7e52> accessed on 16th February, 2019.

INTRODUCTION

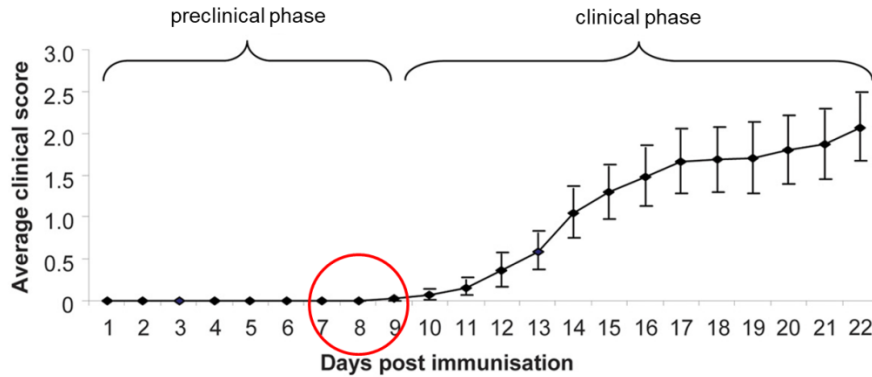


Figure 16: Time course of EAE (days post immunization vs average clinical EAE score)

First EAE clinical symptoms arise at the earliest on day 10 post immunization. Days 1 to 9 were referred to as the preclinical phase. Experiments in this thesis work were focussed on days 7, 8 and 9 post immunizations in the preclinical phase. Abbreviations: p.i.-post immunization, EAE-experimental autoimmune encephalitis. Modified from Fairless et al., 2012.

1.12 Working hypothesis

Till date multiple sclerosis is primarily regarded as an inflammatory demyelinating disease of the central nervous system. However recent research demonstrated that MS pathology is not limited to myelinated axons. Besides affecting grey matter of the brain, MS has been known to affect the retina as well (Frohman et al., 2006; Calabresi et al., 2010; Matthews et al., 2016). Optic neuritis, retinal phlebitis, uveitis are established clinical manifestation of MS (Calabresi et al., 2010; Al-Louzi et al., 2016). However, retinal changes in MS with or without optic neuritis is comparatively a recent finding (Fisher et al., 2006; Al-Louzi et al., 2016). These findings are remarkable because the retina is an unmyelinated tissue (Saidha et al., 2011; Oberwahrenbrock et al., 2013; Behbahani et al., 2017). Through optical coherence tomography studies various groups have shown a thinning of the retinal nerve fibre layer (RNFL) and ganglion cell-inner plexiform layer (GC-IPL) in MS patients (Petzold et al., 2017; Behbahani et al., 2017). A few studies have also found outer retinal changes (Saidha et al. 2011; Behbahani et al., 2017) in MS patients independent of optic neuritis.

In EAE, a well established MS model, RNFL thinning, RGC death and decreased visual acuity were observed before the onset of optic neuritis (Hobom et al., 2004; Fairless et al., 2012; Hein et al., 2012). Most remarkably (Dembla et al., 2018) showed synaptic changes in the preclinical phase of EAE, including changes of synaptic vesicle exocytosis. Since exocytosis is a calcium mediated process (Thoreson, 2007; Neher & Sakaba, 2008; Südhof, 2012; Cho & Von Gersdorff, 2012), my aim was to analyze whether these synaptic changes could be based on changes in presynaptic calcium signaling.

2 MATERIALS AND METHODS

2.1 Materials

2.1.1 Antibodies

2.1.1.1 Primary antibodies use in immunofluorescence assays

Name	Host/Clone	Source	Working Dilutions
RIBEYE (2D9)	Mouse monoclonal	Lab-made, (Dembla et al., 2018)	1:1000
RIBEYE (U2656)	Rabbit polyclonal	Lab-made, (Schmitz et al., 2000)	1:1500
SV2	Mouse monoclonal	Developmental Studies Hybridoma Bank (DSHB), Iowa University (Eich et al., 2017; Buckley and Kelly, 1985)	1:20
Ca _v 1.4 C-term	Rabbit polyclonal	Lab-made, (Grabner et al., 2015)	1:800
Ca _v 1.4 N-term	Rabbit polyclonal	Lab-made, (Maxeiner et al., 2016)	1:800
Ca _v β2 (No.1)	Rabbit polyclonal	Gift from Prof. Dr. Veit Flockerzi, Saarland University; Antigenic peptide sequence: DSETQESRDSAYVEPKEDY	1:100
Ca _v β2 (No.2)	Rabbit polyclonal (affinity purified)	Gift from Prof. Dr. Veit Flockerzi, Saarland University; Antigenic peptide sequence: ISKRRNEAGEWNRDVYIRQ (also referred to as 'Ca _v β2 ab 425' in Katiyar et al., 2015)	1:800
RIM1,2	Rabbit polyclonal	Lab-made (Schoch et al., 2006; Anjum et al., 2014)	1:1000
RIM2 (4F7)	Mouse monoclonal	Lab-made Antigenic peptide sequence: MEYSWLEQASWHSEASPSMLC	1:10
RIM2 (4C6)	Mouse monoclonal	Lab-made Antigenic peptide sequence: MEYSWLEQASWHSEASPSMLC	1:10

MATERIALS AND METHODS

PMCA1	Rabbit polyclonal	Thermo Fisher Scientific (Pdt: PA1-914), (Hegedüs et al., 2017)	1:100
PMCA2	Rabbit polyclonal	Thermo Fisher Scientific (Pdt: PA1-915), (Jeong et al., 2016)	1:100

2.1.1.2 Secondary antibodies used in immunofluorescence assays

Name	Host/Clone	Source	Working Dilutions
Alexa CAM 488	Chicken anti mouse	Invitrogen, Molecular Probes (Cat:A-21200)	1:1000
Alexa DAR 568	Donkey anti Rabbit	Invitrogen, Molecular Probes (Cat:A-10042)	1:1000
Alexa CAR 488	Chicken anti Rabbit	Invitrogen, Molecular Probes (Cat:A-21441)	1:1000
Alexa DAM 568	Donkey anti Mouse	Invitrogen, Molecular Probes (Cat:A-10037)	1:1000
Alexa GAR 647	Goat anti Rabbit	Invitrogen, Molecular Probes (Cat:A-21245)	1:1000
Anti-rabbit Fab fragments	Goat anti Rabbit	Rockland Immunochemicals, (Cat: 811-1102)	1:50

2.1.1.3 Primary antibodies used in Western blot assays

Name	Host/Clone	Source	Working Dilutions
Ca _v 1.4 N-term	Rabbit polyclonal	Lab-made, (Maxeiner et al., 2016)	1:1500
Ca _v β2 (No.2)	Rabbit polyclonal (affinity purified)	Gift from Prof. Dr. Veit Flockerzi, Saarland University; Antigenic peptide sequence: ISKRRNEAGEWNRDVYIRQ (also referred to as 'Ca _v β2 ab 425' in Katiyar et al., 2015)	1:1500

MATERIALS AND METHODS

RIM1,2	Rabbit polyclonal	Lab-made (Schoch et al., 2006; Anjum et al., 2014)	1:800
Actin	Mouse monoclonal	Millipore, (Cat: MAB1501)	1:2000
Fodrin	Mouse monoclonal	Millipore, (Cat: MAB1622)	1:2000

2.1.1.4 Secondary antibodies used in Western blot assays

Name	Host/Clone	Source	Working Dilutions
GAR POX	Goat anti Rabbit	Sigma, (Cat: A3673)	1:5000
GAM POX	Goat anti Mouse	Sigma,(Cat: A6154)	1:3000

2.1.2 Reagents and chemicals

Name	Company
Acetic acid	Roth
Acetone	Fischer Scientific
Amido Black	Merck
APS	Applichem
Benzil	Science Services
Bovine serum albumin	Sigma
Calcium chloride (dihydrate)	Grussing GmbH
Calcium Chloride	Roth
Cell Culture PBS	Sigma
Cobalt	Merck
Cellulose acetate membrane	GE Healthcare
Di sodium hydrogen phosphate	Roth
Dimethylsulfoxide	Roth
Dodecenyl Succinic Anhydride (DDSA)	Electron Microscopy Sciences
DMEM Dulbecco's modified Eagle's medium	Sigma
EDTA	Roth
Epoxy embedding medium (Epon 812)	Fluka-Sigma-Aldrich
Ethanol	ZCHL

MATERIALS AND METHODS

Formaldehyde	Sigma-Aldrich
Fetal Calf Serum	PAA
FURA-2 AM	Biotium
Formic acid	Merck
Glutaraldehyde	Agar Scientific Ltd.
Glucose	Applichem GmbH
Glycerol	Applichem GmbH
HEPES	Roth
Hydrogen peroxide	Roth
Hydro Chloric acid	VWR Chemicals
Incomplete Freund's Adjuvant	Sigma
Inactivated Mycobacterium Tuberculosis	Fisher Scientific
Immersion Oil	Zeiss
LR-Gold	London Resin Company
Low range protein standard Roti marker	Roth
Luminol	Roth
Magnesium Chloride (hexa hydrate)	Sigma
Methanol	Roth
Methyl-5-Norbornene-2,3-Dicarboxylic Anhydride (MNA)	Electron Microscopy Sciences
Methyl Butane	Roth
MOG ₃₅₋₅₅ / CFA kit	Hooke's Laboratories
Non-fat dry milk powder	Supermarket
Nonidet P 50 NPG (n- Propylgallate)	Sigma.
Nitrocellulose membrane	Millipore
Para-hydroxy Coumarin Acid (PCA)	Roth
Paraformaldehyde	Roth
Pertussis toxin	List Biological Laboratories
Pluronic F-127	Invitrogen
Ponceau S-stain	Roth
Potassium chloride	Grussing GmbH
Potassium dihydrogen phosphate	Roth
Rotiphorese Gel 30 (29% acrylamide, 0.8 % bisacrylamide)	Roth

MATERIALS AND METHODS

Sodium azide	Merck
Sodium chloride	VWR
Sodium hydroxide	VWR
Sodium methylate	Merck
Sodium pyruvate	Sigma
TEMED	Roth
Trichloroacetic acid	Roth
TRIZMA BASE	Roth
Tween 20	Roth
Trypsin	Sigma
2,4,6-Tri(dimethylaminomethyl)phenol (DMP-30)	Electron Microscopy Sciences
Xylol	ZCHL
Whatman filter paper	Roth

2.1.3 Cell line

Name	Description
HEK 293T	The HEK 293T was derived from the HEK293 cell line which in turn was derived from human embryonic kidney (HEK) cells. The HEK 293 line was first started by transforming normal HEK cells with sheared fragments of adenovirus 5 DNA. Through the transformation approximately 4.5 kilo bases of the viral genome got incorporated into human chromosome 19 of the HEK cells. HEK293T was first cultured in Michele Calos's lab at Stanford, where HEK293 cell line was stably transfected with a temperature sensitive mutant of SV40 large T antigen. HEK293T can be easily transfected with DNA and plasmids with an SV40 origin of replication are easily replicated with a high copy number in it.

2.1.4 Plasmid vectors (previously cloned)

Name	Description
RIM2/pCMV	This mammalian expression vector has constitutive CMV promoter used to express cloned genes in a variety of mammalian cells. Cytomegalovirus (CMV) is a genus of viruses in the order Herpesvirales, with humans and

MATERIALS AND METHODS

	monkeys as its natural hosts. The kozak sequence allows optimal expression of fusion protein. It has neomycin and kanamycin resistance genes. RIM2 full length cDNA is cloned into it in between the ECOR1 and SMA1 sites (Wang et al., 1997; Schoch et al., 2006).
RIM2/mCherryN1	In pEGFP-N1 plasmid EGFP was replaced with mCherry using BamH1 and Not1 restriction sites. This plasmid has the SV40 promoter. SV40 or simian vacuolating virus 40 is a polyoma virus found in humans and monkeys. It has pUC origin of replication and an f1 origin and neomycin/kanamycin resistance genes. RIM2 was cloned in mCherryN1 using Xho1 and EcoR1 sites. (Dembla et al., 2014).

2.1.5 Buffers and media

Name	Composition
ECL-solution (Chemiluminescence detection system)	1:1 v/v ECL I and ECL II ECL I : 10 ml Tris 1M pH 8.5 1 ml Luminol stock Para-hydroxy Coumarin Acid (PCA) Make volume up to 100 ml with dd H ₂ O ECL-II : 10 ml Tris 1M pH 8.5 64µl H ₂ O ₂ Make volume up to 100 ml with dd H ₂ O
5x PBS	40 g NaCl 1 g KCl 7.2 g Na ₂ HPO ₄ 1.2 g KH ₂ PO ₄ Make up to 1 litre with dd H ₂ O
PBST (1X)	2ml Tween-20 in 900 ml PBS Make volume up to 1litre with dd H ₂ O
Polyacrylamide 10% running gel	1.5 ml dd H ₂ O, 1.9 ml 1 M Tris pH 8.8 2.40 ml 30% Acrylamide

MATERIALS AND METHODS

	<p>75 μl 10% SDS 1.5 ml 50% Glycerol 5 μl TEMED 40 μl 10% APS</p>
Polyacrylamide 7% running gel	<p>2.2 ml dd H₂O, 1.9 ml 1 M Tris pH 8.8 1.75 ml 30% Acrylamide 75 μl 10% SDS 1.5 ml 50% Glycerol 5 μl TEMED 40 μl 10% APS</p>
Polyacrylamide stacking gel	<p>2.4 ml dd H₂O 950 μl 1 M Tris pH 6.8 500 μl 30% Acrylamide 50 μl 10% SDS 10 μl TEMED 50 μl 10% APS</p>
Ponceau S-stain	<p>30 g Trichloroacetic acid 5 g Ponceau S Make volume up to 1 litre with dd H₂O</p>
SDS-PAGE-electrophoresis buffer	<p>3.03 g Tris 14.4 g Glycine 1.0 g SDS Make volume up to 1 litre with ddH₂O</p>
SDS-loading buffer 4x	<p>1,6 g SDS 4 ml β-Mercaptoethanol 2 ml Glycerol 2 ml 1M Tris pH 7 4 mg Bromo phenol blue 2 ml of ddH₂O</p>
Transfer buffer (Western blot)	<p>Tris 15.125 g Glycine 72.05 g Methanol 1 litre</p>

MATERIALS AND METHODS

	Make volume up to 5 litres with dd H ₂ O
EPON embedding medium	6.5 g of epoxy embedding medium (Epon 812), 2.75 g of Dodecenyl Succinic Anhydride (DDSA); 4 g Methyl-5-Norbornene-2,3-Dicarboxylic Anhydride (MNA); 0.1g of 2,4,6-Tri(dimethylaminomethyl)phenol (DMP-30)
Xylol/Methanol	1 Xylol : 1 Methanol
Amidoblack staining solution	0.5% Amidoblack 45% Methanol 45% Distilled water 10% Acetic acid
Amidoblack washing solution	47.5% Methanol 47.5% Distilled water 5% Acetic acid
Cellulose acetate membrane solubilizing solution	80% Formic acid 10% Acetic acid 10g Trichloroacetic acid
Dulbecco's modified Eagle's medium /10% FCS (DMEM for HEK293T cells)	900 ml DMEM 100 ml FCS (per litre)
Chloroquin	51.59 mg chloroquin 10 ml H ₂ O
10X HBBS	20 g NaCl 0.93 g KCl 0.334 g Na ₂ HPO ₄ .2H ₂ O 2.5 g Glucose 12.5 g Hepes Make volume up to 250ml with dd H ₂ O pH 7.05- 7.12
High potassium solution (50mM K ⁺)	4.967 g NaCl 3.728 g KCl 0.203g MgCl ₂ .6H ₂ O

MATERIALS AND METHODS

	<p>0.294 g CaCl₂ 2.38 g HEPES 1.100 g Sodium Pyruvate 1.80 g Glucose Make volume up to 1 litre with dd H₂O pH 7.4 & Osmolarity 305-315 mOsm/L</p>
Resting solution (2mM Ca ²⁺)	<p>7.714 g NaCl 0.227 g KCl 0.203g MgCl₂.6H₂O 0.294 g CaCl₂ 2.38 g HEPES 1.100 g Sodium Pyruvate 1.80 g Glucose Make volume up to 1 litre with dd H₂O pH 7.4 & Osmolarity 305-315 mOsm/L</p>
Low calcium solution (0.5mM Ca ²⁺)	<p>7.714 g NaCl 0.227 g KCl 0.203g MgCl₂.6H₂O 0.074 g CaCl₂ 2.38 g HEPES 1.100 g Sodium Pyruvate 1.80 g Glucose Make up to 1 litre with dd H₂O pH 7.4 & Osmolarity 305-315 mOsm/L</p>
MOG ₃₅₋₅₅ / CFA emulsion	<p>200 µg of encephalotogenic MOG₃₅₋₅₅ (mouse myelin oligodendrocyte glycoprotein) peptide (MEVGWYRSPFSRVVHLYRNGK; >90% purity, generated by Dr. Martin Jung, Department of Biochemistry and Molecular Biology, Medical School Homburg, Saarland University) was mixed at a concentration of 2 mg/ml in sterile water with an equal volume of complete Freund's adjuvant (incomplete Freund's</p>

MATERIALS AND METHODS

	adjuvant, iCFA (Sigma) with 10mg/ml inactivated <i>M. tuberculosis</i> (Fisher Scientific #10218823)).
PTX solution	200ng of pertussis toxin (PTX) from <i>Bordetella pertussis</i> (List Biological Laboratories Inc.#180, via Biotrend, Cologne, Germany) was dissolved in 100µl sterile PBS.

2.1.6 Laboratory instruments and consumable materials

Name	Company
Adjustable pipettes	Eppendorf
Axiovert 200, AxioCam MRm (Camera)	Carl Zeiss
Autoclave	Tuttnauer Systec 5050ELCV
Biofuge fresco	Heraeus
Biofuge primo R	
Biofuge stratos	
Chemidoc XRS system	Bio-Rad
Confocal laser scanning microscope	Nikon
Fluorescence microscope	Axiovert 200 M, Carl Zeiss
Freezer -80°C	Heraeus
Hot air oven	Heraeus
Incubator for cell culture	Thermo
Laminar flow model 1,2	Holten
Magnetic stirrer (Complete Set)	Neolab
Multifuge S-R	Heraeus
pH meter	Inolab
Polyacrylamide gel system	Bio-Rad
Power pack for gel system	GE healthcare
Overhead rotator	Neolab
Refrigerated incubator shaker Innova 4320	New Brunswick Scientific
Steri cycle CO ₂ incubator	Thermo ELECTRON CORPORATION
Sterile filtration device	Millipore

MATERIALS AND METHODS

Super-resolution structured illumination microscope	Carl Zeiss
Thermomixer compact	Eppendorff
Ultracut Microtome (UltraCut S)	Leica
Ultrasound bandelin sonoplus	Bandelin Electronic, Berlin
Vortex	VWR International
Western blot transfer apparatus	HOEFER SCIENTIFIC INSTRUMENTS
Weighing balance CP64	Sartorius
Fluorescence Microscope	Nikon (EPhys)
Wide Field Microscope	Carl Zeiss

2.2 Methods

2.2.1 Induction of experimental autoimmune Encephalitis (EAE)

Female C57Bl/6 mice older than 10 weeks (body weight between 20g-25g) were used to generate the EAE (experimental autoimmune encephalitis) mouse model. It is a common mouse model for multiple sclerosis and optic neuritis (Mix et al., 2010; Robinson et al., 2014). The mice were subcutaneously injected in the axilla and groin with an emulsion of total 200 µg of encephalotogenic MOG₃₅₋₅₅ peptide of mouse myelin oligodendrocyte glycoprotein at a concentration of 2 mg/ml (MEVGWYRSPFSRVVHLYRNGK; >90% purity, generated by Dr. Martin Jung, Department of Biochemistry and Molecular Biology, Medical School Homburg, Saarland University) in sterile water with an equal volume of complete Freund's adjuvant (i.e. incomplete Freund's adjuvant, iCFA (Sigma) with 10mg/ml inactivated *M. tuberculosis* (Fisher Scientific #10218823) as described in (Williams et al., 2011; Dembla et al., 2018). Immunizations were performed by Dr. Karin Schwarz, Department of Anatomy and Cell Biology, Medical School Homburg, Saarland University. To increase blood brain barrier (BBB) permeability 200 ng of pertussis toxin (PTX) from *B. pertussis* (List Biological Laboratories Inc.#180, via Biotrend, Cologne, Germany) in 100µl sterile PBS was injected intraperitoneally on the same day (1-2 hr after the MOG₃₅₋₅₅ peptide injection) and also the next day (16-20 hr after the first PTX injection). Control mice were injected only with CFA and PTX toxin. Besides the homemade MOG₃₅₋₅₅ peptide, commercial premade, ready to use injectable suspensions (MOG₃₅₋₅₅/CFA Emulsion PTX, Hooke Laboratories, Lawrence, MA, USA #EK-2110 and CFA control kit # CK-2110) were also used in EAE induction, to rule out the effects supposedly arising from our peptide suspension preparatory techniques as a result of some contaminant.

2.2.2 Isolation of mouse retina and initial processings

Mice were sacrificed by cervical dislocation following deep anesthesia (no response to tail and paw pinch) with an overdose of isoflurane. Eyes were enucleated and bathed in low calcium solution (LCS, 0.5 mM Ca²⁺, pH 7.4) at room temperature. Under the microscope, using a sharp needle the eye was punctured at the juncture of the anterior and posterior eye cup. The eye was then dissected into the two cups by cutting along the hole. For Epon embedded retinal sections the entire posterior eye cup, clean of all the vitreous was snap frozen in liquid nitrogen and proceeded as described later. To harvest the retina for Western blot and physiological studies the retina needed to be separated gently from the pigment epithelium of the posterior eye cup. For the former the retinas (isolated in ice cold LCS buffer in this case) were immediately put in hot 4X SDS loading buffer supplemented with 2mM EDTA and boiled for 10 minutes at 96⁰C, it was then frozen at -80⁰C to be used later. For physiological assays slices were made from the isolated retina and proceeded accordingly.

2.2.3 Light microscopy

2.2.3.1 Embedding of Epon resin sections

The mice retinal embeddings in Epon were prepared in accordance with Wahl et al., 2013 (modified from Drenckhahn & Franz, 1986) by Dr. Karin Schwarz, Department of Anatomy and Cell Biology, Medical School Homburg, Saarland University. The tissue was initially flash frozen in liquid nitrogen-cooled isopentane followed by its lyophilization while kept cooled continuously in liquid nitrogen for approx. 24 hrs. The lyophilization was performed in a vacuum of $\approx 10^{-7}$ mbar (10^{-5} Pa) using a TCP270 turbo molecular pump (Arthur-Pfeiffer-Vacuumtechnik) controlled by a PKG020 Pirani-gold cathode gauge control unit and an oil diffusion pump as a pre-pumping unit (type DUO 004B, Arthur-Pfeiffer-Vacuumtechnik). Next, after equilibrating the samples to RT, Epon was added to the samples and allowed to infiltrate for 24hrs on rotor. Finally, the resin-embedded samples were polymerized at 60°C for ≈ 24 h.

2.2.3.2 Immunolabeling of 0.5 and 1.5 μ m thin resin sections

0.5 μ m and 1.5 μ m thick Epon embedded semithin sections were cut from its blocks with a Reichert ultramicrotome and put on cover slips. 0.5 μ m thick sections provide higher resolution compared to paraffin embedded sections and cryosections (Punge et al., 2008). Epon was removed with a slightly altered procedure of (Mayoret al., 1961). The sections were washed in a series of the following solutions: sodium methanolate (30% solution in methanol; MERCK) (12min); 1:1 mixture

MATERIALS AND METHODS

of xylol/methanol (12min); acetone (2x10min), running tap water (10min), PBS (10min). Afterwards the sections were incubated with the primary antibodies overnight at 4⁰C. The following day after extensive PBS washing the sections were incubated with the corresponding secondary antibodies. After 1-2 hrs of incubation, sections were washed well with PBS and mounted with an anti-fade solution containing N-propyl gallate (NPG) (Schmitz et al., 2000). Negative control incubations with only secondary antibodies were done to rule out nonspecific background immunofluorescence. Immunolabeled sections of 0.5µm thickness were analyzed by confocal microscopy and the 1.5µm thick sections by super-resolution structured illumination microscopy. Confocal analyses of PMCAs were performed on 1.5µm sections.

2.2.3.3 Immunolabeling with primary antibodies generated in same species

In order to use two primary antibodies generated in the same species (eg. rabbit) on the same section Fab fragments of that species (eg. rabbit) was used for blocking. After the secondary antibody incubation of one of the primary antibodies was completed as described above, the section was washed very well with PBS. Then the Fc regions of the 1st primary left open by its secondary were blocked with its Fab fragments (eg. rabbit). Fab fragments were applied on the sections at a dilution of 1:50 in PBS for 3-4h at room temperature (Dembla et al., 2018). After washing with PBS the second primary antibody was incubated O/N and was detected the next day with a 2nd secondary antibody that was excited at a different wavelength. Finally subsequent to 3 PBS washes, sections were mounted on glass slides with an anti-fade solution containing N-propyl gallate in glycerol, as described before. In the thesis work, PSD95 rabbit polyclonal and PMCAs 1 and 2 rabbit polyclonal antibodies were used in double labelings using goat polyclonal anti-rabbit IgG Fab fragments (Rockland Immunochemicals #811-1102). Possible crosstalks of antibodies were ruled out by performing the experiment omitting one of the two primaries and checking for specific immunolabeling of the other.

2.2.3.4 Blocking of antibodies (preabsorption experiments)

In preabsorption blocking of monoclonal antibodies, they were first diluted to their respective working concentrations. Specific blocking peptide of concentration 2µg/ml was added to a working dilution of the antibody in the ratio 1:1; to another working dilution an unrelated peptide of same concentration was similarly added. The antibody mixtures were incubated overnight at 4⁰C on a rotator and used the next day for immunolabeling experiments as described before.

2.2.3.5 Confocal laser scanning microscopy

2.2.3.5.1 Principle and methodology

The underlying principle of confocal laser scanning microscopy (CLSM) was first introduced by Marvin Minsky in 1957; however, it took more time to fully develop a working model. In CLSM a focused laser beam is used to scan an object point by point and the images are re-constructed through a computer. Unlike a conventional wide field microscope, in confocal microscopes intensity of a laser light beam is first adjusted by neutral density filters. Next the beam is tilted in an x-y plane and scanned in a raster fashion by scanning filters, focusing it on the fluorescent sample. The light from the sample partly passes back through the objective lens by the same path as the laser, undergoing spatial filtering, thus, eliminating out-of-focus light. A pinhole aperture in the detection system allows only a focused part of the fluorescent light from the sample to reach the light detectors, hence improving the signal to noise ratio. The diameter of the pinhole is adjustable, smaller the aperture, more contrasted is the image. A photomultiplier tube (PMT) detects and amplifies the light signal and in turn generates an electrical signal with no noise and this analog signal is converted to a digital one through a computer. As the laser beam scans along the sample the PMT output is displayed on the computer screen with almost zero time lag, such that real time imaging is very much possible. Additionally, 3D images can be constructed by using the z-stack feature of confocal microscope by obtaining optical sections.

Confocal microscopy on 0.5 μm thick Epon embedded sections was performed using the Nikon setup as previously described in Wahl et al., 2013. Images were taken with a 63x Plan-Apochromat oil immersion objective (numerical aperture of 1.4) at excitation wavelengths of 488nm, 561nm and 647nm.

2.2.3.5.2 Analyses of confocal microscopy images

The images were acquired using NIS Element AR 3.2 software. Reuse settings option was used every time to keep same conditions of acquiring for the CFA and MOG/CFA samples. For counting of the number of punctas of antibody signals, the actual length of the scan area was derived from the software using the Measurements option and the number of punctas were counted using the Multipoint option in the ImageJ-NIH software. Fluorescence intensity of the antibody immunosignals on the sections at particular ROIs were determined using the the integrated density values function, derived from Analyze-set measurements drop down in the Imagej-NIH software. Same ROIs were used for all the images for a set of CFA and MOG/CFA sections with a particular antibody. ROIs were managed using the Analyze-Tools-ROI Manager option. Averages of the values

were calculated and plotted as a % (for fluorescence intensity) and the average count for the number of punctas were extrapolated for 100 μm length of OPL. With the average fluorescence intensity value in case of CFA as 100, all the data points were expressed as percentages and their data distribution was plotted in a box and whisker plot in Origin Pro 2018 software. Distribution of the data was tested using the Shapiro-Wilk's (normality distribution) test and subsequently, statistical significance tests using 2-tailed Students unpaired t-test for normally distributed data or Mann Whitney Rank Sum U test for data in a non-normal distribution were also carried out in the same software.

2.2.3.6 Super-resolution structured illumination microscopy (SR-SIM)

2.2.3.6.1 Principle and methodology

Conventional light microscopy has a resolution of approximately 200 nm in lateral (XY) and 500nm in axial (Z) direction. Super-resolution microscopy affords higher resolution by overcoming this diffraction limit. SR-SIM utilizes a movable grating in the excitation beam path to generate a stripe like illumination pattern, which is applied to the sample. The illumination pattern and the structures in the sample interfere with each other creating an interference pattern, called the Moiré fringes. Since Moiré fringes have a lower spatial frequency than the original structures they can be transmitted through a normal objective lens, thus making the previously diffraction limited borders provide structural information that were inaccessible. In order to create the Moiré pattern in all the three directions, a coherent laser beam is projected through a phase grating, diffracting the light into orders: 0, +1 and -1. These orders on being focused in the back focal plane of the objective interfere forming the 3-dimensional pattern (Talbot effect), which is then processed through a Fourier transformation. It results into a highly-resolved image, with a resolution limit of 100 nm in XY axis and 200 to 250 nm in the Z axis (Bost et al., 2013). In SR-SIM it is also possible to use standard dyes and staining protocols (Schermelleh et al., 2010).

To analyze the contour length of $\text{Ca}_v1.4\alpha$ and $\text{Ca}_v\beta 2$ immunolabeled signals on 1.5 μm thick Epon embedded section super-resolution (SR) 3D-SIM analyses (Schermelleh et al., 2010) was applied as it provides much improved spatial resolution. SR-SIM imaging was performed with the ELYRA PS1 setup from Zeiss. Images were taken with a 63x Plan-Apochromat (NA=1.4) objective and Andor iXon EM-CCD camera with excitation light of 561 nm wavelength and then processed to obtain higher resolution images (Gustafsson et al., 2008; Schermelleh et al., 2010). Z stack images with an interval of 125nm were taken to scan the entire depth of the retinal section for 3D-super-resolution structural illumination microscopy (3D-SIM) (for review, see Schermelleh et al., 2010) using the

ZEN 2010 software (black edition). The images were then processed and a maximum projection image derived for 3-D reconstruction and further analysis. Sections were oversampled to avoid signal loss during 3D reconstruction.

2.2.3.6.2 Analyses of 3D SR-SIM images

ZEN 2012 (black edition) software was used for analysing the contour length of the punctas of antibody signals in the CFA and MOG/CFA retinal sections. First an individual puncta was cropped out of the *.lsm image and after adjusting its z dimension for maximum projection it was converted to a 3D image. Using the open polynomial line option the contour length of the punctas was traced out and the length was obtained in μm . Average of the values was calculated and plotted in MS-Excel. Origin Pro 2018 was used to plot the distribution of the data points in a box and whisker plot and to calculate their statistical significance values. Depending upon the data distribution as tested by the Shapiro-Wilk's test, 2-tailed unpaired Students t-test (for normally distributed data points) and Mann-Whitney U test (for non - normally distributed data points) were carried out to find the statistical significance values.

2.2.4 Western blot assays

2.2.4.1 Protein quantification

To determine the protein concentration in the retinal lysates a simple sensitive method as described in Dieckmann-Schuppert & Schnittler, 1997 was employed. BSA protein standards and retinal lysates were spotted onto small cellulose acetate membrane pieces and air dried. Amido black in an aqueous solution of 45% methanol and 10% acetic acid was used to stain the membrane pieces. After washing off the excess stain in recurrent washes with an aqueous solution of 47.5% methanol and 5% acetic acid, the dye bound membrane pieces were solubilized in an acidic solution of 80% formic acid, 10% acetic acid and 10g trichloro acetic acid. Photometric quantification of the dye was then made at 620 nm. A standard curve using the standard BSA solutions and respective OD values was made and its linear regression equation ($y=mx+c$) and correlation coefficient (r^2) were determined. The measured absorbance of the protein samples at 620 nm were plotted against a reference curve obtained with the known concentrations of BSA and the total protein concentration of the lysates. Protein concentrations were calculated from the equation of linear regression analysis of the standard curve.

2.2.4.2 SDS PAGE

2.2.4.2.1 Principle

SDS PAGE (Sodium dodecyl sulphate–Polyacrylamide Gel Electrophoresis) separates proteins in a mixture on the basis of its size, under the principle that charged molecules migrate towards an electrode with opposite charge in an electric field. However, the rate of migration of proteins in a gel matrix during electrophoresis is not solely dependent on its molecular weight; structure and charge also play an important role. To eliminate the latter influences, samples are treated with 0.1% SDS (Laemmli, 1970), a denaturing agent. SDS not only linearizes the polypeptide chains, it also imparts a uniform negative charge onto them so that the negatively charged SDS covered proteins (all of them with same charge to mass ratio) migrate towards the anode (positively charged electrode). Beta-mercaptoethanol along with SDS in the sample buffer cleaves the intra and inter molecular disulfide bonds, unfolding the proteins into linear chains. Thus the proteins can be separated solely based on polypeptide chain length. The gel matrix used for SDS-PAGE is polyacrylamide, which is chemically inert and can also easily be made up to a variety of concentrations providing different pore sizes for a variety of separating conditions that can be altered to fit ones needs. For the movement of the proteins current is conducted from the cathode to the anode through the gel, through a discontinuous Laemmli buffer system. The polyacrylamide electrophoresis gel has two layers: the upper stacking gel at pH 6.8, a macroporous gel with low concentration to concentrate the samples before running and the lower running gel of higher concentration (5% to 12%) at pH 8.8, to separate out the proteins. The electrode buffer is of pH 8.3. The proteins can be easily visualized by staining with a protein specific stain such as Coomassie Brilliant R 250.

2.2.4.2.2 Western blot using retinal lysates

2.2.4.2.2.1 Methodology

In preparation of retinal lysates for western blot, a pair of the isolated retinas were added to 170 μ l of hot SDS buffer and boiled at 96^oC for 12 mins. In western blot after running of the SDS-PAGE, the separated proteins in the gel were electrophoretically transferred onto nitrocellulose membrane and later checked with Ponceau-S stain for protein. For RIM1,2 and Ca_v β 2 incubations on the very same strip, it was cut into 2 parts at the 118 KDa mark at this stage. Rigorous washing with PBS removes Ponceau S stain completely. After blocking of the membrane in 5% milk/PBST for 1 hr at room temperature and washing in PBST, it is then incubated with a primary antibody (an antibody against a target protein) overnight at 4^oC. The next morning, the membrane was again washed in

MATERIALS AND METHODS

PBST and then incubated for 1-2 hrs at room temperature in secondary antibody conjugated with horseradish peroxidase (HRP). Following washing with PBST, the signals from Luminol (in ECL) on reacting with HRP were captured and documented by a BioRad Gel Doc Chemiluminescence detection system. The size of a protein band was determined by comparing its migration distance against a standard molecular weight ladder.

2.2.4.2.2.2 Analysis of Western blots

The band intensities of the western blots were quantified using the Analyze-Gels option in ImageJ-NIH software. The first rectangular ROI was placed covering the first band and was also used for the subsequent one. The integrated grey values of the bands were then obtained as the area under the curve of the signal peaks generated by the software. To compensate for any loading errors, band intensities of the target proteins (Cav1.4 α , Cav β 2 and RIM1,2) were always normalized by their corresponding housekeeping proteins used on the same strip (fodrin for Cav1.4 α & RIM1,2 and actin for Cav β 2). Average of the values for CFA and MOG/CFA was calculated and plotted in MS-Excel. The data were checked for their distribution through the Shapiro-Wilk's test in Origin 2018. The sample sizes for the blot data were very small, extending upto 6 to 7 data points only. Therefore a Pearson's correlation coefficient analysis was run in MS-Excel. In accordance with De Winter, 2013 if sample sizes of a normally distributed data are very small, but data points in the two groups show very high within-pair correlation (Pearson's correlation coefficient ≥ 0.8), a paired t-test can be performed, even if the 2 populations are independent in nature. The distribution of the data points was represented through a box and whisker plot in Origin 2018.

2.2.5 Calcium imaging of retinal slices of CFA and MOG/CFA injected mice

2.2.5.1 Making of retinal slices

Retinal slices were prepared as described in Wahl et al., 2016. After removing the retinal pigment epithelium and vitreous body, the retina was cut at four sides like a flower and flat mounted onto a nitrocellulose membrane (Millipore, #HABG01300) with a drop of the LCS buffer (at room temperature), with its ganglionic cell layer facing the membrane. The membrane along with the retina was then transferred onto a silica sieve funnel with a 20 ml syringe attached to it, by suctioning manually several times the retina was made to attach firmly to the membrane. Next, the membrane with the attached retina was wetted in buffer and fixed on a glass slide (retina on top) on a spot of Vaseline. The slide was transferred to the cutting stage of a Werblin-type tissue slicer and 200 to 300 μm thick slices were cut from it. Parallel streaks of Vaseline were made on 25 mm

MATERIALS AND METHODS

cover slips and the gaps were filled with 200-300 μl of LCS buffer. Finally the slices were picked, rotated by 90° and fixed between the Vaseline streaks making all the retinal layers visible with the ganglionic layer at the far end of the membrane. The cover slips were kept in Rachel's plexiglass chamber aerated with 5% CO_2 /95% O_2 at room temperature.

2.2.5.2 Loading of retinal slices with FURA2-AM

Calcium indicator dyes used in calcium measurement studies work on the principle that a change in cellular calcium concentration is projected as a robust increase or decrease in fluorescence intensity of the dye. One such dye is FURA2-AM. The acetomethoxy ester group (AM) engineered to the hydrophilic molecule of FURA2 helps in its loading. The AM group makes the dye hydrophobic and cell membrane permeable. The dye gets passively loaded in a reasonably high concentration (100 μM) into the cells from the extracellular medium (1-10 μM). Inside the cells the indigenous cellular esterases cleave the AM groups trapping in the dye molecules (Mauleon et al., 2013). The dye is generally dissolved in DMSO and kept frozen at -20°C that helps in inhibiting the fast hydrolysis of its ester groups in a moist environment. During loading Pluronic-F127 is used to help in dispersion of the hydrophobic AM attached dye molecules in the extracellular medium (Cameron et al., 2016). In our protocol of dye loading a 10 μM FURA2-AM solution (1mM stock concentration in DMSO) was made in Resting Solution (RS, 2mM Ca^{2+} , pH 7.4) with pluronic acid (20% solution in DMSO) in 1:1 ratio. The retinal slices were then incubated with 50 μl of FURA2-AM solution in the humidified aerated glass chamber for 45 to 60 minutes at room temperature (Mauleon et al., 2013).

2.2.5.3 Baseline fluorescence and Ca^{2+} influx measurement with FURA2-AM

2.2.5.3.1 Mechanism of action of FURA2-AM

On the basis of their response to calcium binding calcium indicator dyes are broadly classified as ratiometric and non ratiometric dyes. Ratiometric dyes are more commonly used for Ca^{2+} concentration quantification; however, they can also be used for qualitative assays just to indicate any relative changes in calcium concentration. Fura2-AM is a ratiometric or a dual excitation wavelength dye. FURA2-AM changes its peak excitation wavelength from 380 nm to 340 nm on binding with Ca^{2+} . The emission wavelength of both the populations of FURA2-AM (i.e. its free and bound forms) is 510 nm. An increase in calcium concentration following depolarization results into a raise in the emission fluorescence of the Ca^{2+} bound FURA2-AM molecules (excitation at 340 nm)

accompanied by a corresponding decrease in emission fluorescence of the free dye molecules (excitation at 380 nm) (Kong & Lee, 1995; Barreto-Chang & Dolmetsch, 2009)

2.2.5.3.2 Methodology

After dye incubation a retinal slice was washed twice in resting solution (RS, 2mM Ca²⁺, pH 7.4) before proceeding with its Ca²⁺ influx measurement. For imaging the retinal slice, fixed in between two streaks of Vaseline on a 25mm glass cover slip, was placed in a circular open bottom chamber, and 1.5 ml of Resting solution (RS, 2mM Ca²⁺, pH 7.4) was added to it. The entire setup was mounted on to the stage of the NIKON ECLIPSE FN1 microscope, having a high resolution 1.2 numerical aperture, 10x water immersion objective and a final 2x magnifying lens in front of the camera. A high speed wavelength switcher from Sutter Instruments (Lambda DG4) was used to rapidly interchange between the two excitation wavelengths of FURA2, 340nm and 380 nm. 100 ms of exposure time was applied for both of the excitation wavelengths. The experiment was started with 1.5 ml of resting solution, and during the recording, images were acquired every 1 second using the NIS Elements AR 4.30.02 software. For the initial one minute, ratiometric fluorescence of FURA2 in the slices is at its basal level in the physiological RS (2mM Ca²⁺) solution. Since dye loading conditions for CFA and MOG/CFA retinal slices were kept identical, ratiometric (340/380) baseline fluorescence values could be compared between the two groups, as an indirect measure of the intracellular calcium concentration in the slices at a physiological state. At the 60th second, 1.5 ml of 50 mM K⁺ solution was added (in absence of suction 50 mM K⁺ solution gets diluted 2 times in the recording chamber to 25 mM KCl). On simultaneous excitation with 340 and 380 nm wavelengths the corresponding changes in emission fluorescence at 510 nm brought about in FURA2 were recorded.

2.2.5.4 Analyses of FURA2-AM baseline fluorescence and imaging on depolarization

Averages of the raw baseline ratiometric (340/380) values for CFA and MOG/CFA slices were calculated and compared for each day in case of self-made and commercial peptide (Hooke's Laboratories) injected mice separately. The data were then tested for their normality using the Shapiro-Wilk's test in Origin 2018 and accordingly 2-tailed unpaired Student's t-test (for normally distributed data) or Mann Whitney Rank Sum U-test (for non-normally distributed data) were performed to test the statistical significance. The data distributions were illustrated through box plots in Origin 2018.

MATERIALS AND METHODS

For analyzing, the FURA2-AM response traces to depolarization using high K⁺ solution, first of all the ratiometric 340/380 traces were normalized at two points. 0 to 59th seconds of RS responses (captured every one second) were normalized by the 340/380 value at the 0th second. Similarly, the 60th to 120th seconds of KCl responses were normalized by the 340/380 value at the 60th second (time point of addition of KCl). The average trace for each mouse can then be plotted in MS Excel. To derive amplitude and time constant (τ) of each individual trace, the trace values were put in the Igor Pro 6.22A software and the wave was plotted. Subsequently, curve fitting on the trace was carried out which showed that the traces follow a single exponential fit. The amplitude and time constants (as a parameter for the kinetics of the traces) from all the traces of each mouse were collected. Average of the amplitudes and the taus of the CFA and MOG/CFA injected mice from days 7 to 9 after injections were calculated and plotted separately in MS-Excel. The data distribution was shown through a box and whisker plot and also tested for statistical significance in Origin Pro 2018 software. Depending on the distribution of the data as analyzed by the Shapiro-Wilk's test, 2-tailed unpaired Students t-test (for data in normal distribution) and Mann Whitney Rank Sum U test (for data not in normal distribution) were used to measure the statistical significance of the data. To compare the amplitudes and time constants of the MOG/CFAs over the days 7, 8 and 9; the % values of MOG amplitudes and time constants were calculated separately for all the three days with respect to their respective CFA mean amplitude and time constant. Thus, after normalizing the MOG values against the mean CFA value we could proceed to analyze whether the MOGs on the 3 consecutive days were responding significantly different to their respective CFAs. Since there were 3 independent groups one way ANOVA (when all 3 groups were normally distributed) or Kruskal-Wallis ANOVA (when one or more groups were non - normally distributed) were used in Origin 2018 software to analyze the data. The normality test was done by the Shapiro-Wilks test in Origin.

2.2.6 Overexpression in HEK293T cells to check antibody specificity

2.2.6.1 Plasmid purification

Plasmid purification was done by using QIAGEN buffers. To 100 μ l plasmid in a sterile eppendorf tube 500 μ l of Binding buffer (Buffer PB) was added and mixed by pipetting up and down. The mixture was transferred to QIA prep mini column and spun down at 13000 rpm for 1 minute. The supernatant is discarded and 500 μ l of Wash buffer (Buffer PE) was added to the column and given a spin at 1300rpm for 1 minute. The supernatant was discarded and washed again. The column was spun alone for a final time to remove the traces of alcohol. Next, 50 μ l of pre-warmed 1mM Tris

MATERIALS AND METHODS

HCl was added to the column and incubated at RT for 5 mins and centrifuged at 13000 rpm for 1 minute. The plasmid DNA was quantified at 260 nm wavelength by a spectrophotometer.

2.2.6.2 Sub-culturing of HEK293T cells

HEK293T cells were cultured in DMEM medium with 10% FCS. During sub culturing old medium was discarded and the cells were washed with 20 ml PBS. After incubating the adhered cells in the culture flask with 500 µl of 0.25% trypsin for 1 min at 37°C, 5% CO₂, the flask was gently tapped to dislodge the cells. 5-6 ml of DMEM medium was added to it and the cells were gently pipetted up and down to disperse the clump of cells. Then 250-500 µl of trypsinized cells was gently added to a new culture flask containing 10ml DMEM medium with 10% FCS. The flask was then incubated at 37°C, 5% CO₂ for 3 days.

2.2.6.3 Transfection of HEK293T cells

HEK293T cells were transfected using the calcium phosphate precipitation method (Wigler et al., 1977; Chen & Okayama, 1987). For healthy HEK293T cells to be transfected, 1 ml of trypsinized cells was plated in a Petri dish in 9 ml of 10% FCS supplemented DMEM medium and incubated for 24hrs at 37°C, 5% CO₂ to achieve a minimum of 70-80% confluency. A DNA/CaCl₂ mixture was prepared by adding 120 µl of 2M CaCl₂ drop by drop to a solution of 10 µg of DNA dissolved in 500 µl of sterile water. This DNA mixture was then added dropwise to 1 ml of 2X HBBS medium and mixed well with gentle agitation. While, keeping the mixture standing at RT for a few minutes, the old medium of the HEK293T cells was discarded and replaced with 6 ml of fresh DMEM medium containing 25 µl of chloroquin. Then the DNA- HBBS mixture was added to the cells. After 8 hrs of incubation in chloroquin containing medium, it was replaced with new DMEM medium containing 10% FCS and kept for incubation for 48 hrs at 37°C, 5%CO₂.

2.2.6.4 Western blot of transfected HEK293T cells

For western blot analysis of transfected HEK293T cells, after 48hrs of incubation the cells were scraped off from the plate and collected in 15ml falcons. The cells were centrifuged at 5000 rpm for 15 min. After discarding the supernatant, the cell pellets were washed three times in ice cold 1X PBS. The cell pellets were then incubated in 500µl of ice cold Lysis buffer (100 mM TRIS, 150 mM NaCl, 1 mM EDTA and 1% TritonX-100) and briefly vortexed. The cell suspension was then transferred to 1.5ml microfuge tube and incubated for 30min at 4°C. Then after a final centrifugation step at 13,000 rpm for 15 min, the supernatants were collected in new 1.5ml

MATERIALS AND METHODS

microcentrifuge tubes. 10 μ l of the cell supernatant mixed with 10 μ l of SDS loading buffer and heated for 5 min at 96°C was loaded in the wells of the SDS-PAGE gel and run. Electrotansfer of the proteins from the gel to the nitrocellulose membrane was performed and checked with Ponceau S stain. The membrane was then incubated O/N with the primary antibody whose specificity was to be analyzed by the over expression. The next day subsequent to HRP labeled secondary antibody incubation for 1-2 h, Luminol (in ECL) signals on reacting with HRP were captured and documented by a BioRad Gel Doc Chemiluminescence detection system.

3 RESULTS

Dembla et al., 2018 observed that synaptic vesicle cycling at photoreceptor synapses was significantly diminished in the MOG/CFA injected mice. The phenotype appeared as early as on day 9 after immunization, before development of the clinical signs for EAE (Fig. 16). Similar to other neurons, neurotransmitter release in photoreceptor ribbon synapses is primarily a Ca^{2+} mediated process (Heidelberger et al., 2005; Thoreson, 2007; Lagnado & Schmitz, 2015), so I inquired into potential defects in synaptic Ca^{2+} signaling of EAE photoreceptors. To explore the Ca^{2+} influx machinery in MOG/CFA injected mice in comparison to CFA mice; I first analyzed expression levels of the key proteins that mediate Ca^{2+} entry in the rod photoreceptor terminals.

3.1 $\text{Ca}_v1.4$ $\alpha 1\text{F}$ expression in photoreceptor synapses of MOG/CFA-injected (EAE) and CFA-injected (control) mice

It is in general agreement that the principal mode of depolarization induced Ca^{2+} entry in rod photoreceptor terminals is through the L-type high voltage gated $\text{Ca}_v1.4$ channels (Morgans, 2000; Szikra & Križaj, 2006; Zanazzi & Matthews, 2009). $\text{Ca}_v1.4$ $\alpha 1\text{F}$ subunit (CACNA1F) forms the pore forming subunit of the channel (Catterall, 2011; Striessnig et al., 2014). CACNA1F gene mutations cause multiple visual disorders including incomplete congenital stationary night blindness (Bech-Hansen et al., 1998; Strom et al., 1998). Moreover, $\text{Ca}_v1.4$ KO mice show absence of photoreceptor ribbon synapses and also a lack in rod and cone synaptic transmission (Mansergh et al., 2005; Liu et al., 2013). These studies indicate the importance of $\text{Ca}_v1.4$ channels in development and maintenance of morphology and function of photoreceptor ribbon synapses.

Two independent Ca_v antibodies, $\text{Ca}_v1.4$ $\alpha 1\text{F}$ C-term and $\text{Ca}_v1.4$ $\alpha 1\text{F}$ N-term directed against different domains of the protein were used in immunolabeling of retinal sections of MOG/CFA-injected and CFA-injected mice, and analyzed through confocal and SR-SIM microscopy. The latter antibody was also used in Western blot analyses of retinal lysates of both the control and peptide-injected mice to evaluate the overall protein expression. All the analyses were done on mice sacrificed on day 9 after the CFA and MOG/CFA injections.

3.1.1 $\text{Ca}_v1.4$ α C-term immunolabeling and analyses

' $\text{Ca}_v1.4\alpha$ C-term' was double immunolabeled with anti-RIBEYE mouse monoclonal antibody (2D9) on 0.5 μm thick Epon embedded mice retinal sections and analyzed using confocal microscopy. The

RESULTS

labeling for the $Ca_v1.4$ channel is just at the base of the ribbon (Fig. 17). Using a common ROI in ImageJ NIH software, fluorescence intensity of $Ca_v1.4$ C-term punctas in the outer plexiform layer of CFA and MOG/CFA retinal sections was measured. The antibody labeling in MOG sections was of lower fluorescence intensity compared to CFA. A significant reduction of ~40% was evident (P value=1.55E-07) in case of MOG/CFA (Fig. 17). To account for the decreased fluorescence intensity the number of punctas of $Ca_v1.4$ was also counted in a fixed length of OPL (kept constant over all CFA and MOG/CFA images) in both the groups. However there was no significant reduction in its number in the EAE retina (Fig. 17). RIBEYE also shows decreased fluorescence intensity at photoreceptor synapses in the OPL in MOG/CFA sections (Dembla et al., 2018).

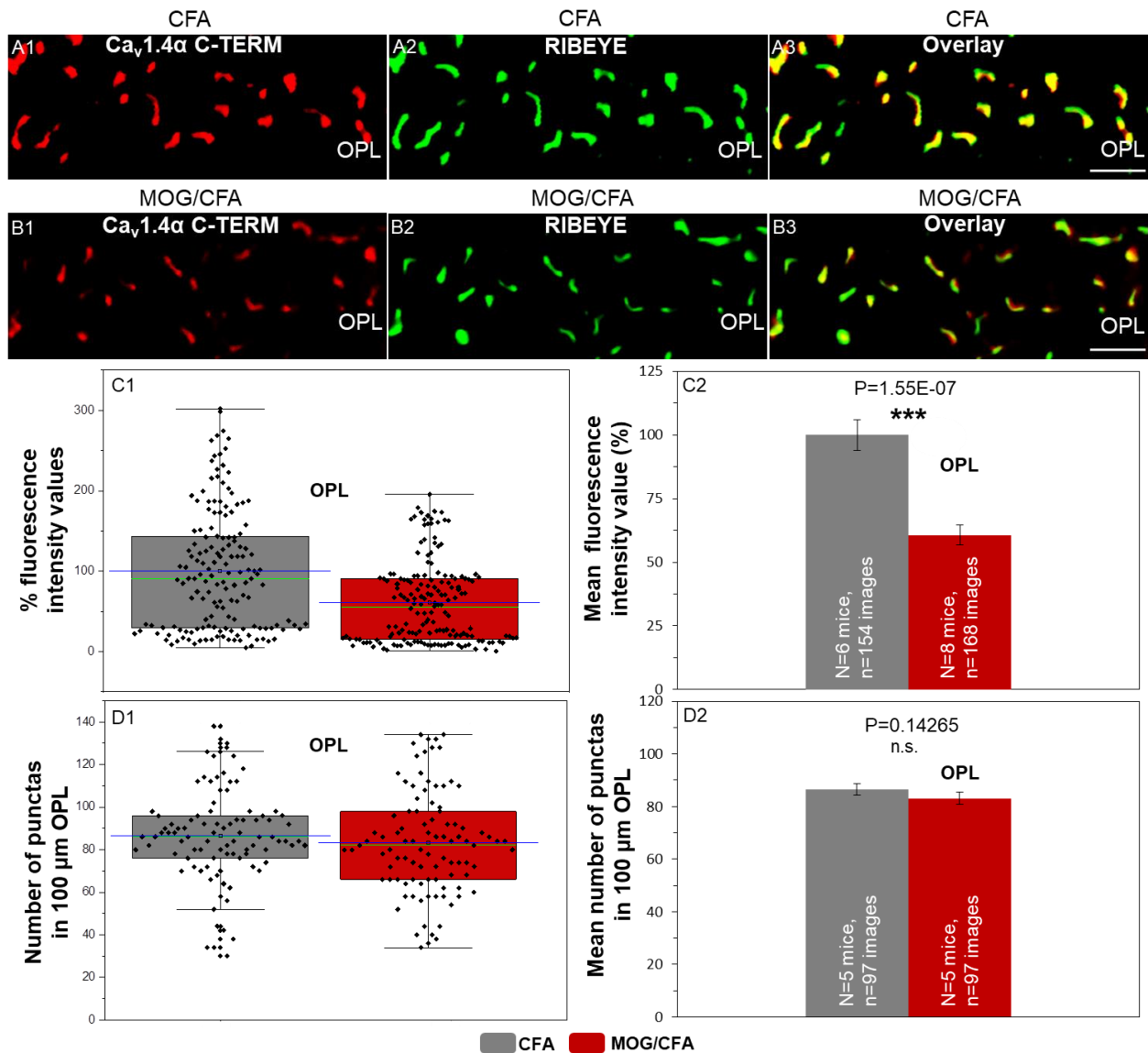


Figure 17: $Ca_v1.4\alpha$ C-term expression in retinal sections of CFA and MOG/CFA injected mice

(A1–B3) Double immunostaining with $Ca_v1.4$ specific C-term rabbit polyclonal antibody and anti-RIBEYE mouse monoclonal antibody. The former detected with donkey anti-rabbit Alexa 568 and the latter with chicken anti-mouse Alexa 488. C1

RESULTS

shows the box and whisker plots for the % fluorescence intensity values of $Ca_v1.4$ C-term at a pre-fixed ROI in the OPL of all CFA and MOG/CFA images. D1 depicts the counts for the number of punctas of $Ca_v1.4$ C-term in 100 μm length of the OPL in both CFA and MOG/CFA images. Blue and green lines in C1 and D1 represent means and medians respectively. Mean fluorescence intensity values (%) and mean count for the number of punctas in 100 μm of OPL for CFA and MOG/CFA are shown in C2 and D2 respectively. Abbreviations: OPL - outer plexiform layer, n.s.-not significant; Scale bar: 2 μm (A-B); Error bars=SEMs (C2, D2); Whiskers=1.5 times inter-quartile range (C1, D1).

3.1.2 Verification of $Ca_v1.4\alpha$ data with a second independent antibody ' $Ca_v1.4\alpha$ N-term'

We wanted to verify our $Ca_v1.4$ data with a second antibody to ensure that $Ca_v1.4$ expression was truly reduced in the EAE model mice in immunofluorescence assays. ' $Ca_v1.4\alpha$ N-term' was used for co-immunolabeling with anti-RIBEYE monoclonal antibody (2D9) on 0.5 μm thick Epon embedded CFA and MOG/CFA injected mice retinal sections. $Ca_v1.4$ N-term showed a reduced expression much like $Ca_v1.4$ C-term (Figs. 17 & 18). More than 50% reduction in fluorescence intensity of the antibody labeling at the outer plexiform layer was observed in the retina of MOG/CFA-injected mice in comparison to CFA-injected mice. The reduction was highly significant (P value=1.16E-05). Similar to the immunolabeling experiments with $Ca_v1.4$ C-term, I did not observe a reduction in the count of $Ca_v1.4$ N-term punctas in MOG/CFA-injected mice retina that could explain the decreased fluorescence intensity (Fig. 19). However in case of both the C-term and N-term antibodies I felt that the size of the punctas appeared smaller and it encouraged me to analyze them at a higher resolution.

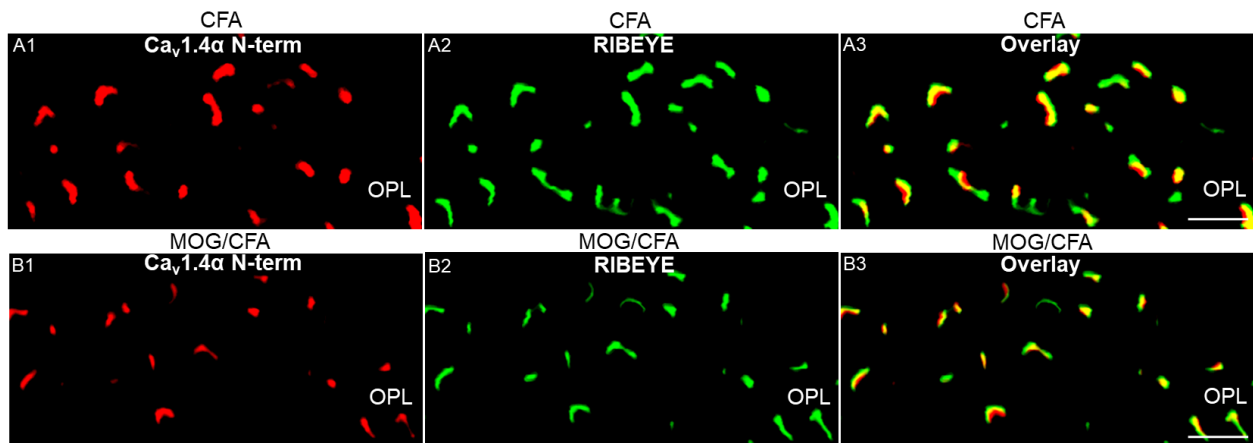


Figure 18: Immunolabeling of $Ca_v1.4\alpha$ N-term in retinal sections of CFA- and MOG/CFA-injected mice $Ca_v1.4$ N-term is double immunolabeled with anti-RIBEYE antibody on 0.5 μm thick retinal sections and detected by donkey anti-rabbit Alexa 568 and chicken anti-mouse Alexa 488 respectively (A1 to B3). Decreased immunofluorescence intensity of $Ca_v1.4$ N-term labeling at the OPL in the MOG/CFA sections is evident. Abbreviations: OPL - outer plexiform layer; Scale bar: 2 μm (A-B).

RESULTS

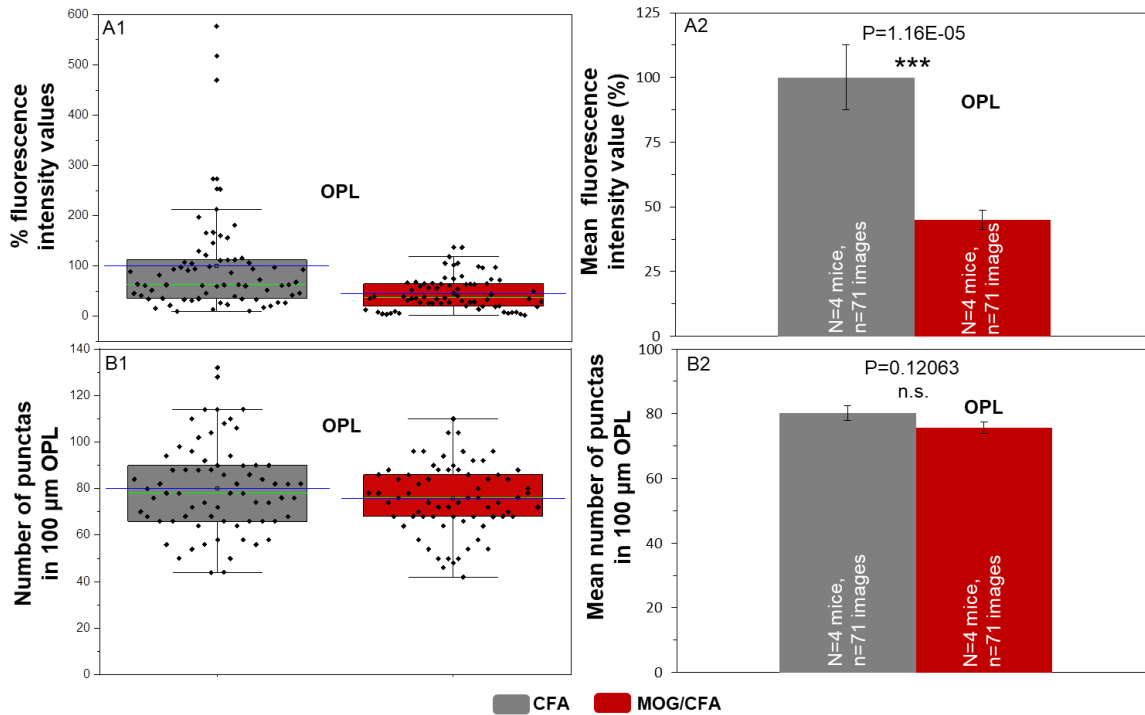


Figure 19: Quantification of $Ca_v1.4$ N-term in retinal sections of CFA- and MOG/CFA-injected mice
Percentage fluorescence intensity values of $Ca_v1.4$ N-term immunosignals for CFA and MOG/CFA are depicted in a box plot in A1, and A2 depicts their mean values. The counts for the number of punctas of $Ca_v1.4$ N-term in 100 μm of OPL for CFA and MOG/CFA are shown as a box plot in B1, and B2 represents their mean values. Blue and green lines in A1 and B1 denote the mean and median values. Abbreviations: OPL - outer plexiform layer, n.s.-not significant; Error bars=SEMs (A2, B2); Whiskers=1.5 times inter-quartile range (A1, B1).

3.1.3 High resolution analyses of $Ca_v1.4$ alpha punctas by super resolution structured illumination microscopy (SR-SIM)

Since $Ca_v1.4$ was showing weaker labeling at the OPL in MOG/CFA sections compared to the CFAs without any decrease in the count of the number of punctas, I thought of analyzing the contour length of the punctas in both the groups. I used the $Ca_v1.4\alpha$ C-term antibody for this assay. Z-stack images from 1.5 μm thick Epon embedded sections were taken through SR-SIM and then analyzed for contour length of the individual punctas. I found that while the mean contour length of the $Ca_v1.4$ punctas was approximately 1.4 μm in CFA, in case of the MOG/CFA sections it was only ~ 1 μm . The difference was very highly significant with a P value=8.03E-35. Thus I could conclude that it must be the number of $Ca_v1.4$ channel units that cluster together at the base of each individual ribbon that is going down and is responsible for the decreased fluorescence in MOG/CFA (Fig. 20).

RESULTS

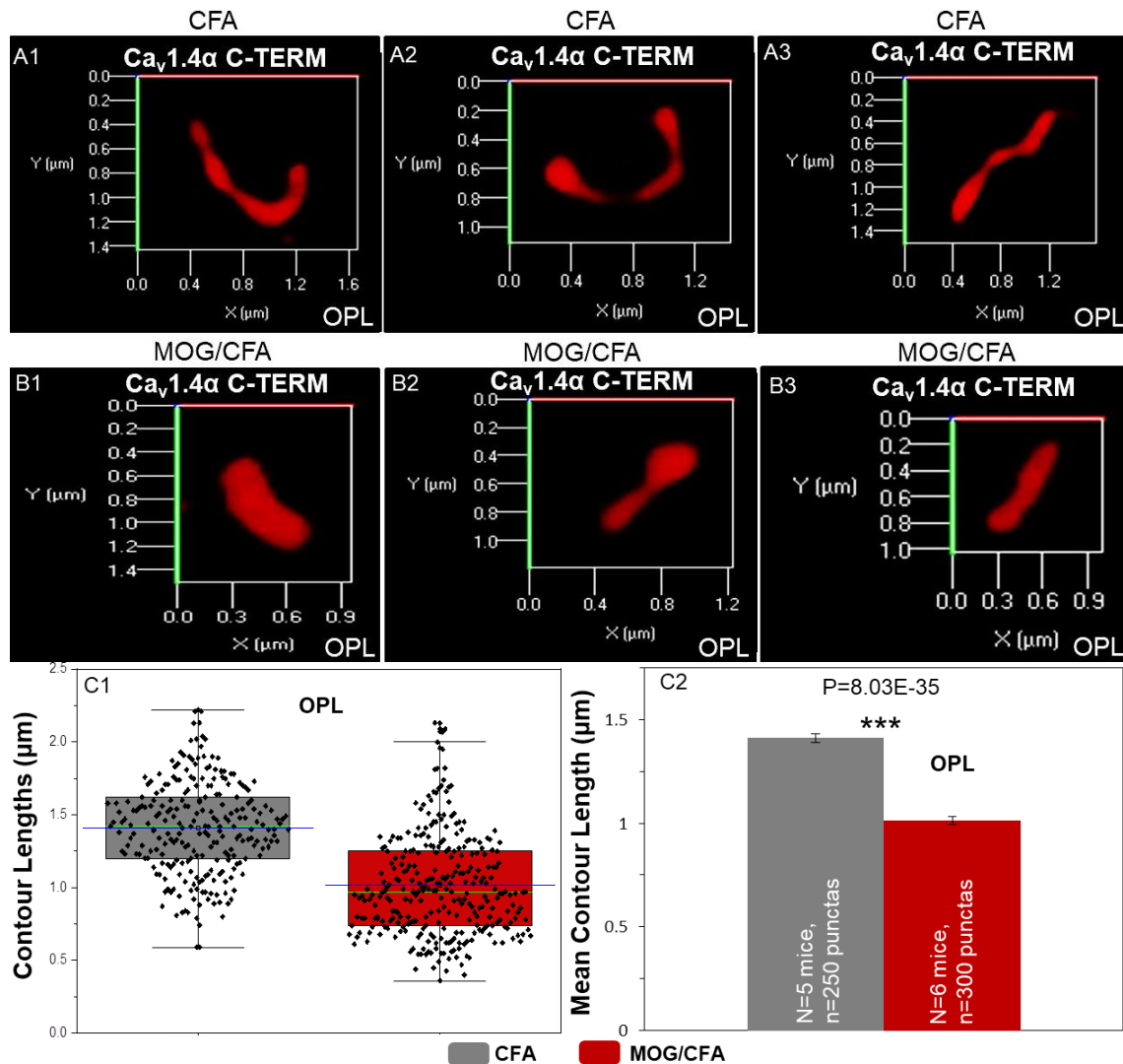


Figure 20: Contour length analyses of $Ca_v1.4\alpha$ C-term punctas in CFA and MOG/CFA injected mice retina
 $Ca_v1.4\alpha$ C-term/donkey anti-rabbit Alexa 568 labels 1.5 μ m thick retinal sections of CFA and MOG/CFA-injected mice. A1 to A3 are representative images of individual punctas at the OPL in CFA sections and B1 to B3 belong to MOG/CFA sections. C1 illustrates the contour lengths of both the groups as measured by the ZEN 2012 software in a box and whisker plot, where blue and green lines indicate the mean and median values. In C2, mean contour lengths from the two groups are represented. Abbreviations: OPL-outer plexiform layer; Error bars=SEMs (C2); Whiskers=1.5 times inter-quartile range (C1).

3.1.4 Western blot analyses of $Ca_v1.4\alpha$ expression in EAE and control retinas

To analyze the overall protein expression of $Ca_v1.4$ in retinal lysates of EAE mice, Western blot analysis was performed. $Ca_v1.4\alpha$ N-term antibody gave a band at \sim 160 kDa mark that most likely represented full-length $Ca_v1.4$. Subsequently fodrin used on the same blot strip showed a single band at about 230 kDa. However, unlike in immunofluorescence, here I could see no obvious changes in band intensities in case of MOG/CFA. I quantified the bands with ImageJ software, normalizing $Ca_v1.4$ band intensities with respective fodrin bands. Fodrin being a globally expressed

RESULTS

cytoskeletal protein was used as a loading control for both the retinal lysates (Glenney Jr & Glenney, 1983; Grabner et al., 2015). The normalized mean band intensity of Ca_v1.4 for MOG/CFA was reduced by 8% in retinas of MOG/CFA-injected mice in comparison to retinas from CFA-injected control mice (Fig. 21). De Winter, 2013 had shown that when sample sizes are small but within-pair correlation is high (Pearson's correlation coefficient ≥ 0.8), it is possible to conduct a paired t-test. Since the sample size of my normally distributed blot data was small, I accordingly computed the Pearson's correlation coefficient between the pairs in MS-Excel. Pearson's correlation coefficients (r) for Ca_v1.4, fodrin and Ca_v1.4 normalized by fodrin were found to be 0.852193, 0.977326 and 0.944925 respectively. Hence, a two-tailed paired t-test was performed on the normally distributed data in all the three cases. For MOG/CFA vs CFA, normalized Ca_v1.4 yielded a P value=0.113361, while that for absolute Ca_v1.4 full length and fodrin were 0.070851 and 0.528844 respectively. This data suggested that the overall Ca_v1.4 α protein expression level was not disturbed in the EAE mice retina; however the protein was not being clustered into as many calcium channels as are usually present in a normal healthy mouse retina. That is why the punctate labelings for Ca_v1.4 channel clusters were smaller in MOG/CFA retina.

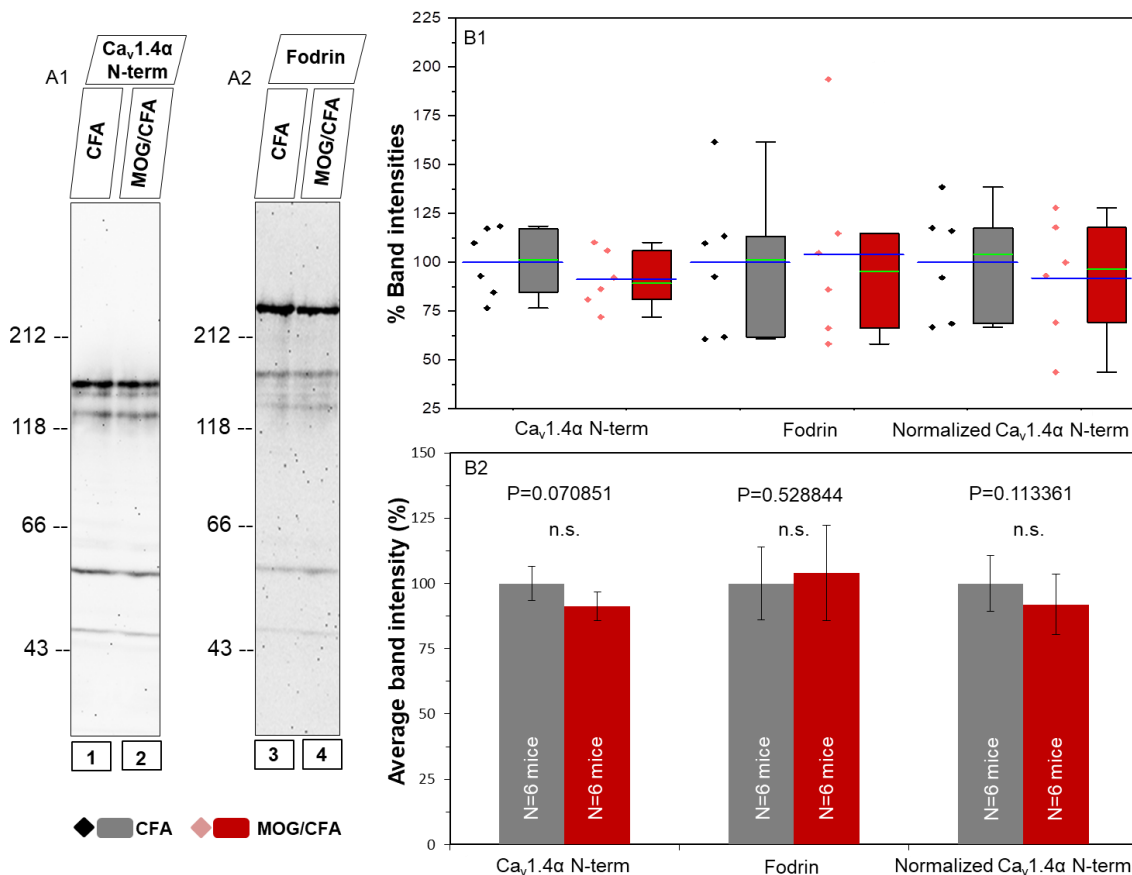


Figure 21: Western blot analyses for Ca_v1.4 N-term in CFA and MOG/CFA injected mice retinal lysates
A1 and A2 are blots of Ca_v1.4 alpha and fodrin on CFA and MOG/CFA mice retinal lysates separated by SDS-PAGE using a dis-

RESULTS

continuous running gel (7% on 10% acrylamide). A1(1 and 2) shows the full length bands for Ca_v 1.4 alpha at ~160 kDa in the CFA and MOG/CFA blot lanes respectively. A2 (3 and 4) are the blot lanes of the same strip (A1) showing the bands for fodrin at ~230 kDa. B1 represents the box plots for the % band intensities of Ca_v1.4, fodrin and Ca_v 1.4 normalized by fodrin in the the two groups. Mean and median of the band intensities are indicated by blue and green lines respectively. In B2 mean band intensities for Cav1.4, fodrin and Ca_v1.4 normalized by fodrin in CFA and MOG/CFA retinal blots have been illustrated. Abbreviation: n.s.-not significant; Error bars = SEMs (B2); Whiskers=1.5 times inter-quartile range (B1).

3.2 Ca_vβ2 expression in photoreceptor synapses of MOG/CFA-injected (EAE) and CFA-injected (control) mice

Besides the main pore-forming α1F subunit of Ca_v1.4 channel, other cytoplasmic auxiliary subunits α2δ4 and β2 exist in photoreceptor terminals that determine the channel kinetics. Ca_vβ2 is also responsible for membrane targeting and expression of the α1F subunit (Ball et al., 2002). Absence of Ca_vβ2 shows an abnormal ERG similar to that of Ca_v1.4α KO, loss of ribbon synapses and thinning of the OPL (Ball et al., 2002; Ball & Gregg, 2002; Katiyar et al., 2015). On finding drastic changes in the expression pattern of Ca_v1.4 α in the EAE retina, I was encouraged to evaluate Ca_vβ2 too in a similar fashion through confocal microscopy, SR-SIM and western blot analyses.

3.2.1 Immunolabeling and quantification of Ca_vβ2 antibody (No.1) in EAE retina

Rabbit polyclonal Ca_vβ2 antibody (No.1) was coimmunolabeled with anti-RIBEYE monoclonal antibody (2D9) on 0.5 μm thick CFA and MOG/CFA injected mice retinal sections and images were acquired through confocal microscopy. On quantifying its fluorescent signals just at the base of the ribbon in the OPL, I found a similar decrease in its fluorescence intensities in MOG/CFA mice retinas in comparison to retinas from CFA-injected control mice, similarly as described above for the pore-forming α-subunit. The mean fluorescence intensity of Ca_vβ2 signals in MOG/CFA was significantly reduced by ≈25% compared to CFA (P value=0.00719). Moreover on counting the Ca_vβ2 (No.1) punctas, no difference in the count per 100 μm of OPL was observed in the two groups (Fig. 22). Before proceeding to analyze the puncta contour lengths in CFA and MOG/CFA sections, I verified the Ca_vβ2 data with a second independent antibody Ca_vβ2 (No.2). Here too, I focused on the mice that were sacrificed 9days after immunization.

RESULTS

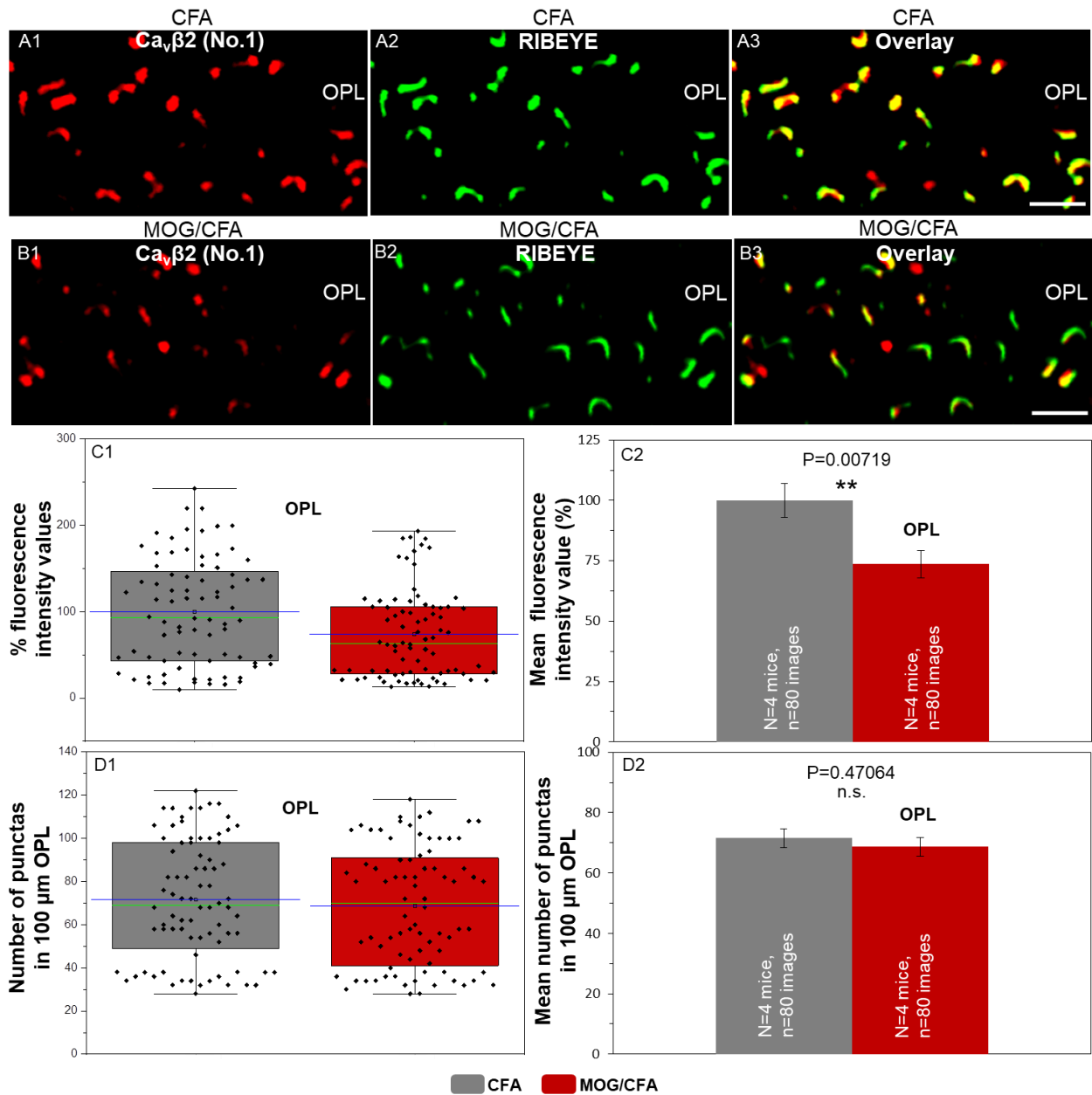


Figure 22: $Ca_v\beta 2$ (No.1) immunolabeling and analyses in CFA and MOG/CFA mice retinal sections

A1 & B1 show $Ca_v\beta 2$ /donkey anti-rabbit Alexa 568 labeling at the OPL in CFA and MOG/CFA sections respectively and A2 & B2 show ribbon labeling with RIBEYE/chicken anti-mouse Alexa 488 likewise. A3 and B3 depict the merged images of CFA and MOG/CFA in the same order. The fluorescence intensities of $Ca_v\beta 2$ and RIBEYE appear diminished in the MOG/CFA sections compared to CFA. The percentage fluorescence intensities of $Ca_v\beta 2$ for the CFA and MOG/CFA sections at a particular ROI in the OPL are depicted in a box and whisker diagram in C1. The count for the number of punctas of $Ca_v\beta 2$ per 100 μm OPL in both the groups are shown in D1. The blue and green lines in C1 and D1 represent the mean and median values respectively. Mean fluorescence intensities (%) and mean counts of the number of punctas for the control and EAE mice are illustrated in figures C2 and D2. Abbreviations: OPL-outer plexiform layer; n.s.-not significant; Scale bar: 2 μm (A-B); Error bars = SEMs (A2, B2); Whiskers=1.5 times inter-quartile range (C1, D1).

RESULTS

3.2.2 Second independent Ca_vβ2 antibody (No.2) corroborates previous Ca_vβ2 data

A second independent affinity purified rabbit polyclonal Ca_vβ2 antibody 'No.2' and anti-RIBEYE mouse monoclonal antibody (2D9) were used to double immunolabel 0.5μm thick CFA and MOG/CFA mice retinal sections to confirm the labeling pattern of the previous Ca_vβ2 antibody. Confocal images of Ca_vβ2 (No.2) were acquired and analyzed using the ImageJ software to measure its fluorescence intensity and to count its number of punctas in 100 μm length of OPL. The mean fluorescence intensity for Ca_vβ2 (No.2) at the OPL in MOG/CFA sections was significantly less than that of CFA sections by ~40%, (P value=5.70E-09). Similar to Ca_vβ2 (No.1), Ca_vβ2 (No.2) also exhibited no difference in the number of punctas between the two groups of mice (Fig. 23).

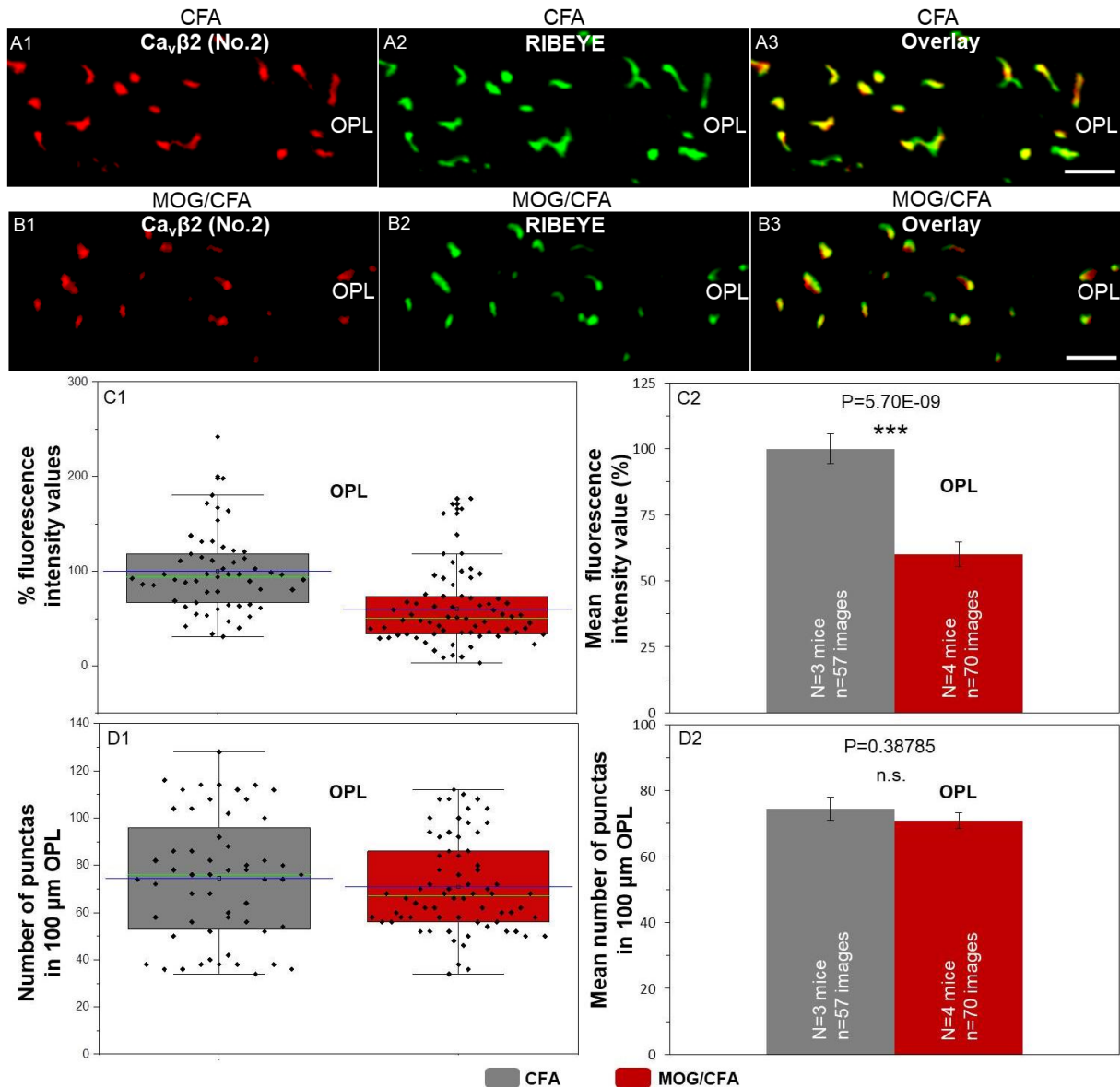


Figure 23: Analyses of Ca_vβ2 (No.2) in CFA and MOG/CFA injected mice retinal sections

A1, A2 and B1, B2 are the single channel labelings for Ca_vβ2 (No.2)/donkey anti-rabbit Alexa 568 and RIBEYE/chicken anti-

RESULTS

mouse Alexa 488, and A3 and B3 represent the merged images. $Ca_v\beta 2$ shows diminished fluorescence in images of the EAE retina. C1 depicts the distribution of the % fluorescence intensity values through a box plot and the mean values are represented in C2. D1 is the box plot distribution for the count of number of punctas of $Ca_v\beta 2$ in 100 μm of OPL in the control and EAE retina. D2 compares the mean counts of number of punctas for the two groups. Blue and green lines in C1 and D1 indicate mean and median values respectively. Abbreviations: OPL-outer plexiform layer, n.s.-not significant; Scale bar: 2 μm (A-B); Error bars = SEMs (C2, D2); Whiskers=1.5 times inter-quartile range (C1, D1).

3.2.3 High resolution analyses of contour length of $Ca_v\beta 2$ punctas by super resolution structured illumination microscopy (SR-SIM)

To investigate the decreased fluorescence of $Ca_v\beta 2$ labeling in the OPL of EAE mice retina I took the help of SR-SIM microscopy. 1.5 μm thick sections were immunolabeled with $Ca_v\beta 2$ (No.1) antibody and donkey anti-rabbit Alexa 568 as its secondary. Images of $Ca_v\beta 2$ punctas in CFA and MOG/CFA injected mice retina were acquired at a higher resolution and its lengths were analyzed (Fig. 24). It was evident that contour lengths of $Ca_v\beta 2$ punctas in MOG/CFA mice were shorter than that in CFA mice. While mean length of the punctas in CFA is $\sim 1.4 \mu m$, $Ca_v\beta 2$ punctas in MOG/CFA retina reach $\sim 1.1 \mu m$. The mean values of the two groups are significantly different (P value=1.418E-23) (Fig. 25). The reduced contour lengths of $Ca_v\beta 2$ as well as $Ca_v 1.4 \alpha 1F$ in EAE retina suggest that the number of Ca_v channels that cluster together beneath each individual ribbon must be decreasing. However, no ribbon in the EAE retina was losing its complete cluster of $Ca_v 1.4$ channels. Thus, I could conclude that the shorter sized punctate labelings of $Ca_v\beta 2$ and $Ca_v 1.4 \alpha$ were responsible for the respective reduced fluorescence intensities in retina of MOG/CFA injected mice.

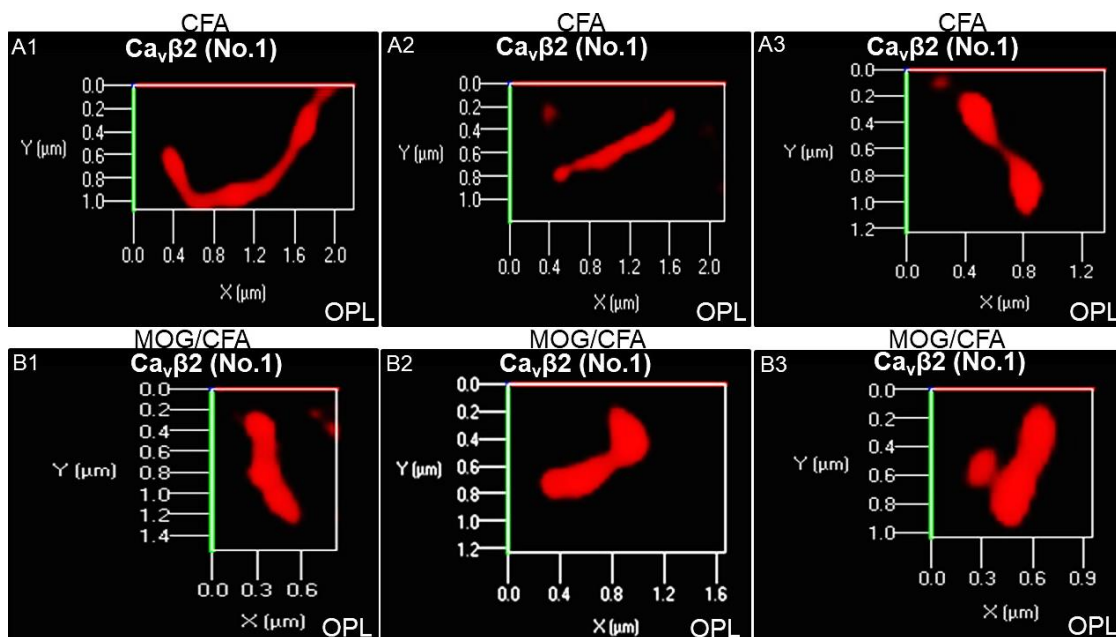


Figure 24: SR-SIM images of $Ca_v\beta 2$ (No.1) punctas in CFA and MOG/CFA injected mice retinal sections
 $Ca_v\beta 2$ (No.1)/ donkey anti-rabbit 568 was used to immunolabel 1.5 μm thick retinal sections. A1 to A3 are the representative

RESULTS

images of $Ca_v\beta 2$ punctas of CFA-injected mice retinal sections and B1 to B3 represent MOG/CFA.

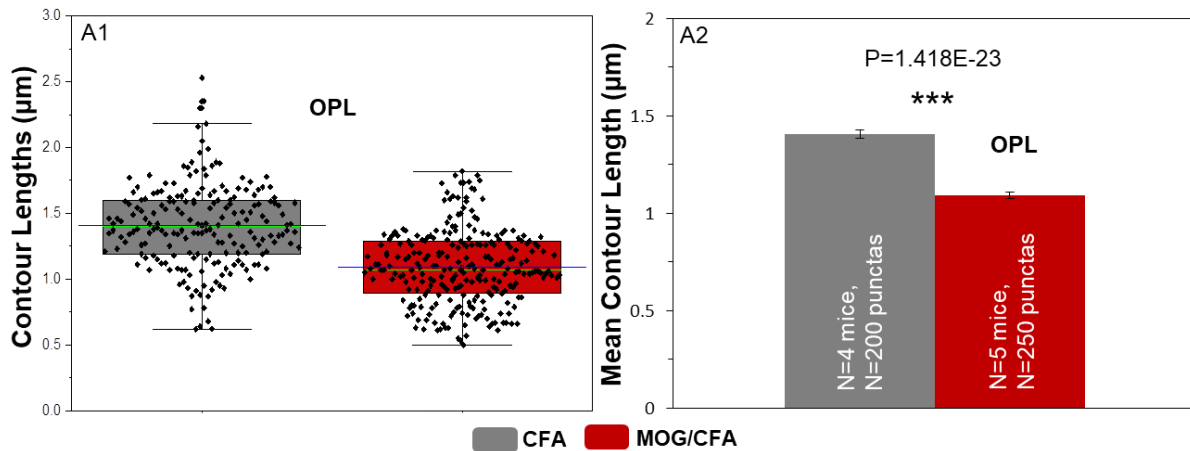


Figure 25: Contour-length analyses of $Ca_v\beta 2$ (No.1) punctas in CFA and MOG/CFA mice retinal sections
Individual contour lengths of $Ca_v\beta 2$ (No.1) punctas in CFA and MOG/CFA injected mice retinal sections are represented in a box plot in A1. In A1 blue and green lines represent the mean and median values respectively. Mean contour lengths of the $\beta 2$ punctas of CFA and MOG/CFA mice retinas are compared in A2. Abbreviations: OPL-outer plexiform layer; Error bars=SEMs (A2); Whiskers=1.5 times inter-quartile range (A1).

3.2.4 Western blot analyses of $Ca_v\beta 2$ expression in EAE and control mice retinas

To quantify the overall protein expression of $Ca_v\beta 2$ in EAE mice retina, Western blot analysis of the CFA and MOG/CFA injected mice retinal lysates was performed and the band intensities for $Ca_v\beta 2$ were compared. In retinal blots $Ca_v\beta 2$ (No.2) antibody gives a single band at ~60 kDa mark (Katiyar et al., 2015). The 118 kDa to >212 kDa part of the blot was used for RIM1,2, while the lower part of the blot strip was incubated with $Ca_v\beta 2$ (No.2) antibody. Actin was later used as a loading control for the lysates. Its band comes at ~43 kDa. Mean band intensity of $Ca_v\beta 2$ normalized by actin in MOG/CFA was reduced by ~10% against CFA (Fig. 26). With a small sample size and high within-pair correlations (Pearson's correlation coefficient ≥ 0.8), it is possible to perform two-tailed paired t-test for normally distributed data (De Winter, 2013). On evaluating the relationship of normalized band intensities of $Ca_v\beta 2$ in CFA and MOG/CFA, I found a Pearson correlation coefficient (r) of 0.850568. Absolute $Ca_v\beta 2$ and actin also showed high Pearson correlation coefficients (r) of 0.8065588 and 0.77772 (≈ 0.8), yielding P values of 0.119732 and 0.450056 respectively. Mean band intensity of $Ca_v\beta 2$ normalized by actin in MOG/CFA exhibited a weak significant reduction compared to CFA (P value=0.035362) (Fig. 26). Thus though total $Ca_v 1.4$ alpha expression remains unaltered in EAE mice retina at a preclinical phase, total $Ca_v\beta 2$ expression in MOG/CFA undergoes a significant reduction. The difference in total expression levels of $Ca_v\beta 2$ and $Ca_v 1.4$ alpha relative to each other in EAE can possibly be explained by the fact that β

RESULTS

subunits have been observed to operate in modulation of intracellular calcium concentration independent of its role as a Ca_v channel subunit (Belkacemi et al., 2018).

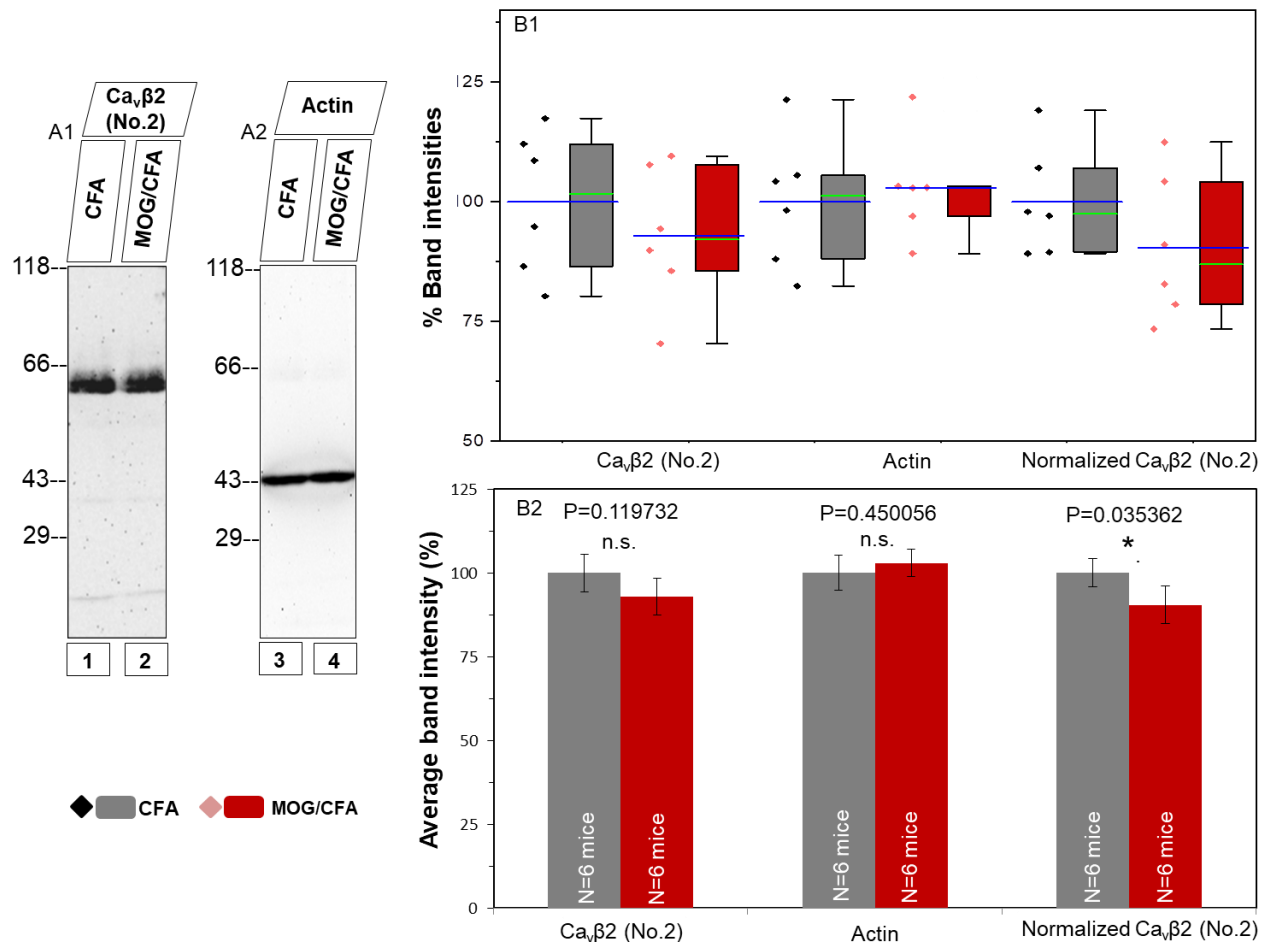


Figure 26: Western blot analyses for $Ca_v\beta2$ (No.2) antibody in EAE mice retinal lysates

A1 and A2 are blots of $Ca_v\beta2$ and actin on CFA and MOG/CFA injected mice retinal lysates separated by SDS-PAGE using a discontinuous running gel (7% on 10% acrylamide). $Ca_v\beta2$ bands at ≈ 60 kDa are visible in A1 (lanes 1 and 2 for CFA and MOG/CFA respectively) and A2 shows the blot lanes of the very same strip with loading control actin at 43 kDa in lanes 3 and 4. The % band intensities of $Ca_v\beta2$, actin and $Ca_v\beta2$ normalized by actin in the two groups are illustrated through a box plot in B1. Mean and median of the band intensities are shown by blue and green lines respectively. The mean band intensities for $Ca_v\beta2$, actin and $Ca_v\beta2$ normalized by actin in the two groups are compared in B2. Abbreviations: n.s.-not significant; Error bars = SEMs (B2); Whiskers=1.5 times inter-quartile range (B1).

3.3 Evaluation of depolarization-evoked Ca^{2+} influx in EAE mice retina

Since I could see a disturbance in $Ca_v1.4$ channel focal distribution through immunofluorescence assays I wanted to find out whether such disturbances were getting extrapolated to the level of physiological Ca^{2+} influx through the channels. Moreover, Dembla et al., 2018 had observed decreased vesicular cycling in EAE photoreceptor synapses at a preclinical phase. Since exocytosis

RESULTS

is a calcium mediated process, it further encouraged me to explore the calcium influx machinery in EAE photoreceptor terminals. I compared Ca^{2+} influx on depolarization with high K^+ solution in CFA and MOG/CFA mice retinal slices at the OPL by using Fura2-AM as the calcium indicator dye (Mauleon et al., 2013; Cameron et al., 2016).

3.3.1 Depolarization-evoked Ca^{2+} influx measurement on day9 after induction

Keeping in line with my immunofluorescence data, I first performed a series of depolarization experiments on retinal slices of the control and EAE animals on day 9 after the injections. Both CFA and MOG/CFA injected mice were recorded on the very same day. I found that Ca^{2+} influx as per the rise in ratiometric (340/380) fluorescence of Fura2 at 515 nm was less in MOG/CFA retinal slices compared to the CFA ones. Not only did I find a decrease in the mean amplitude of the depolarization responses in MOG/CFA slices, mean slope of the rise in fluorescence for MOG/CFA was gentler compared to CFA. To better analyze the responses, I curve fitted each individual response in Igor Pro software. The mono exponential fit seemed to fit best (Fig. 27). After deriving amplitude and time constant (τ) values for the rise and kinetics of the response, I analyzed them to get the mean amplitude and time constants for both the groups. The amplitude was significantly less in MOG/ CFA while the time constant (τ) was significantly higher. The mean amplitudes and mean τ values of the two groups differed significantly with a P value=3.22E-09 and 1.45E-04 respectively (Fig. 28).

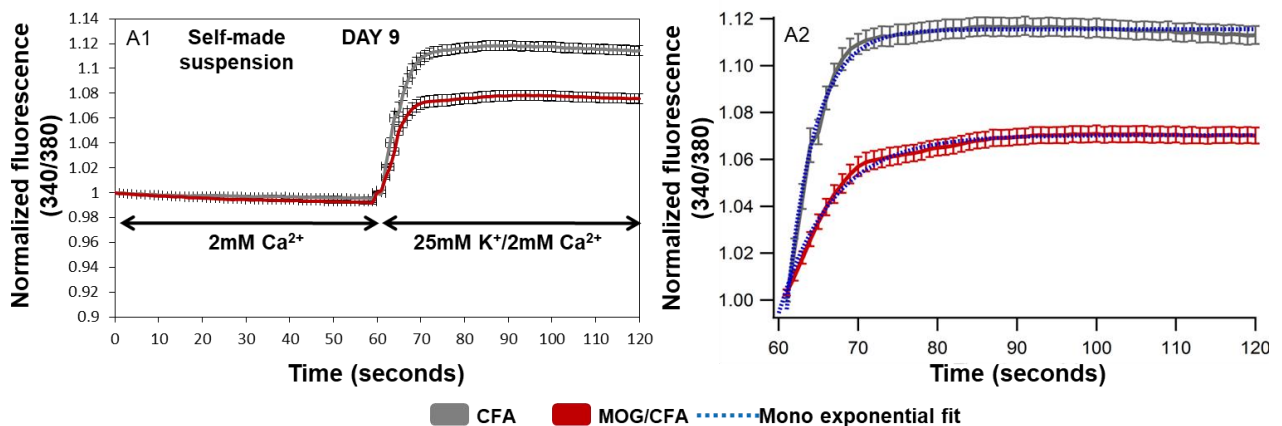


Figure 27: Fura2-AM recordings of CFA and MOG/ CFA mice retinal slices on day 9 after injection

A1 shows the Ca^{2+} influx traces for CFA and MOG/CFA, in response to 25 mM KCl/2 mM Ca^{2+} depolarizing solution. A2 delineates the mono exponential fits of the average CFA and MOG/CFA depolarization response traces in blue. Error bars=SEMs (A1, A2); Acquisition frequency=1 Hz.

RESULTS

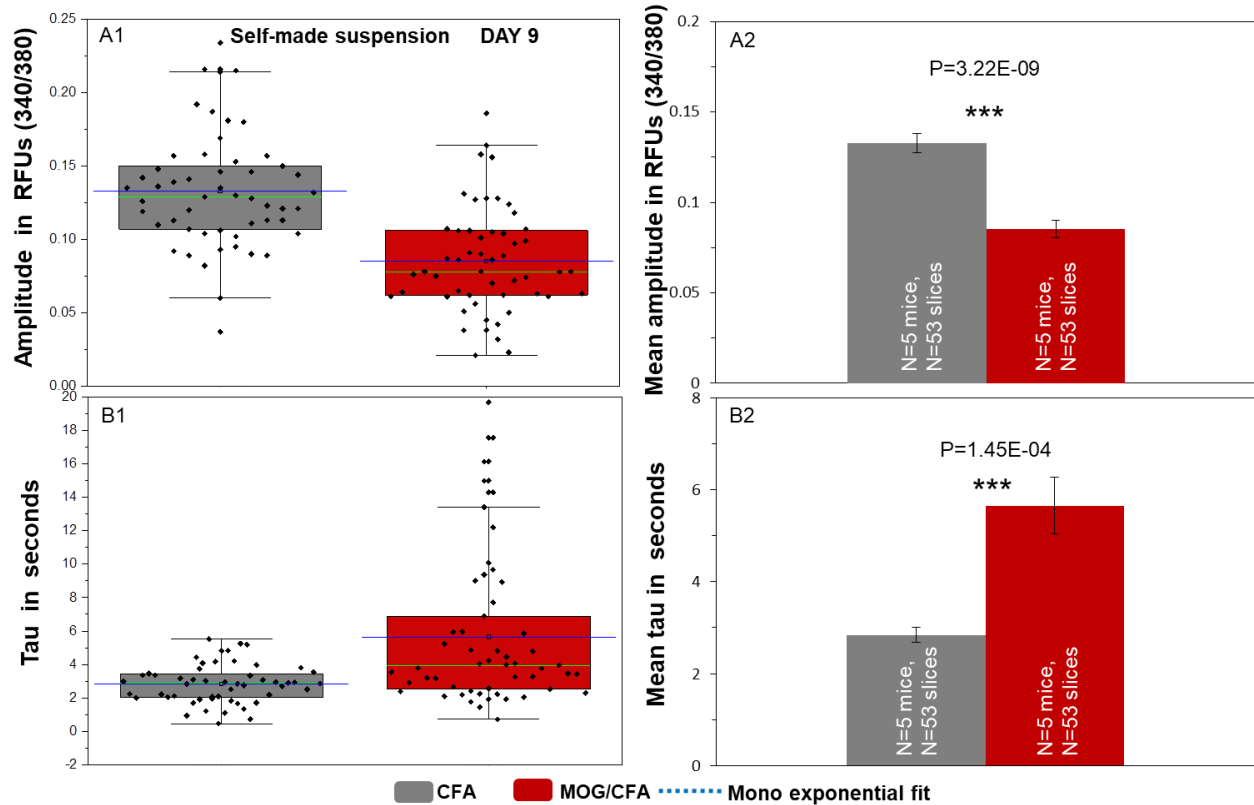


Figure 28: Fura2-AM analyses of CFA and MOG/CFA mice retinal slices on day 9 after immunization
The individual amplitude values are denoted in a box and whisker plot in A1 and the tau values in B1, with the blue and green lines indicating the mean and median values respectively. Mean amplitudes and time constants for CFA and MOG/CFA traces are depicted in B2 and C2 respectively. Acquisition frequency=1 Hz; Error bars=SEMs (A2, B2); Whiskers=1.5 times inter-quartile range (A1, B1).

3.3.2 Analysis of depolarization-evoked Ca^{2+} influx at earlier time points (days 7 and 8 after immunization)

Encouraged by the Ca^{2+} influx data of day 9, I was curious to find out whether these physiological changes were occurring at even earlier time points. With this purpose in mind I repeated the same experiment with Fura2-AM loaded retinal slices on days 7 and 8 after the injections. On both the days I could see a similar reduced Ca^{2+} influx response with slower kinetics in the MOG injected mice, as on day 9 after injection. Thus, degradative changes start occurring in photoreceptor terminals as early as day 7, even before clinical symptoms of EAE appear in the MOG/CFA mice. After carrying out the curve fitting of the individual responses, I found that mono exponential curves fit the traces best for both days 7 and 8, as it was with day9 (Figs. 29 & 30). A significant decrease in the mean amplitude of the depolarization response was observed in MOG/CFA mice compared to CFA for both the days. The P values for the amplitudes on days 7 and 8 are 1.15E-11

RESULTS

and $3.49\text{E-}08$ respectively. The kinetics of the rise of Ca^{2+} concentration in photoreceptor terminals was also found to be much slower in MOG/CFA against CFA. P values for the time constants of CFA and MOG/CFA on days 7 and 8 are $1.34\text{E-}05$ and $1.71\text{E-}04$ respectively (Figs. 29 & 30).

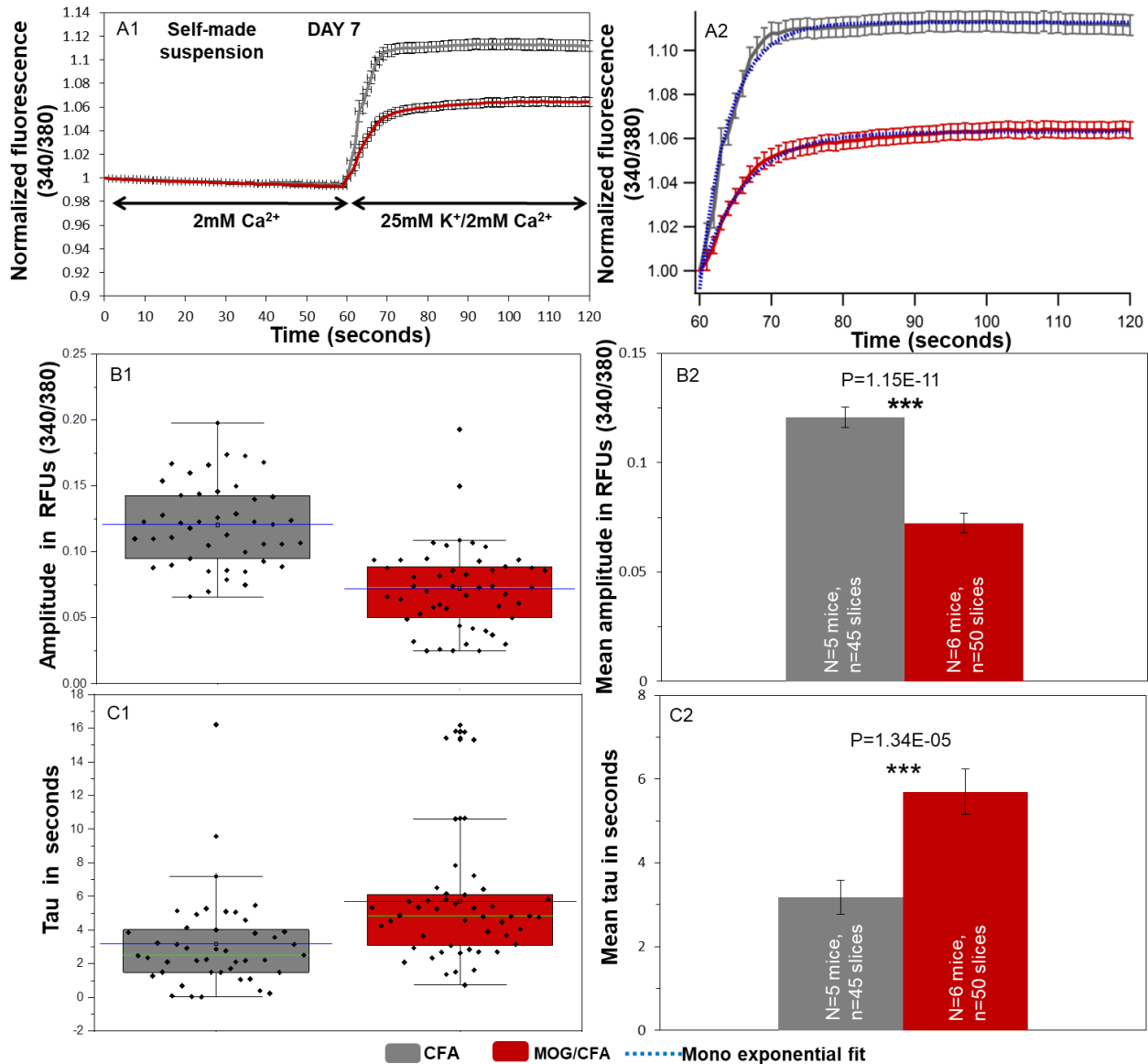


Figure 29: Fura2-AM measurements in CFA and MOG/CFA injected mice retina on day 7 after injection
A1 shows the increase in ratiometric fluorescence of Fura2-AM in CFA and MOG/CFA retinal slices on depolarization with 25mM KCl. The monoexponential fits of the mean CFA and MOG/CFA responses are shown in A2 in blue. The amplitudes of the individual responses of the control and EAE mice retinal slices are depicted in a box plot in B1 and their mean time constant values in C1. The blue and green lines in B1 and C1 denote the mean and median values respectively. The mean amplitude of the MOG/CFA responses is significantly smaller than that in the CFAs, while the mean tau of MOG/CFA in turn is significantly higher (B2 and C2 respectively). Acquisition frequency=1 Hz; Error bars = SEMs (A1, A2, B2, C2); Whiskers=1.5 times inter-quartile range (B1, C1).

RESULTS

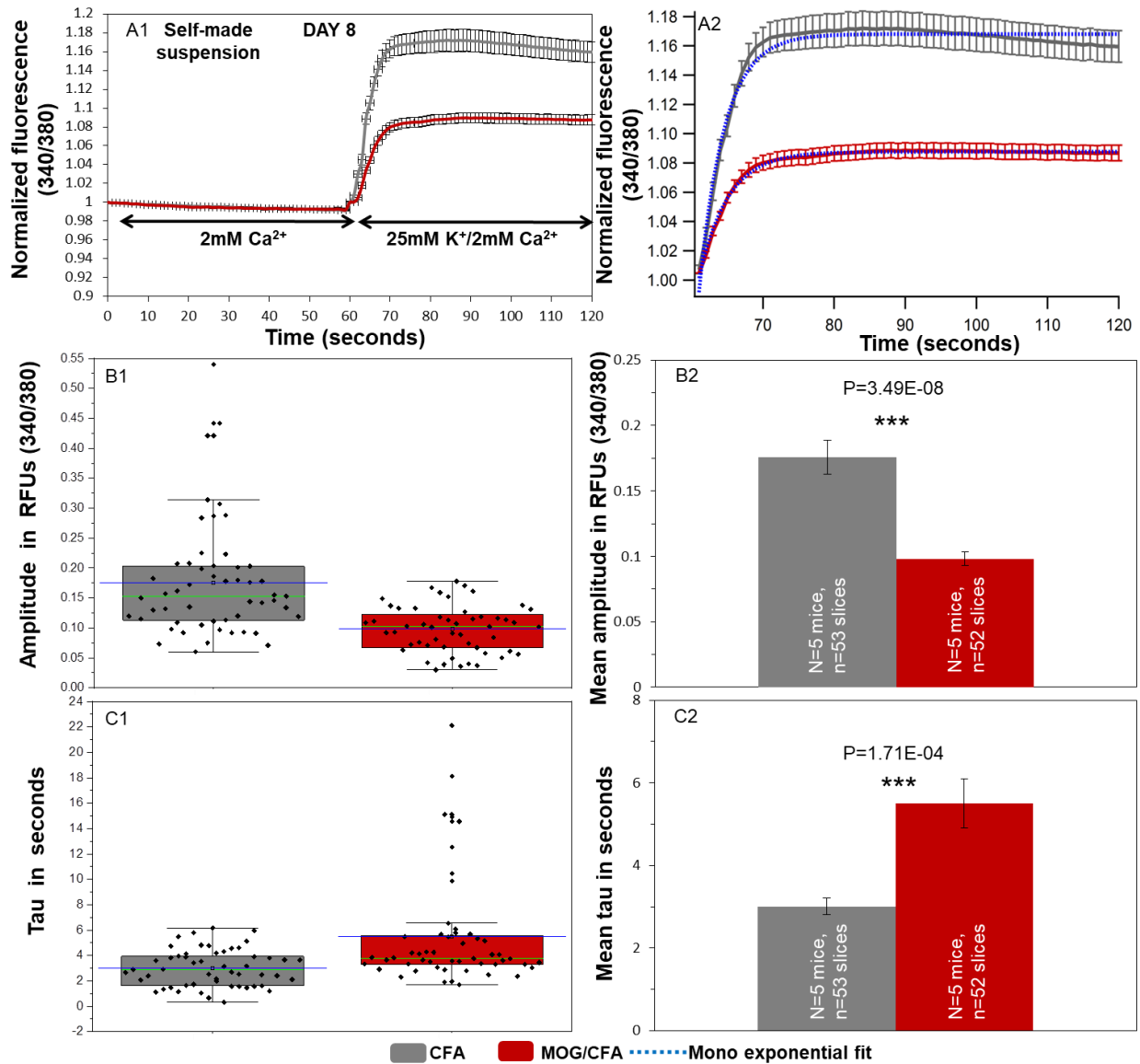


Figure 30: Fura2-AM measurements in CFA and MOG/CFA mice retinal slices on day 8 after injection
A1 shows the Ca²⁺ influx traces for CFA and MOG/CFA, in response to 25mM KCl/2mM Ca²⁺ depolarizing solution. A2 delineates the mono exponential fits of the average CFA and MOG/CFA depolarization response traces in blue. B1 and C1 illustrate the individual response amplitudes and time constants of CFA and MOG/CFA in a box plot distribution with mean and median values marked out in blue and green lines respectively. B2 compares the mean response amplitudes of CFA and MOG/CFA traces and C2 depicts the mean tau values of the two groups. Acquisition frequency=1 Hz. Error bars=SEMs (A1, A2, B2, C2); Whiskers=1.5 times inter-quartile range (B1, C1).

3.3.3 Comparing amplitudes and time constants of MOG/CFA depolarization-evoked Ca²⁺ influx responses over days 7, 8 and 9

Finally I wanted to see whether the amplitude and the tau values of the MOG/CFAs were varying significantly over the days. With the mean CFA amplitude and tau set to 100, the % values of MOG

RESULTS

amplitudes and taus were calculated for all the three days, thus normalizing them with respect to the CFA values. Since the data values were not normally distributed, the Kruskal–Wallis ANOVA test was performed on the normalized values of amplitudes and taus of the MOG/CFAs for days 7, 8 and 9. It showed that they were not varying significantly over the days. The P value for the amplitude was 0.37926 and that for the tau, 0.76498 (Fig. 31).

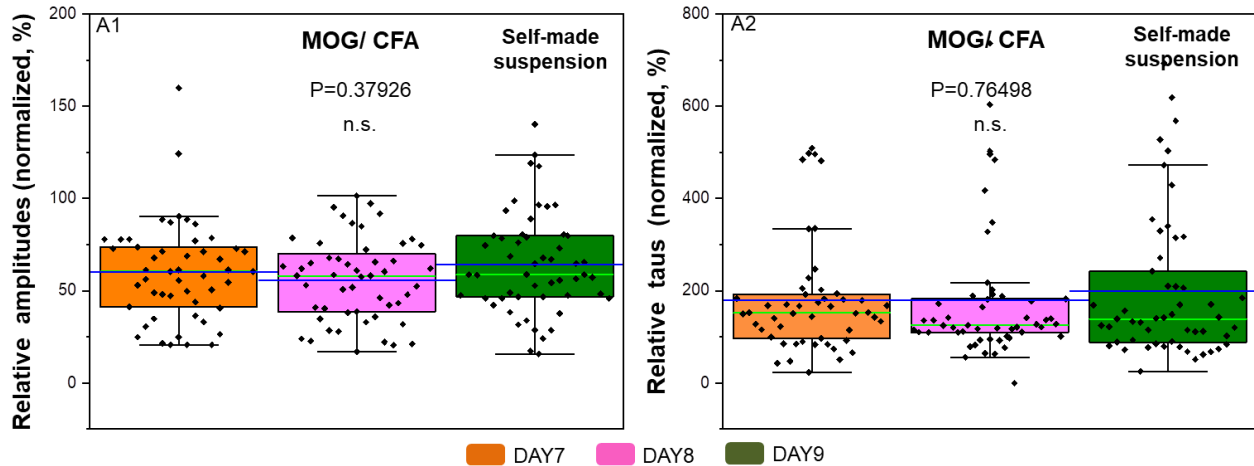


Figure 31: Comparison of Ca^{2+} influx amplitudes and kinetics in MOG/CFA injected mice retinal slices over days 7 to 9 after immunization

% values of MOG/CFA depolarization-evoked Ca^{2+} influx amplitudes for days 7, 8 and 9 with respect to respective mean CFA amplitudes are plotted in a box and whisker diagram in A1. A2 shows the same for the time constants of MOG/CFA depolarization responses. Mean and median values for the amplitudes and the taus are represented in blue and green lines respectively. The mean amplitudes and taus were found not to differ significantly in the MOGs with respect to their respective mean CFA values over days 7, 8 and 9. Abbreviation: n.s.-not significant; Whiskers=1.5 times inter-quartile range (A1, A2).

3.3.4 Confirmation of the results with a commercially available EAE injection system

A homemade version of the MOG₃₅₋₅₅ peptide (Seq. MEVGWYRSPFSRVVHLYRNGK) in an emulsion with Complete Freund's Adjuvant (CFA) was used and subsequent intraperitoneal injection of Pertussis toxin was given to induce EAE (experimental autoimmune encephalitis) in 10 weeks old C57Bl/6 female mice. The control mice had no MOG₃₅₋₅₅ peptide in their injections. The induction worked efficiently and I could also see effects of the disease through my experiments at as early day points as day7. However, there was a need to ensure that whatever effects I observed were not a result of some contaminant arising in the injectable preparations. For this purpose Hooke Laboratories premade ready to use commercial kit (# EK 2110) for CFA and MOG₃₅₋₅₅/CFA emulsions with PTX was also used to induce EAE. After inducing EAE in the 10 weeks old C57Bl/6 female mice with the preparations from the commercial kit, I used these mice for my calcium imaging experiments with FURA2. To doubly ensure our data and to rule out all suspicions we did the Ca^{2+} recordings on all the three days, day7, day8 and day9. Similar to the self-made MOG

RESULTS

peptide injected mice responses, I observed that depolarization responses of the Hooke's kit MOG injected mice retinal slices was lower in amplitude and slower in kinetics compared to its corresponding control slices. Mono exponential curve fittings for individual depolarization response traces of CFA and MOG/CFA for all the 3 days were performed using Igor pro (Fig. 32). It provided the individual amplitude and time constant values for each response trace.

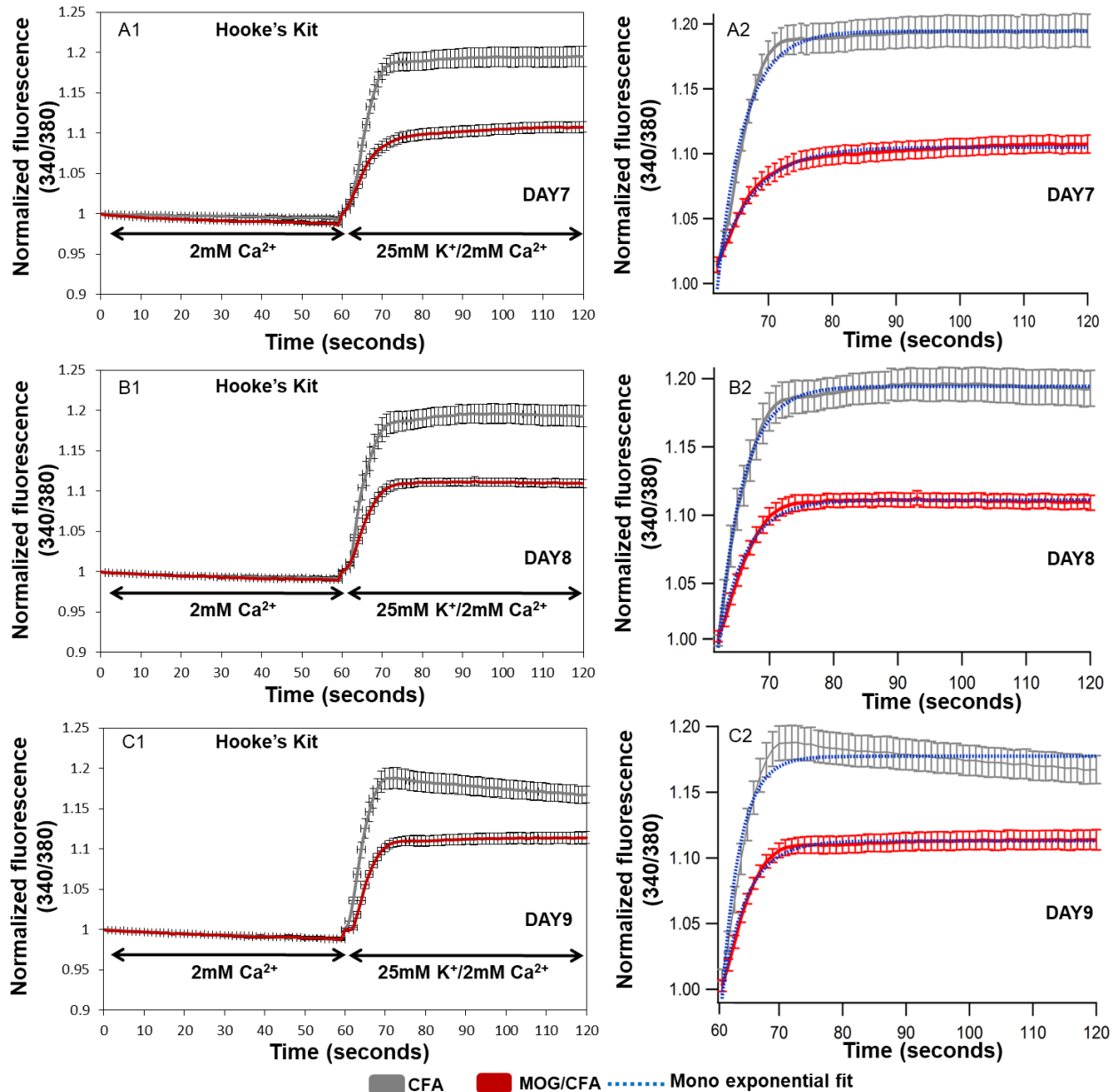


Figure 32: Depolarization-evoked Ca^{2+} influx measurements in commercial CFA and MOG/CFA injected mice retinal slices

Panels A, B and C depict Ca^{2+} influx data for retinal slices of mice injected with Hooke's Laboratories commercial CFA and MOG emulsions on days 7, 8 and 9 after the injections respectively. A1, B1 and C1 illustrate the ratiometric fluorescence increase in FURA2 in response to depolarization with 25mM KCl. The mono exponential fits of the average response traces of

RESULTS

CFA and MOG/CFA for days 7, 8 and 9 are delineated in blue in A2, B2 and C2 respectively. Acquisition frequency=1 Hz; Error bars=SEMs (A1, A2, B1, B2, C1, C2).

For further analysis the mean amplitude and the mean tau was calculated for CFA and MOG/CFA mice for each of the 3 days separately. I found that the mean amplitude for the MOG/CFA responses was significantly less than that of the CFA on all the days. P values for the comparison of mean amplitudes between the two groups for days 7, 8 and 9 were 1.98E-07, 1.13E-07 and 1.43E-05 respectively (Fig. 33). Similar to the homemade MOG, the commercial MOG injected mice showed slower kinetics in their responses with significantly higher tau values compared to their controls (CFAs) on all the 3 days. Mean tau values of CFA and MOG/CFA response traces on days 7, 8 and 9 were found to be significantly different with P values 0.00177, 2.68E-04 and 7.27E-05 respectively (Fig. 33).

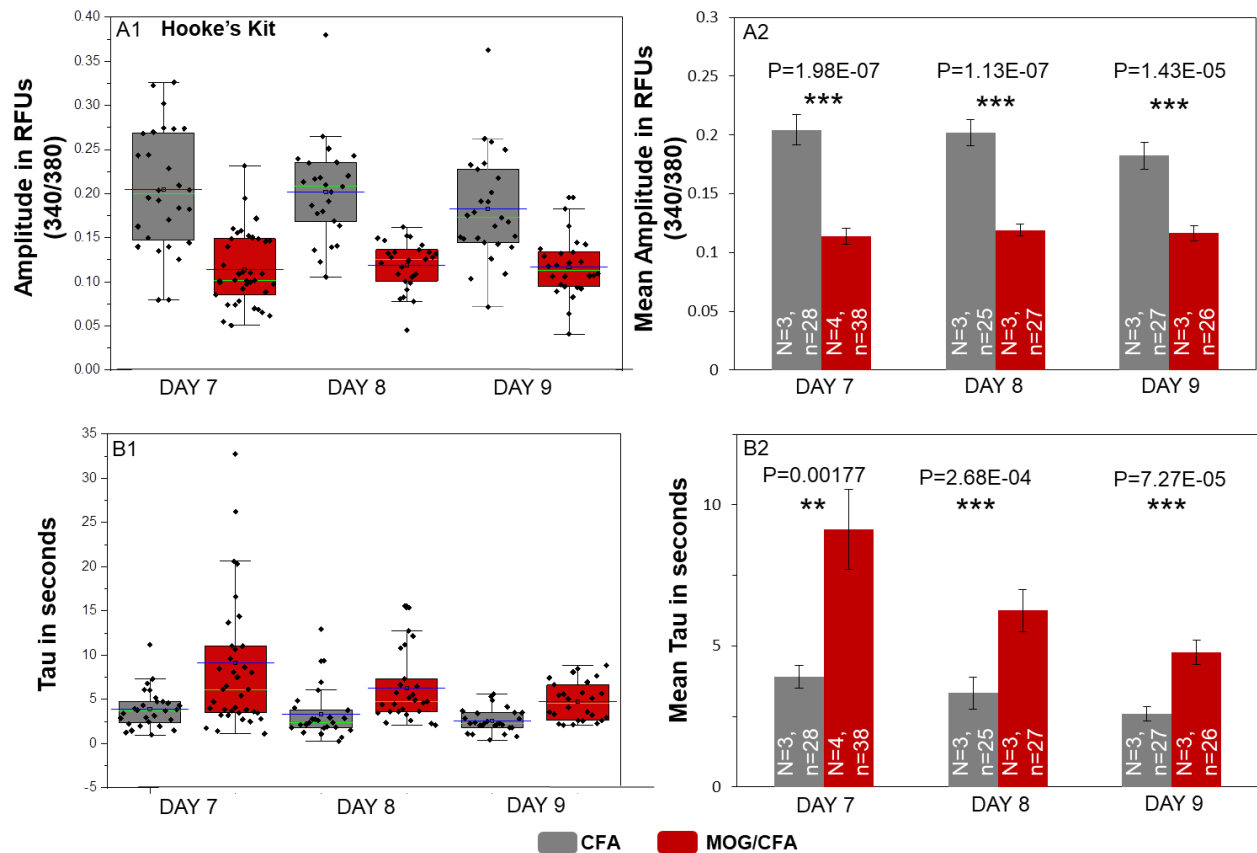


Figure 33: Fura2-AM measurements in commercial CFA and MOG/CFA injected mice retinas on days 7, 8 and 9 after immunization

Individual response amplitudes and time constants for CFA and MOG/CFA injected mice on days 7, 8 and 9 are illustrated through box and whisker plots in A1 and B1. Mean and median values are marked out by the blue and green lines respectively. Mean amplitudes of CFA and MOG/CFA are compared day wise in A2 and mean tau values in B2. Mean

RESULTS

MOG/CFA amplitudes are significantly smaller than average CFA amplitudes while mean time constants (τ) are higher. N =number of mice, n =number of retinal slices; Error bars=SEMs (A2, B2); Whiskers=1.5 times inter-quartile range (A1, B1).

Finally I wanted to confirm that in case of commercial MOG₃₅₋₅₅ peptide injected mice too, calcium influx relative to its corresponding CFA was not varying significantly over the days 7 to 9 after induction. The % values of the MOG/CFA amplitudes and τ values were calculated for each day considering the CFA mean amplitude and mean τ as 100. The MOG/CFA Ca²⁺ influx amplitudes relative to its own mean CFA amplitude were all normally distributed. So, one way ANOVA was tested on them which showed that the normalized MOG/CFA amplitudes were not varying significantly over the 3 days. Similarly, Kruskal-Wallis ANOVA was used to test the τ value populations as they were not normally distributed. The test showed that over the days 7 to 9, normalized MOG/CFA τ values did not vary significantly. The P values for the amplitudes comparison and the time constants comparisons were 0.20076 and 0.91032 respectively (Fig. 34). Since, I saw that the effects of the self-made MOG₃₅₋₅₅ peptide and commercial Hooke's Laboratories one were almost identical I continued the rest of the study with the self-made peptide.

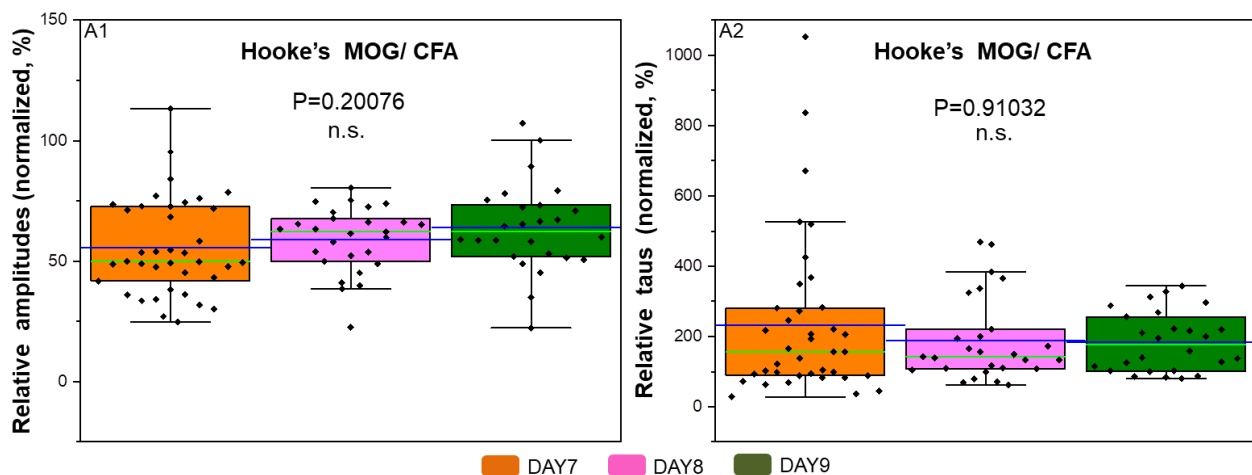


Figure 34: Comparing Ca²⁺ influx amplitudes and kinetics in Hooke's MOG₃₅₋₅₅ injected mice retinal slices over days 7 to 9 after injection

The % normalized values of the MOG/CFA amplitudes with respect to respective mean CFA average amplitudes and the % normalized values of MOG time constants with respect to respective CFA average τ values for the days 7, 8 and 9 are depicted through box and whisker plots in A1 and A2. The mean and median values for the normalized amplitudes and the taus are represented in blue and green lines respectively. Abbreviation: n.s.-not significant; Whiskers=1.5 times inter-quartile range (A1, A2).

3.4 Analyzing RIMs, main regulators of Ca_v channels in EAE photoreceptor terminals

After studying the change in expression pattern of $Ca_v1.4$ channels in the EAE mice retina and also the reduced Ca^{2+} influx, I wanted to delve further and examine whether RIMs were undergoing any alterations in the EAE retina. RIMs are known to be positive regulators of Ca_v channel activity (Kiyonaka et al., 2007; Gandini & Felix, 2011). Besides influencing the biophysical properties of the channel, RIMs are thought to play a role in tethering and stabilizing the Ca_v channels at the active zone below the ribbons. RIMs have been accredited with the role of holding Ca_v channels to the presynaptic membrane on the basis of their interaction with the α -subunit directly or via the β -subunit and RIM-BP (Hibino et al., 2002; Catterall & Few, 2008; Catterall, 2011; Gandini & Felix, 2011; Pangrsic et al., 2018). RIM1,2 knock outs show massively reduced presynaptic Ca^{2+} currents in rod photoreceptors however the Ca_v channel abundance remains unchanged (Grabner et al., 2015). Moreover, RIMs are also proposed to facilitate exocytosis by tethering Rab3-GTP bearing synaptic vesicles to the active zone (Betz et al., 2001; Schoch et al., 2006; Kaeser et al., 2011). In addition to the reduction in Ca^{2+} influx in EAE photoreceptor terminals at an early time point, Dembla et al., 2018 had also found a significant reduction in exocytotic release in EAE mice. These observations strengthened my motivation to look for changes in RIM expression in EAE retinas.

Photoreceptor ribbon synapses have primarily RIM2 α and less of RIM1 α (Grabner et al., 2015), so I used two independent mouse monoclonal RIM2 antibodies (4F7 and 4C6) to analyze their immunofluorescence intensities in the EAE mice retinal sections. Unfortunately, the RIM2 monoclonals did not work ideally on western blots so RIM1,2 rabbit polyclonal antibody was used for the blot analyses.

3.4.1 Coimmunolabeling of EAE retinal synapses with antibodies against RIM2 and PSD95

RIM2 was double immunolabeled with PSD95 on 0.5 μ m thick Epon embedded CFA and MOG/CFA injected mice retinal sections, sacrificed on day9 after the injections. The mouse monoclonal RIM2 antibody (4F7) was detected with Alexa 568 donkey anti-mouse and the polyclonal PSD95 by Alexa 488 chicken anti-rabbit secondary antibody. I observed strong ribbon-like punctate labeling of RIM2 (4F7) at the outer plexiform layer of CFA retinal sections, while it was visibly diminished in the MOG/CFA sections. The labeling of RIM2 (4F7) punctas in the MOG peptide injected sections was too faint to be reliably counted. Hence, measurement and comparison of the number of punctas in a given length of OPL between the two groups of mice was not possible. To ensure that CFA and MOG/CFA retinal layers were comparable in their uniformity and continuity, PSD95 was

RESULTS

used as a control antibody. PSD95 labels rod and cone terminals presynaptically at the outer plexiform layer (Koulen et al., 1998). In the inner plexiform layer PSD95 shows very small punctate labeling, concentrated in postsynaptic processes of bipolar cell ribbon synapses (Koulen et al., 1998). PSD95 labeling in CFA and the MOG/CFA sections showed integrity of both outer and inner synaptic layers (Fig. 35).

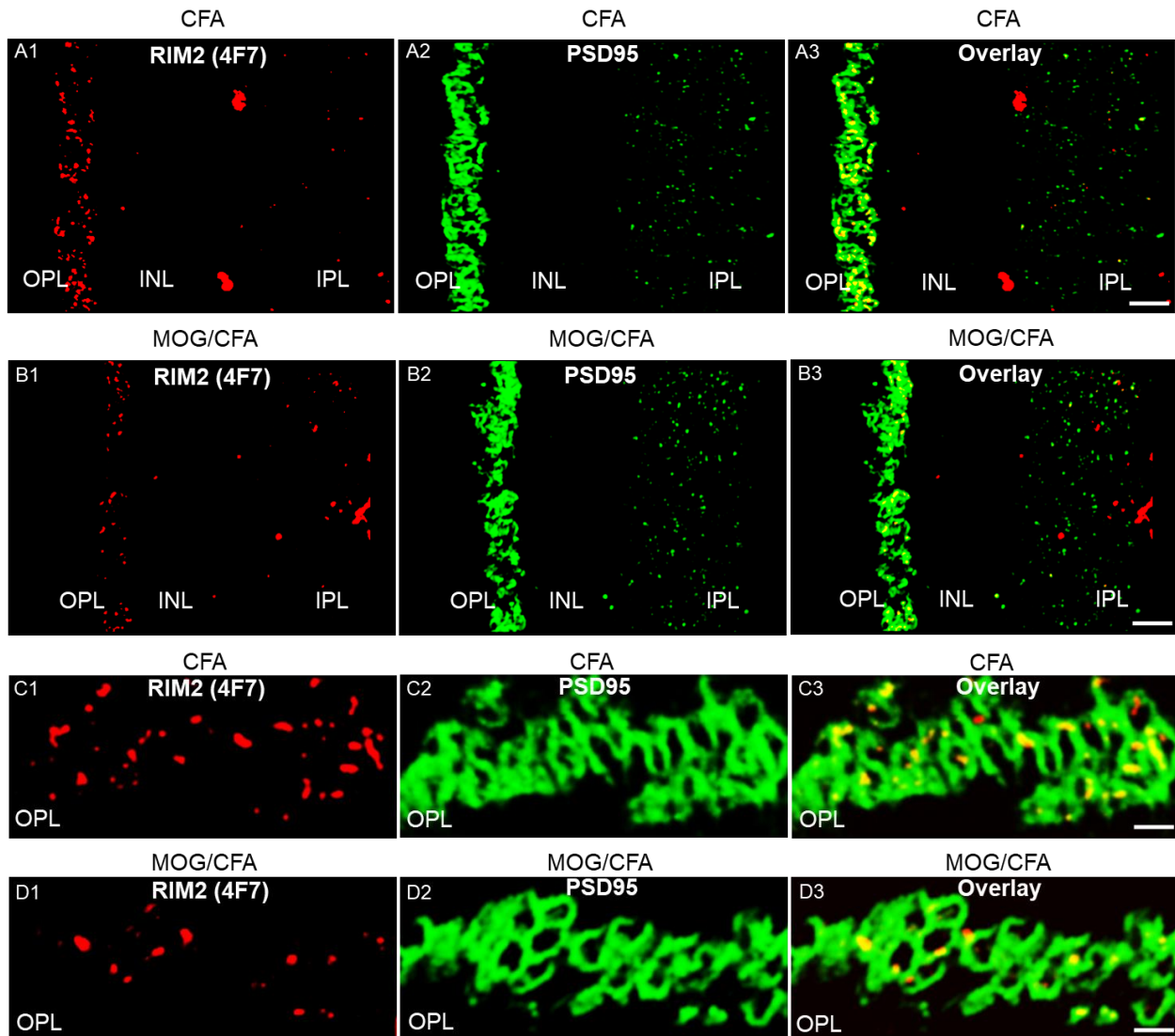


Figure 35: Immunolabeling of RIM2 (4F7) and PSD95 in EAE retinal sections

RIM2 is double immunolabeled with PSD95 on $0.5 \mu\text{m}$ CFA and MOG/CFA injected mice retinal sections. Donkey anti-mouse Alexa 568 and chicken anti-rabbit 488 are used to detect RIM2 and PSD95 respectively (A-D). A1 and B1 show RIM2 (4F7) labeling in CFA and MOG/CFA injected sections at the OPL. PSD 95 labeling at the OPL and IPL of CFA (A2) and MOG/CFA (B2) sections look comparable. A3 and C3 are the merged images of RIM2/PSD95. C-D depicts zoomed views of OPL of CFA and MOG/CFA sections. Abbreviations: OPL-outer plexiform layer, IPL-inner plexiform layer, INL-inner nuclear layer; Scale bars: $5 \mu\text{m}$ (A-B), $2 \mu\text{m}$ (C-D).

RESULTS

Upon quantification of the immunosignals of RIM2-No.1 at the OPL using ImageJ I found more than 50% reduction in mean value of MOG/CFA compared to the CFA mean. The difference in the means was highly significant (P value=4.18E-10). The fluorescence intensity of PSD95 at OPL and IPL was also quantified in the two groups of mice and found to be similar. P value for the mean fluorescence intensity values of PSD95 at the OPL in the two groups was found to be 0.84724 and that at the IPL 0.81928, both being not significant (Fig. 36).

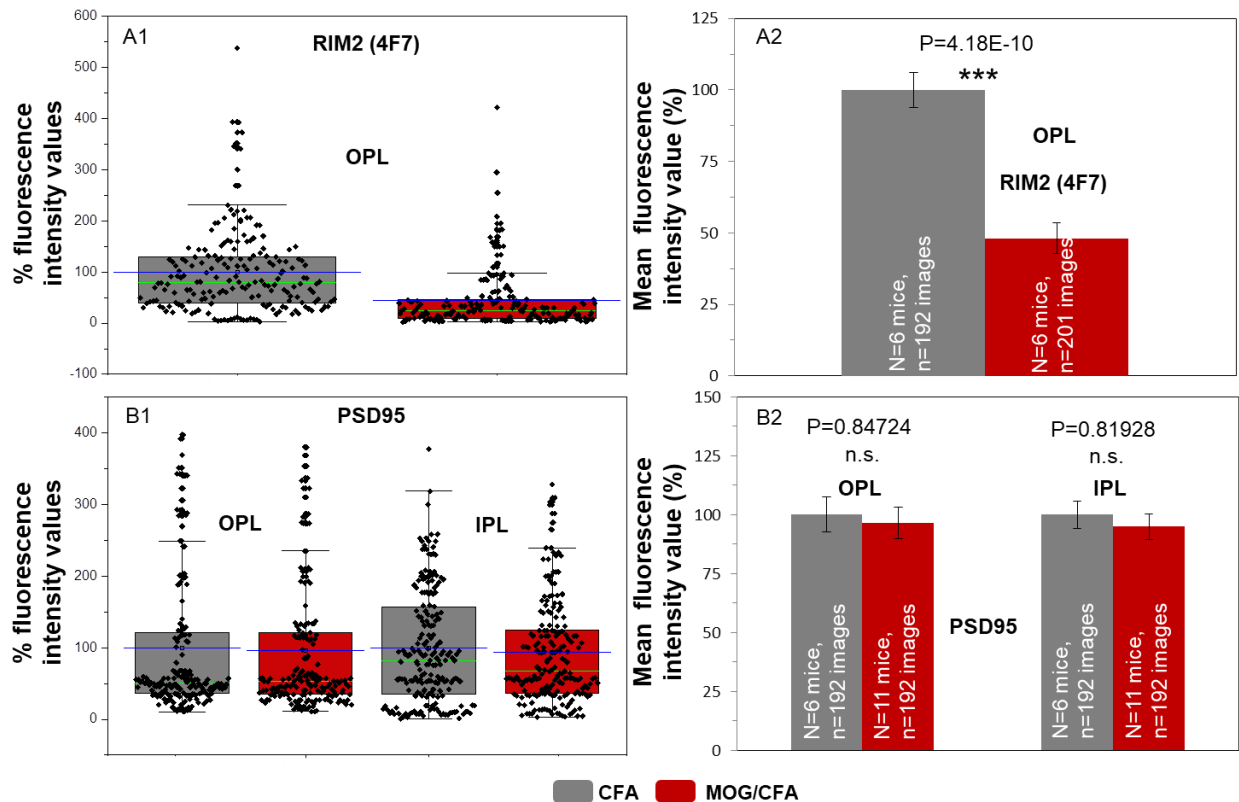


Figure 36: Quantification of RIM2 (4F7) and PSD95 immunosignals in CFA and MOG/CFA mice retinas
A1 illustrates individual % fluorescence values of RIM2 at the OPL in CFA and MOG/CFA injected mice retinal sections in a box plot while B1 depicts the same for PSD95 at the OPL and IPL in the 2 groups of mice. Mean and median values are indicated through blue and green lines in A1 and B1. Comparison of mean fluorescence intensities of RIM2 in A2 show that, the mean value for MOG/CFA is significantly less than that of CFA by >50%. In B2 mean fluorescence values for PSD95 at OPL and IPL are depicted, which do not differ significantly in the two groups. Abbreviations: OPL–outer plexiform layer, IPL–inner plexiform layer, n.s.-not significant; Error bars = SEMs (A2, B2); Whiskers=1.5 times inter-quartile range (A1, B1).

3.4.2 Verifying reduced immunofluorescence of RIM2 (4F7) with a second RIM2 antibody

To verify our RIM data with the RIM2 (4F7) antibody, we repeated the immunolabeling with a second independent anti-RIM2 mouse monoclonal antibody (4C6). RIM2 (4C6) was double immunolabeled with a rabbit polyclonal antibody against RIBEYE-B domain (U2656) on 0.5 μ m thick mice retinal sections. Donkey anti-mouse Alexa 568 was used as the secondary antibody for

RESULTS

RIM2 (4C6) while RIBEYE was detected using goat anti-rabbit Alexa 647 (Fig. 37). RIM2 (4C6) labeling at the OPL colocalizing with the ribbon was quantified and compared between the CFA and the MOG/CFA mice retinal sections. $\approx 50\%$ of reduction in fluorescence of RIM2 (4C6) was observed in the peptide injected mice compared against the CFA ones. The mean fluorescence intensities differed by a P value of $9.6E-07$. I counted the number of punctas of RIM2 (4C6) in the two groups. In $100 \mu\text{m}$ of OPL the mean count for the number of RIM2 punctas in MOG/CFA sections was not significantly different from that of the CFA sections (P value= 0.11629) (Fig. 37). Next I wanted to analyze RIM2 punctas at a higher resolution using SR-SIM to corroborate my RIM data so far, however unfortunately the extremely reduced fluorescence of RIM2 in MOG/CFA sections made it impossible to do so.

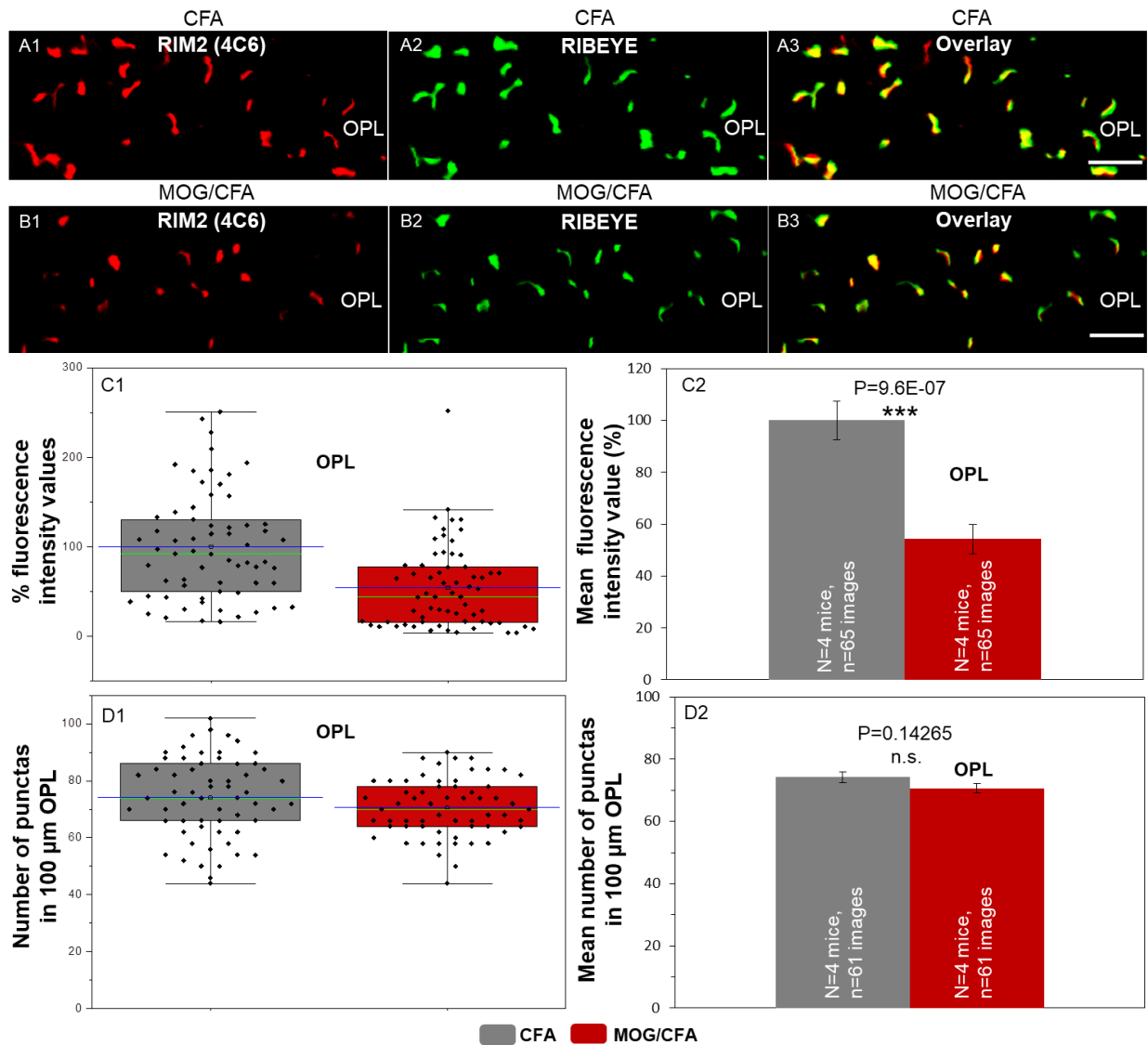


Figure 37: RIM2 (4C6) immunolabeling and quantification in CFA and MOG/CFA mice retinal sections
A and B show indirect immunofluorescent labeling of RIM2 (4C6)/ donkey anti-mouse Alexa 568 (A1, B1), anti-RIBEYE/goat

RESULTS

anti rabbit Alexa 647(A2, B2) and its merged images (A3, B3) in 0.5 μm thick Epon embedded retinal sections of CFA and MOG/CFA mice respectively. C1 depicts the box and whisker plots for the % fluorescence intensity values of RIM2 (4C6) at the OPL for both the groups. The counts for the number of punctas of RIM2 (4C6) in 100 μm length of the OPL in both the CFA and MOG/CFA images are shown in D1. Blue and the green lines in C1 and D1 represent the mean and median values respectively. Mean fluorescence intensity values and the mean count for the number of punctas in 100 μm of OPL are illustrated in C2 and D2 respectively. Abbreviations: OPL - outer plexiform layer, n.s.-not significant; Scale bar: 2 μm (A-B); Error bars=SEMs (C2, D2); Whiskers=1.5 times inter-quartile range (C1, D1).

3.4.3 Western blot analysis of RIMs in EAE mice retinal lysates

To quantify the overall expression of RIMs in the EAE mice retina I performed Western blot analyses for CFA and MOG/CFA mice retinal lysates. A third antibody RIM1,2 rabbit polyclonal was used for this purpose since the monoclonal antibodies did not work reliably on retinal blots. The upper half of $\text{Ca}_v\beta 2$ blots (118 kDa to > 212 kDa) was incubated with the RIM1,2 antibody. On the CFA and MOG/CFA retinal blots RIM1,2 gave two bands, RIM 1 at ~212 kDa mark and RIM 2 at ~180 kDa mark (Grabner et al., 2015). Fodrin (~ 230 kDa) Grabner et al., 2015 was used as the loading control for the retinal lysates (Fig. 38). To determine whether the band intensities of RIM1, RIM2 and fodrin in the two groups were showing any correlation ship, Pearson's correlation coefficient (r) was computed on the normally distributed data in MS-Excel. While RIM2 and fodrin showed strong correlation with $r > 0.8$, (0.929108 and 0.830694 respectively), RIM1 showed a relatively weaker correlation with $r = 0.715278$ (i.e. with $r < 0.8$). Hence, in accordance with the suggestions from De Winter, 2013 unpaired t-test was conducted for RIM1 and paired t-tests for RIM2 and fodrin. The P values for RIMs 1 and 2 and fodrin were 0.037016, 0.007068 and 0.779549 respectively. Normalization of the RIM band intensities with that of fodrin (loading control) exhibited fairly reduced RIM 1 and 2 band intensities for MOG/CFA compared against CFA. The mean normalized RIM1 of MOG/CFA being 25% less than that of CFA and the mean normalized RIM2 by ~35% (Fig. 38). Normalized RIM1 and 2 also had high Pearson correlation coefficients of 0.855594 and 0.948094 respectively. Paired t-tests on normalized RIM1 and RIM2 band intensities in the two groups showed that the mean intensity values of MOG/CFA were significantly less than that of CFA (P values=0.001479 and 0.005305 for RIM1 and 2 respectively) (Fig. 38). Thus unlike $\text{Ca}_v1.4$ alphas, RIMs were undergoing high significant reductions in their total expression levels in EAE retina as early as day9 after MOG peptide injection.

RESULTS

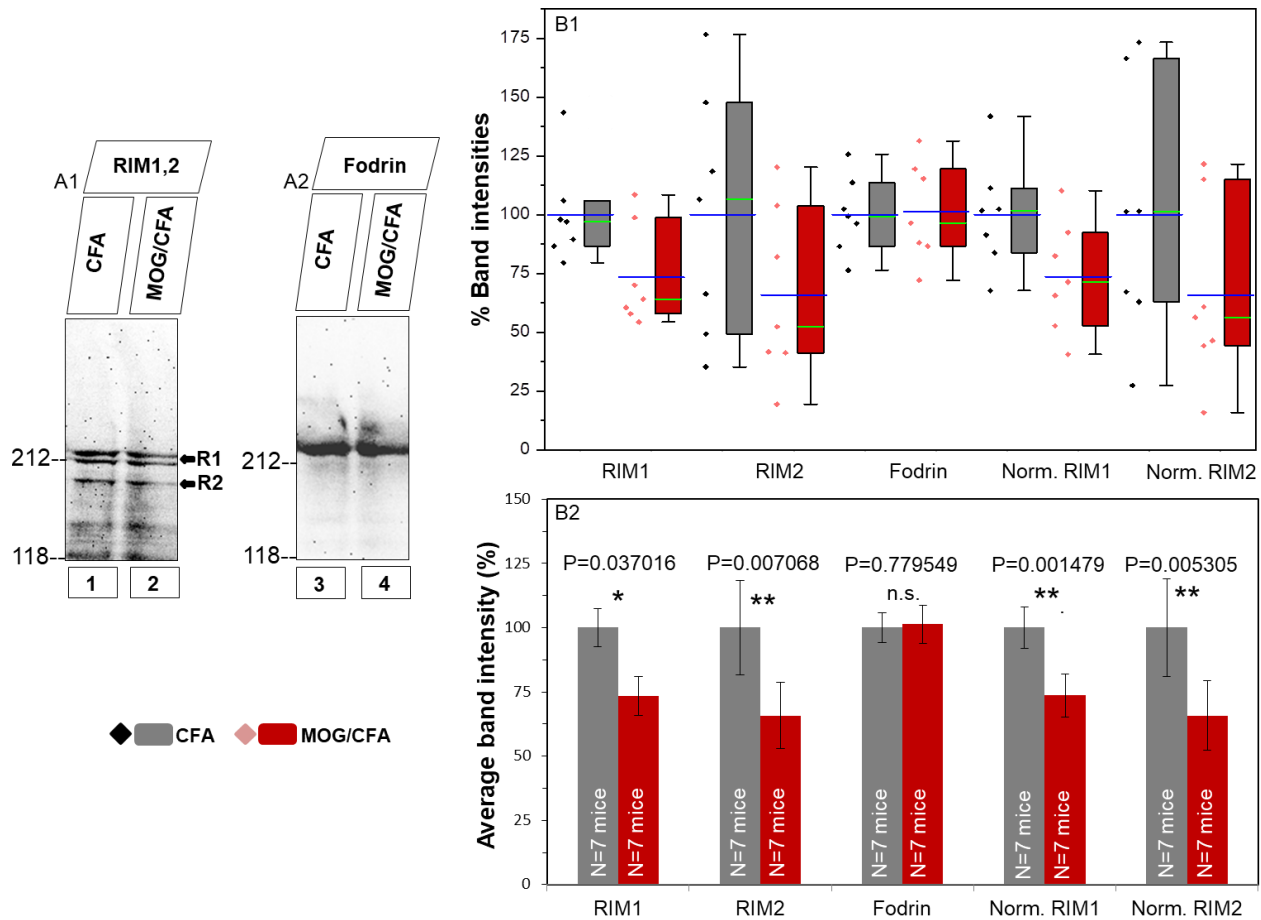


Figure 38: Western blot analyses of RIM1,2 on EAE mice retinal lysates

A1 and A2 are blots of RIM1,2 and fodrin on CFA and MOG/CFA injected mice retinal lysates separated by SDS-PAGE using a discontinuous running gel (7% on 10% acrylamide). RIM1 bands at ~212 kDa (R1) and RIM2 bands at ~180 kDa (R2) are visible in A1 (lanes 1 and 2 for CFA and MOG/CFA respectively) and A2 shows the blot lanes of the very same strip with loading control fodrin at ~230 kDa in lanes 3 and 4. The individual % band intensities of RIM1, RIM2, fodrin and RIM 1 & 2 normalized by fodrin in the two groups are illustrated through a box plot in B1. Mean and the median values for the band intensities are shown in blue and green lines respectively. Besides normalized RIMs 1 and 2, absolute band intensities of RIM1, 2 and fodrin have also been compared in B2. Abbreviation: n.s.-not significant; Error bars = SEMs (B2); Whiskers=1.5 times inter-quartile range (B1).

3.5 Comparing intracellular calcium concentration in retinal slices of EAE and control mice

Besides using Fura2-AM in depolarization experiments to determine extent of calcium influx in CFA (control) and MOG/CFA mice retinal slices, Fura2-AM could also be used to compare intracellular calcium concentration in them. Since dye loading conditions of the retinal slices in both the groups are identical, the baseline ratiometric fluorescence (340/380) of Fura2 in resting solution (2mM Ca^{2+}) could be considered as an indirect measure for intracellular calcium concentration. I observed

RESULTS

that MOG/CFA (self-made and Hooke's both) injected mice retinal slices show significantly higher mean baseline values for ratiometric (340/380) fluorescence compared to CFAs at the OPL on all the 3 days—7, 8 and 9 after induction (Fig. 39). Self-made MOG peptide injected mice retinas exhibit significantly higher baseline ratiometric fluorescence of FURA2 against the CFAs on all the 3 days (P values = 6.78E-04, 5.23E-05 and 1.03E-04 on days 7, 8 and 9 respectively) (Fig. 39).

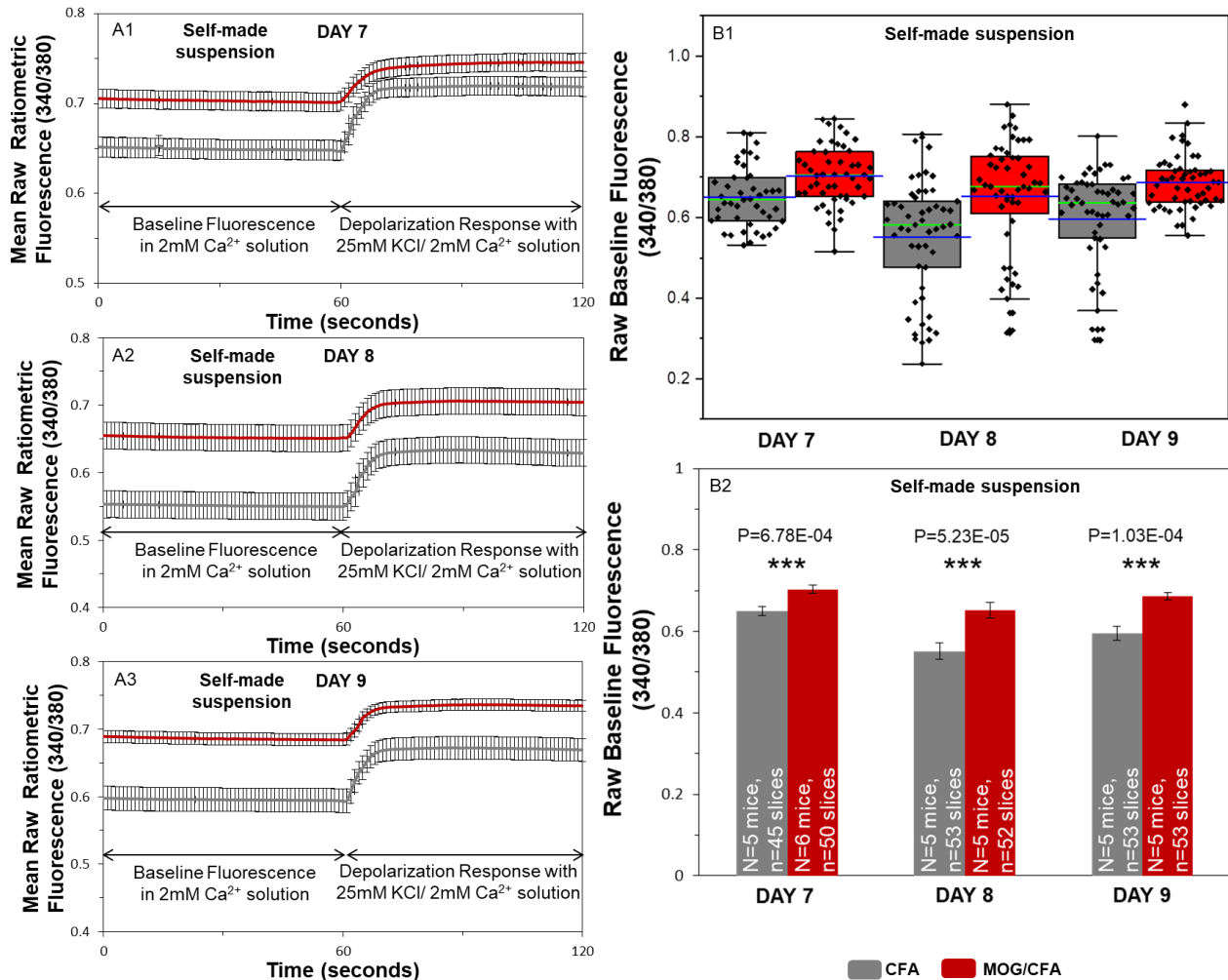


Figure 39: Baseline ratiometric (340/380) FURA2 fluorescence comparison between self-made MOG/CFA and CFA-injected mice retinal slices

A1, A2 and A3 depict plots of mean raw FURA2-AM ratiometric (340/380) fluorescence against time for CFA and MOG/CFA mice retinal slices on days 7, 8 and 9 respectively. B1 and B2 represent the distribution of baseline ratiometric fluorescence intensities (340/380) of FURA2 in self-made MOG/ CFA and CFA retinal slices over the days 7, 8 and 9 after induction. Blue and green lines indicate the mean and median values. The mean baseline Fura2 (340/380) fluorescence values of control and EAE retinal slices are compared in A2. Error bars = SEMs (A1, A2, A3, B2); Whiskers=1.5 times inter-quartile range (B1).

Hooke's MOG injected mice retinal slices also show significantly higher baseline (340/380) FURA2-AM fluorescence against its corresponding CFA counterpart (P values=1.65E-04, 7.15E-05 and

RESULTS

5.33E-04 for days 7, 8 and 9 accordingly) (Fig. 40). This data along with my previous results on reduced calcium influx in MOG/CFA photoreceptor terminals suggest that there must be some disturbance in the efflux machinery of calcium in EAE photoreceptor terminals, which could possibly explain the intracellular calcium dyshomeostasis.

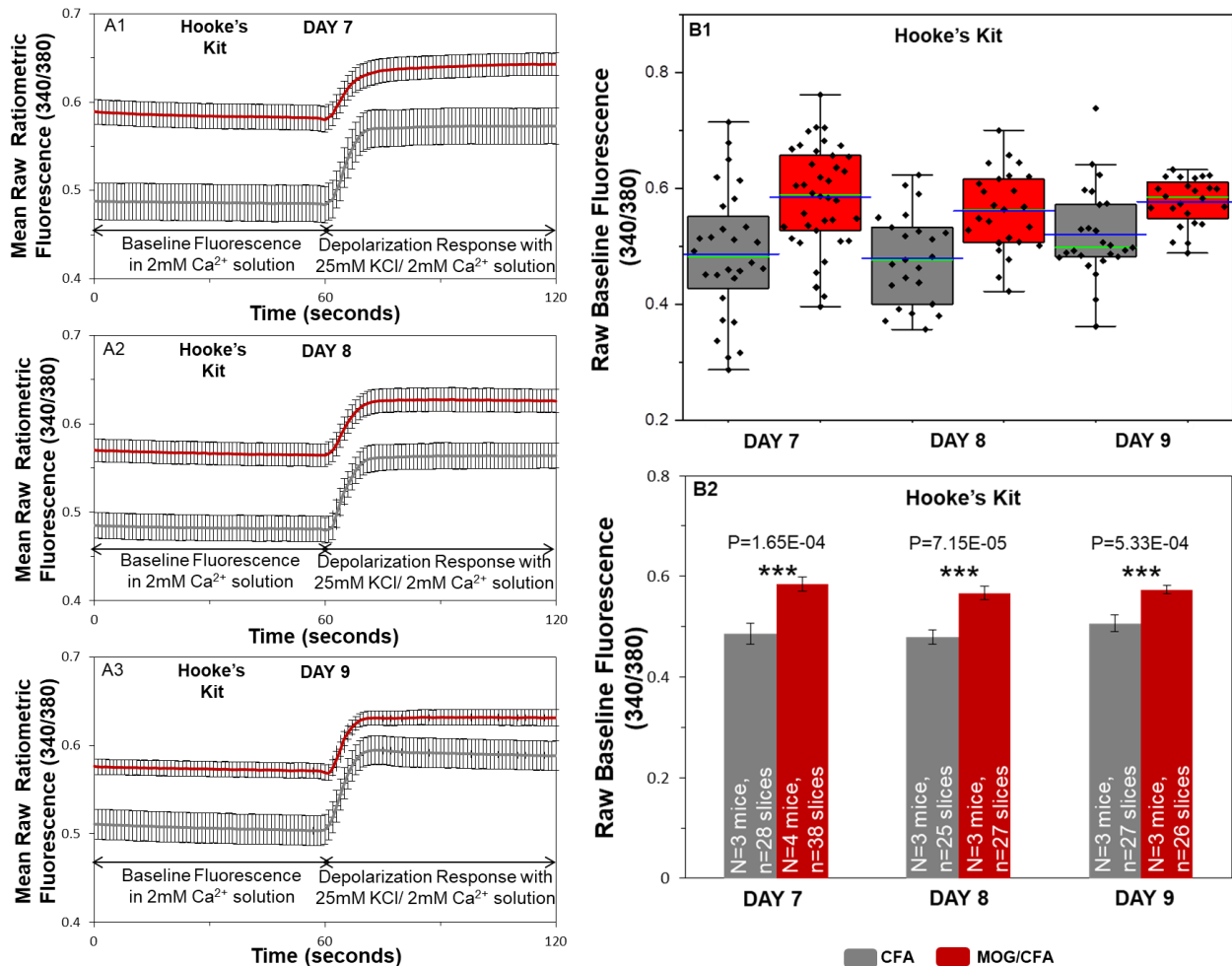


Figure 40: Comparing baseline ratiometric (340/380) fluorescence of FURA2 in retinal slices of mice induced with Hooke's laboratories EAE induction kit

A1, A2 and A3 illustrate the mean traces of raw ratiometric (340/380) FURA2-AM fluorescence values against time for Hooke Laboratory's CFA and MOG/CFA mice retinal slices on days 7, 8 and 9 after disease induction respectively. B1 demonstrates the box and plot distribution for baseline ratiometric fluorescence intensities (340/380) of FURA2 in CFA and MOG/CFA injected mice retinal slices over days 7, 8 and 9. Mean and median values are represented by blue and green lines respectively. Mean baseline ratiometric fluorescences (340/380) of CFA and MOG/CFA for all the 3 days are compared in B2. Error bars= SEMs (A1, A2, A3, B2); Whiskers=1.5 times inter-quartile range (B1).

3.6 Pre-clinical effect of EAE on calcium efflux mechanism in mice photoreceptor synapses

Though the Ca^{2+} influx machinery was adversely affected in EAE photoreceptor terminals, there was strong evidence of higher intracellular calcium in them in comparison to CFA. This made me curious about functioning of the Ca^{2+} efflux machinery in EAE photoreceptor terminals. Of the two main modes of calcium efflux in the photoreceptor synapses, PMCA's being more abundant and more efficient in calcium extrusion compared to the NCXs (Zenisek & Matthews, 2000; Duncan et al., 2006; Herchuelz et al., 2007) formed the basis of my preliminary study. The two most abundant isoforms of PMCA's in the retina are 1 and 2 (Duncan et al., 2006). I double immunolabeled PMCA1 and PMCA2 separately with PSD95 on 1.5 μ m thick retinal sections of CFA and MOG/CFA injected mice sacrificed on day 9 after injection. All the 3 antibodies were rabbit polyclonal in nature. Blocking using Fab fragments was performed for using secondary antibodies of the same antigenic species. As PSD95 demarcated out the presynaptic terminal labeling at the OPL we could see strong presynaptic and extra-synaptic labeling (on the side of the INL) of PMCA 1 and 2 at the OPL. They also labeled the IPL (Figs. 41 & 42).

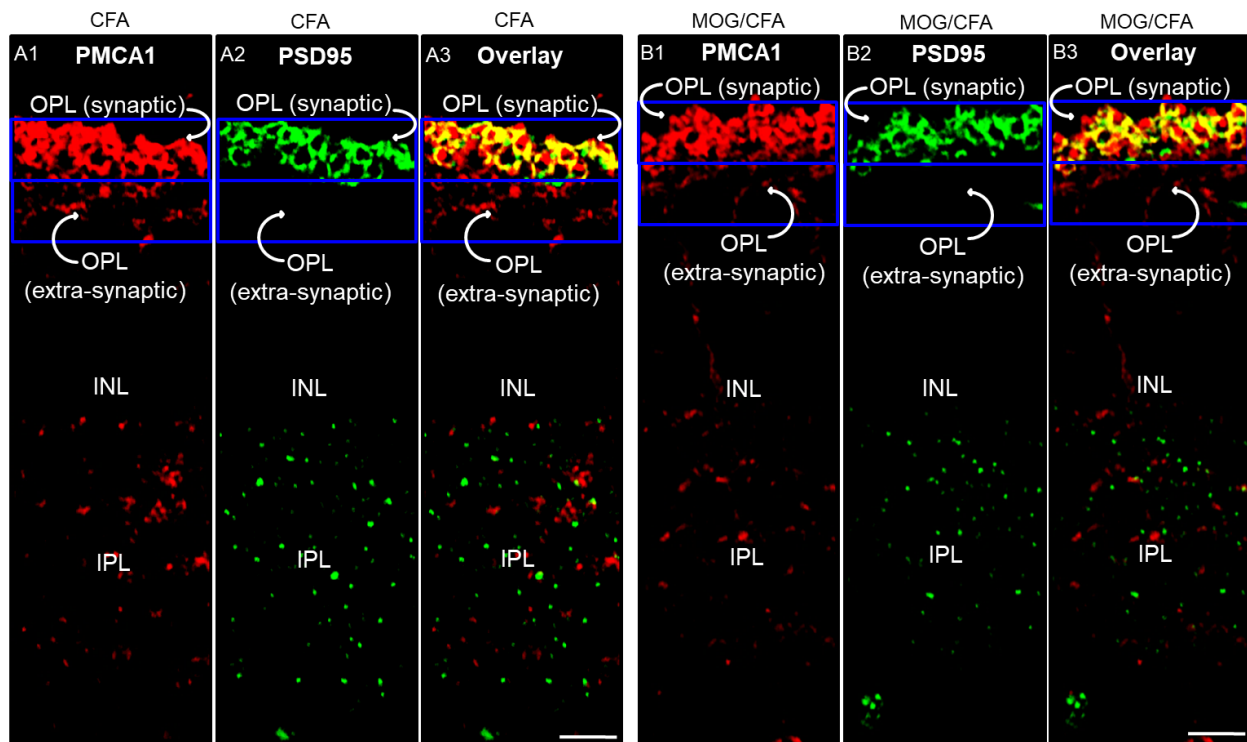


Figure 41: PMCA1/PSD95 double immunolabeling in CFA and MOG/CFA injected mice retinal sections
Panels A and B show indirect immunofluorescent labeling of PMCA1/donkey anti-rabbit Alexa 568 (A1, B1), PSD95/chicken anti-rabbit Alexa 488 (A2, B2) and its merged images (A3, B3) on 1.5 μ m thick Epon embedded retinal sections of both the groups. PSD95 labeling clearly marks presynaptic terminals at the OPL. PMCA1 shows strong synaptic and extra-synaptic

RESULTS

labeling at the OPL and fainter labeling at the IPL. The labeling of both PMCA1 and PSD95 in CFA (A1, B1) and MOG/CFA (A2, B2) retinal sections look comparable. Abbreviations: OPL-outer plexiform layer, INL-inner nuclear layer, IPL-inner plexiform layer; Scale bar = 5 μ m (A, B).

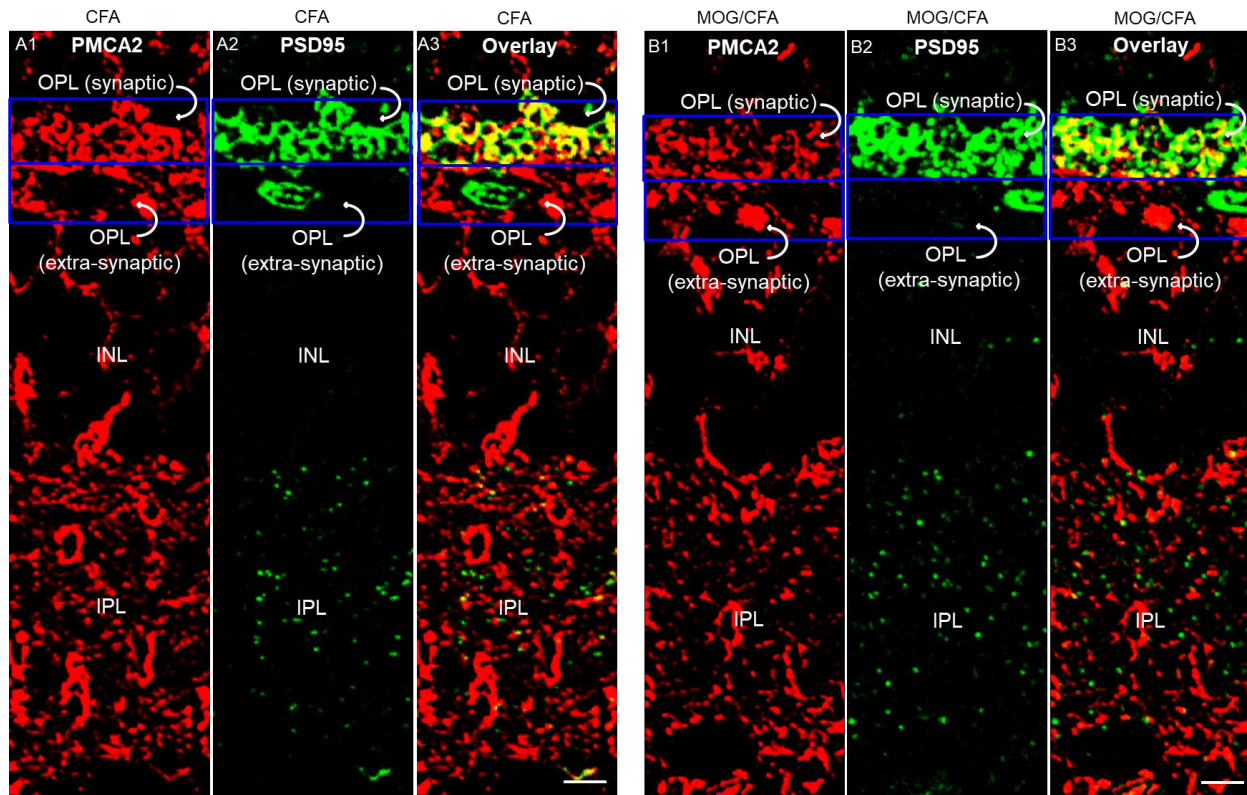


Figure 42: PMCA2/PSD95 coimmunolabeled on CFA and MOG/CFA injected mice retinal sections

A1 and B1 illustrate indirect immunofluorescent labeling of PMCA2/donkey anti-rabbit Alexa 568 on 1.5 μ m thick Epon embedded retinal sections of both the groups. While A2 & B2 show PSD95/chicken anti-rabbit Alexa 488 labeling of the very same sections and A3 & B3 are the merged images. PSD95 helps in demarcation of the synaptic and extra-synaptic labeling of PMCA2 by labeling the presynaptic photoreceptor terminals. PMCA2 shows strong synaptic and extra-synaptic labeling at the OPL and at the IPL. . Abbreviations: OPL-outer plexiform layer, INL-inner nuclear layer, IPL-inner plexiform layer; Scale bar = 5 μ m (A, B)

I next quantified fluorescence intensities of both the antibodies, PMCA1 and PMCA2, in the retinal sections of CFA and MOG/CFA injected mice. 3 separate ROIs were used to mark out the different retinal areas at which the fluorescence was measured separately. On the basis of the PSD95 labeling we marked out the ROIs for the synaptic region of the OPL and also the extra-synaptic part. The third ROI was for the IPL (Fig.s 41 & 42).

On analysis I found that average fluorescence intensities of PMCA1 at the synaptic and extra-synaptic portions of OPL and IPL in the 2 groups of mice were not significantly different from each other. The P values at the OPL (synaptic), OPL (extra-synaptic) and IPL are as follows: 0.86137,

RESULTS

0.54054 and 0.95742. Thus PMCA1 is not getting altered in EAE mice retina at a preclinical stage (Fig. 43).

Next, I proceeded to analyze PMCA2 expression in a similar fashion through immunofluorescence assay. In this case, however I observed that there were significant differences in the fluorescence intensities of PMCA2 in the control (CFA) and EAE (MOG/CFA) mice retinal sections. Synaptic part of the OPL showed a significant reduction of > 30% in the EAE retina with a P value=1.70E-04. Average fluorescence at extra-synaptic part of the OPL in EAE retina was also less than that in the control retina by ~25% with a P value=0.00166. The IPL too showed a significant reduction in its fluorescence intensity in case of EAE (P value = 0.0149) (Fig. 43).

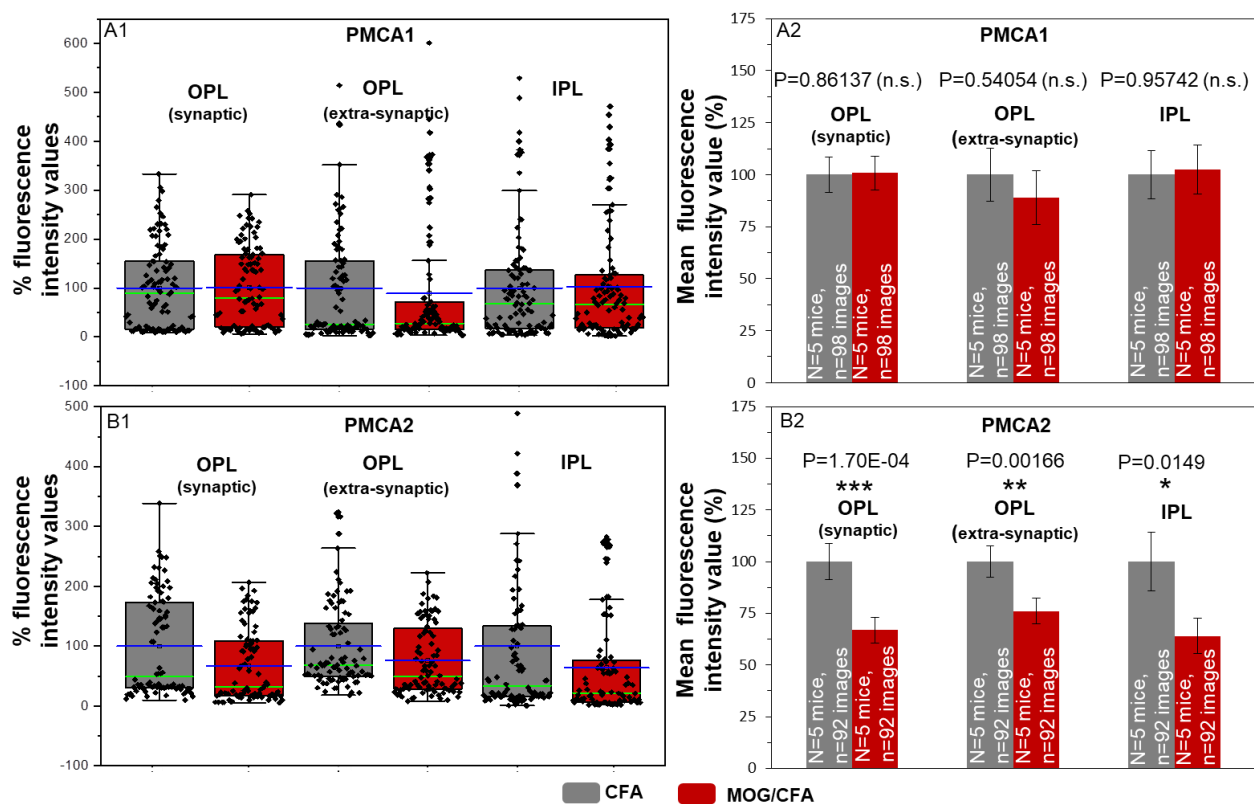


Figure 43: Quantification of PMCA1 and PMCA2 immunosignals in CFA and MOG/CFA retinal sections

A1 and B1 illustrate the individual % fluorescence intensity values of PMCA1 and PMCA2 at the synaptic OPL, extra-synaptic part of OPL and at the IPL in CFA and MOG/CFA mice retinal sections in a box plot. The mean and median values are indicated by the blue and green lines in A1 and B1. A2 shows that mean PMCA1 fluorescence intensities at all the three different regions remain similar in CFA and MOG sections. B2 depicts % reductions observed in mean fluorescence intensities of PMCA2 at the OPL (synaptic and extra-synaptic) and the IPL in case of EAE compared to the control mice retina. OPL (synaptic) shows a reduction in fluorescence by more than 30%, OPL (extrasynaptic) by ~25% and IPL by ~40% though with far greater variability. Abbreviations: OPL – outer plexiform layer, IPL – inner plexiform layer, n.s.-not significant; Error bars = SEMs (A2, B2); Whiskers=1.5 times inter-quartile range (A1, B1).

3.7 Testing of specificity of antibodies

Most of the data of my PhD thesis was generated by the use of lab-made antibodies. Therefore, to ensure the specificity of these antibodies I did a series of experiments. The antibodies were either tested on respective knock out sections or blocked by preabsorbing with respective peptides or checked for their specificity by overexpressing respective proteins in cell line.

3.7.1 $Ca_v1.4$ alpha antibodies

Both of the $Ca_v1.4$ alpha antibodies N-term and C-term were tested on $Ca_v1.4$ alpha knockout mice retinal sections. The sections were coimmunolabeled with the mouse monoclonal anti-RIBEYE antibody (2D9). The wild type sections showed $Ca_v1.4$ alpha labeling coinciding with RIBEYE labeling at the OPL. Both of the $Ca_v1.4$ antibodies had no labeling in the KO sections thus proving their specificity (Figs 44 and 45). $Ca_v1.4$ alpha KO sections showed a disturbed OPL with dot like floating ribbons and a normal looking IPL (Zabouri & Haverkamp, 2013).

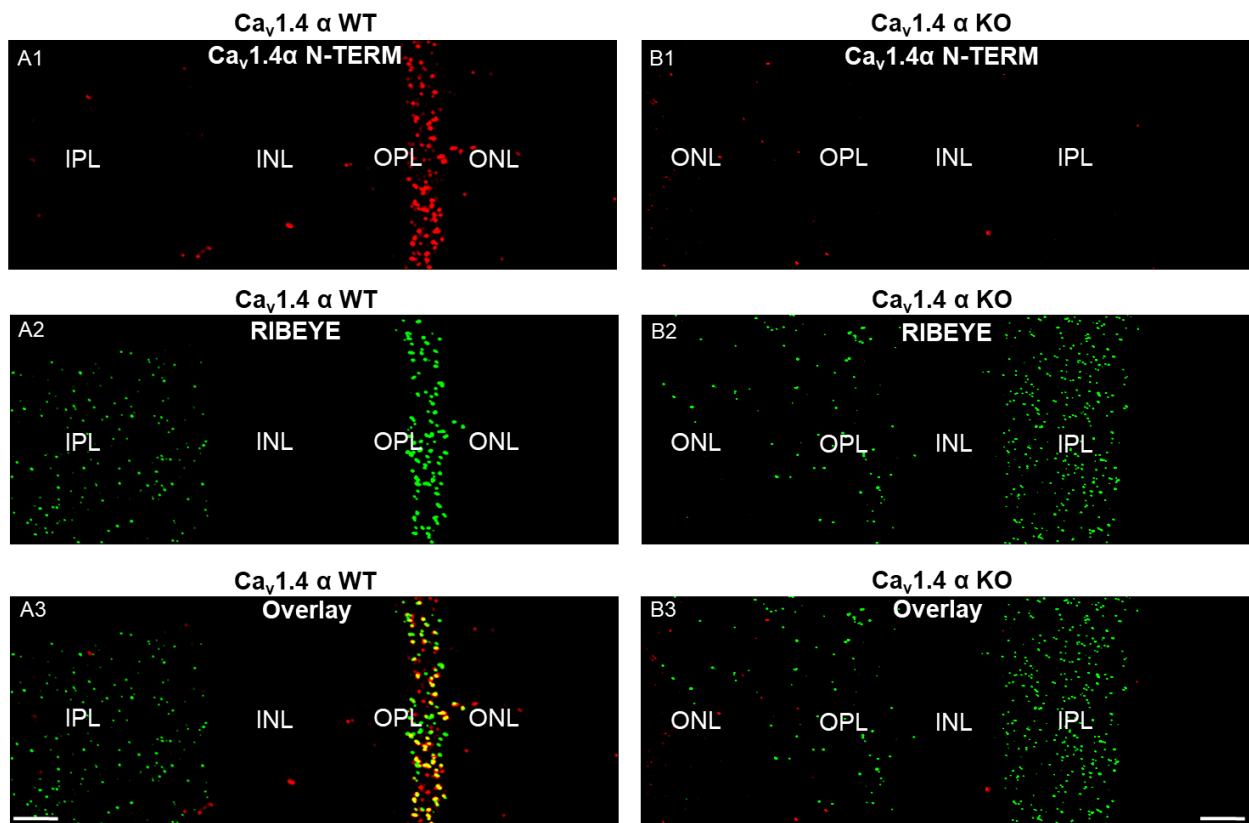


Figure 44: $Ca_v1.4$ alpha N-term is coimmunolabeled with monoclonal anti-RIBEYE antibody on WT and $Ca_v1.4$ KO mice retinal sections

A1 shows the $Ca_v1.4$ alpha N-term labeling with donkey anti-rabbit Alexa 568 at the OPL in Epon embedded wild type mice retinal sections and B1 illustrates the absence of $Ca_v1.4$ alpha N-term labeling in $Ca_v1.4$ KO sections. A2 and B2 show RIBEYE immunosignals at the OPL and IPL with chicken anti-mouse Alexa 488 in WT and KO sections. A3 and B3 represent merged

RESULTS

images of WT and KO sections. Abbreviations: ONL-outer nuclear layer, OPL-outer plexiform layer, INL-inner nuclear layer, IPL-inner plexiform layer, WT-wild type, KO-knock out; Scale bar = 5 μ m (A, B). Data generated by Dr. Ekta Mayur Dembla.

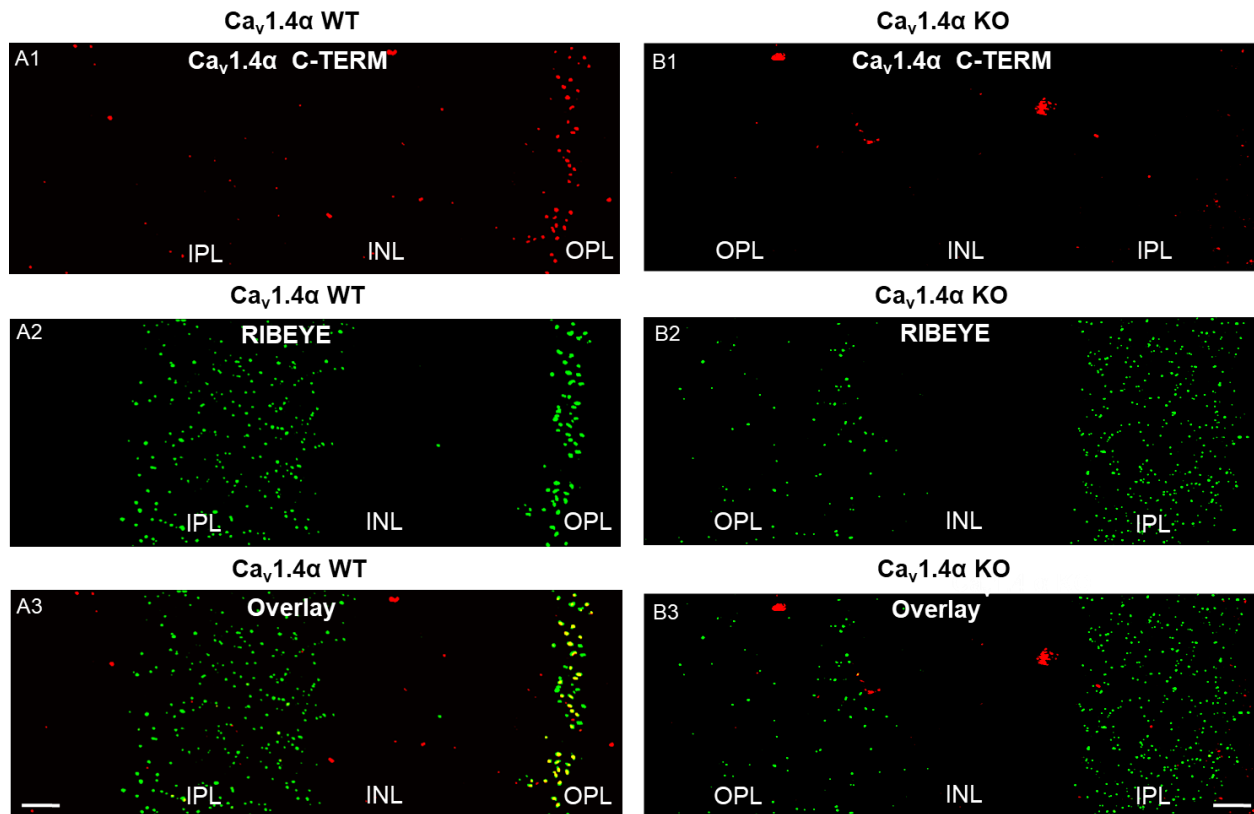


Figure 45: Double immunolabeling of $Ca_v1.4\alpha$ C-term with monoclonal RIBEYE antibody on WT and $Ca_v1.4$ KO mice retinal sections

$Ca_v1.4$ alpha C-term/donkey anti-rabbit Alexa 568 labeling at the OPL of Epon embedded wild type mice retinal section is shown in A1 and B1 shows the absence of $Ca_v1.4$ alpha C-term labeling in $Ca_v1.4$ KO section. A2 and B2 show RIBEYE/chicken anti-mouse Alexa 488 labeling at the OPL and IPL in WT and KO sections respectively. A3 and B3 represent the merged images. Abbreviations: ONL-outer nuclear layer, OPL-outer plexiform layer, INL-inner nuclear layer, IPL-inner plexiform layer, WT-wild type, KO-knock out; Scale bar = 5 μ m (A, B). Data generated by Dr. Ekta Mayur Dembla.

3.7.2 $Ca_v\beta2$ antibodies

To rule out the issue of cross reactivity, both of the $Ca_v\beta2$ rabbit polyclonal antibodies $Ca_v\beta2$ (No.1) and $Ca_v\beta2$ (No.2) were coimmunolabeled with SV2 on Epon embedded $Ca_v\beta2$ KO and WT retinal sections. $Ca_v\beta2$ antibodies gave punctate labelings at the OPL in WT sections while their labeling was absent in $Ca_v\beta2$ KO. $Ca_v\beta2$ KO retina had a thinned out OPL and some sprouting of the SV2 labeling was also evident. The IPL however looked normal (Katiyar et al., 2015) (Fig.s 46 & 47).

RESULTS

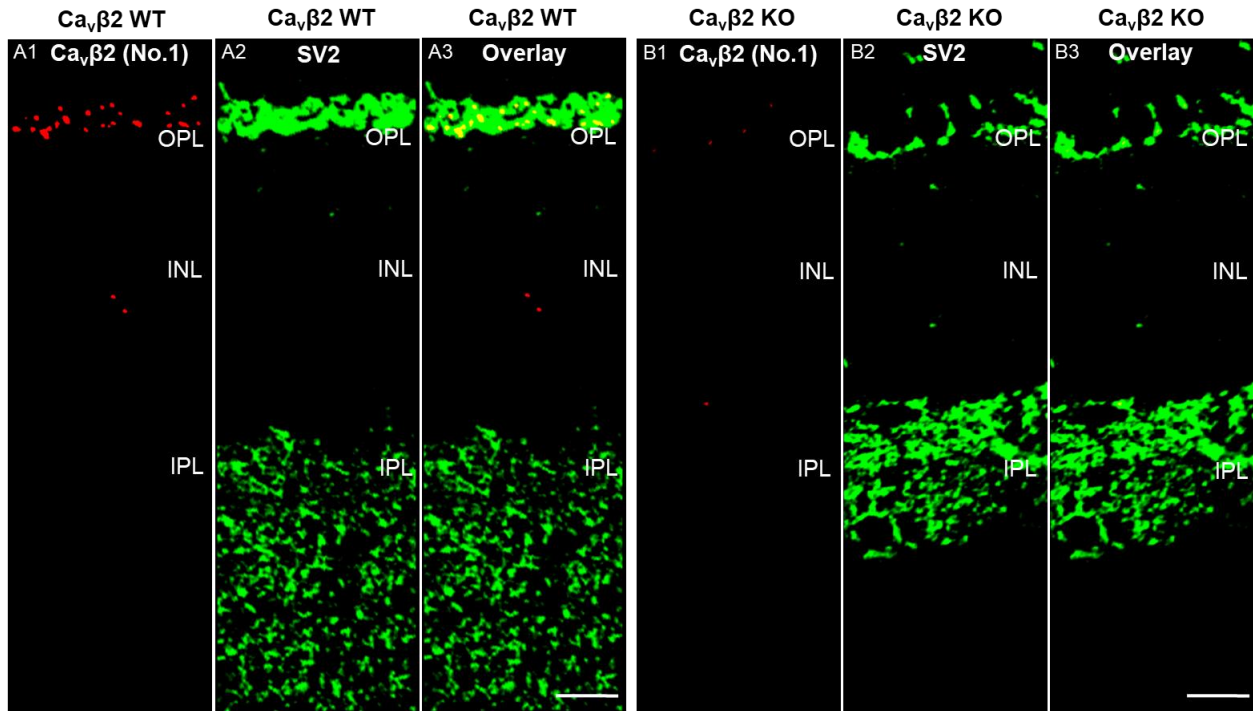


Figure 46: Double immunolabeling of $Ca_v\beta 2$ (No.1) and SV2 on WT and $Ca_v\beta 2$ KO mice retinal sections
 $Ca_v\beta 2$ (No.1)/donkey anti-rabbit Alexa 568 and SV2/chicken anti-mouse Alexa 488 are labeled on Epon embedded $0.5 \mu\text{m}$ WT (A) and $Ca_v\beta 2$ KO (B) sections. Single punctate labeling of $Ca_v\beta 2$ (No.1) at the OPL is seen in the WT section (A1) while in the KO section its labeling is absent proving its specificity (B1). SV2 labels the OPL and IPL in the WT (A2) and KO sections (B2.). SV2 labeling at the OPL in the KO retina is disrupted, thin and sprouting, though the IPL looks normal. A3 and B3 are the merged images of SV2 and $Ca_v\beta 2$ in WT and KO sections respectively. Abbreviations: OPL-outer plexiform layer, INL-inner nuclear layer, IPL-inner plexiform layer, WT-wild type, KO-knock out; Scale bar = $5 \mu\text{m}$ (A, B).

RESULTS

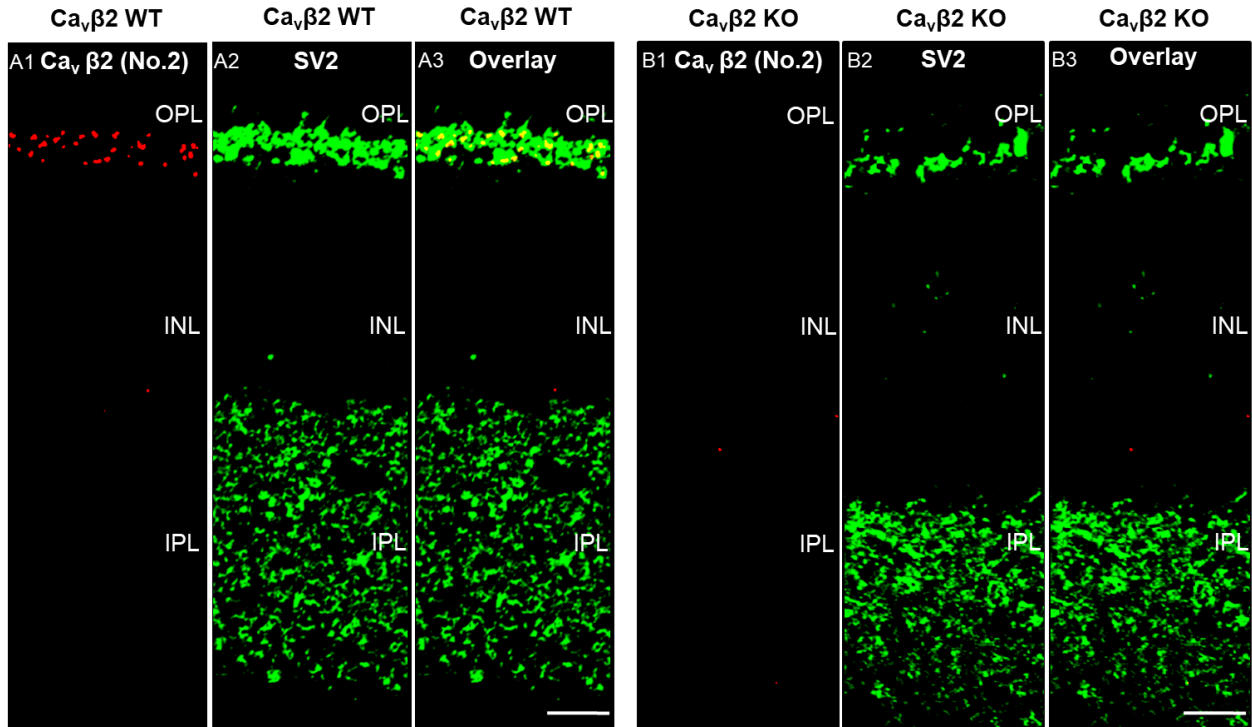


Figure 47: Immunolabeling of $Ca_v\beta 2$ (No.2) and SV2 on WT and $Ca_v\beta 2$ KO mice retinal sections

$Ca_v\beta 2$ (No.2)/donkey anti-rabbit Alexa 568 and SV2/chicken anti-mouse Alexa 488 are labeled on Epon embedded $0.5 \mu\text{m}$ WT (A) and $Ca_v\beta 2$ KO (B) sections. $Ca_v\beta 2$ (No.2) shows punctate labeling at the OPL in WT section (A1) and its immunosignals are absent in the KO section (B1). SV2 labels the OPL and IPL in the WT section (A2); in the KO section (B2) SV2 labeling at the IPL looks normal, however the OPL is disrupted and thin. A3 and B3 show the merged images of SV2 and $Ca_v\beta 2$ in WT and KO sections respectively. Abbreviations: OPL-outer plexiform layer, INL-inner nuclear layer, IPL-inner plexiform layer, WT-wild type, KO-knock out; Scale bar = $5 \mu\text{m}$ (A, B).

3.7.3 RIM2 mouse monoclonal antibodies

Both of the RIM2 monoclonal antibodies, RIM2 (4F7) and RIM2 (4C6) were examined for their specificity through preabsorption experiments using respective blocking peptide and control unrelated peptide. The antibodies were preabsorbed with the peptide solutions to competitively bind the antibody epitopes to its specific antigenic peptide before being applied to the sections. While the control peptide preabsorbed antibodies gave ribbon like punctate labeling at the OPL, antigenic peptide blocked antibodies showed no staining, henceforth proving their specificity. Rabbit polyclonal anti-RIBEYE (U2656) was used as an internal control antibody for the sections Figs (48 & 49).

RESULTS

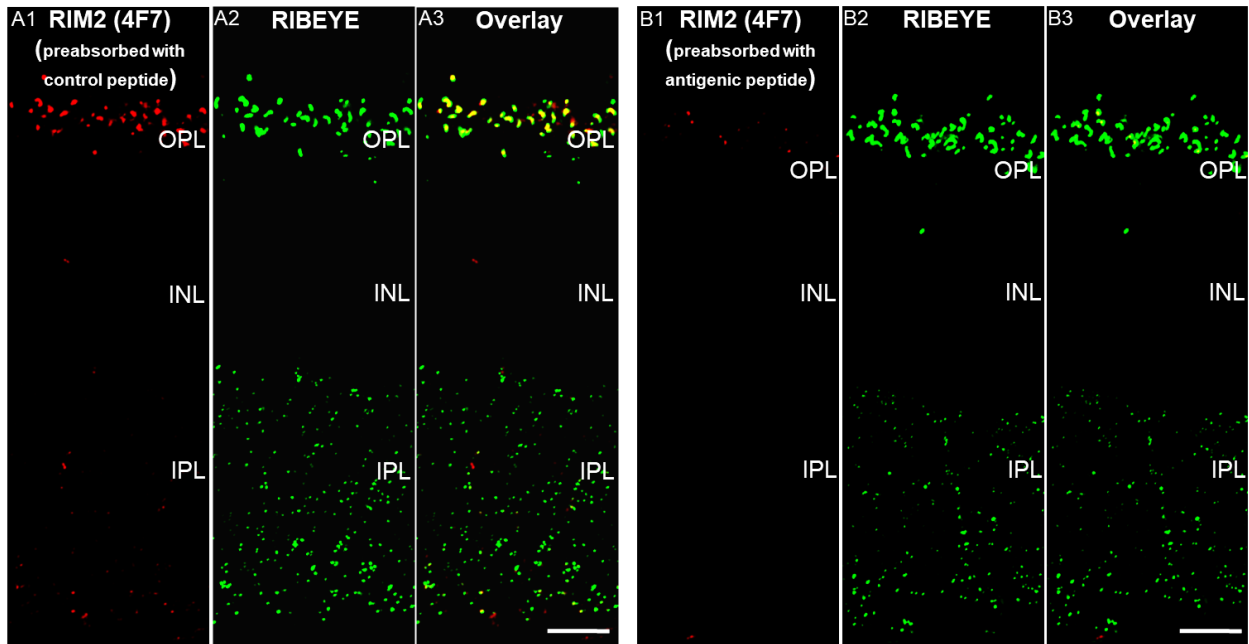


Figure 48: RIM2 (4F7) blocked with control and antigenic peptide is co-immunolabeled with polyclonal anti-RIBEYE antibody on WT mice retinal sections

In Panel A control peptide preincubated RIM2 (4F7) with donkey anti-mouse Alexa 568 (A1) show punctate ribbon-like labeling at the OPL, coinciding with OPL-RIBEYE punctas stained with goat anti-rabbit Alexa 647 (A2). Panel B illustrates the absence of immunostaining of RIM2 (4F7) with donkey anti-mouse Alexa 568 (B1) on being preincubated with the antigenic RIM2 peptide while anti-RIBEYE with goat anti-rabbit Alexa 647 (B2) acts as an internal control for the section, labeling the OPL and IPL. A3 and B3 depict the merged images of A1/A2 and B1/B2. Abbreviations: OPL-outer plexiform layer, INL-inner nuclear layer, IPL-inner plexiform layer; Scale bar = 5 μ m (A, B).

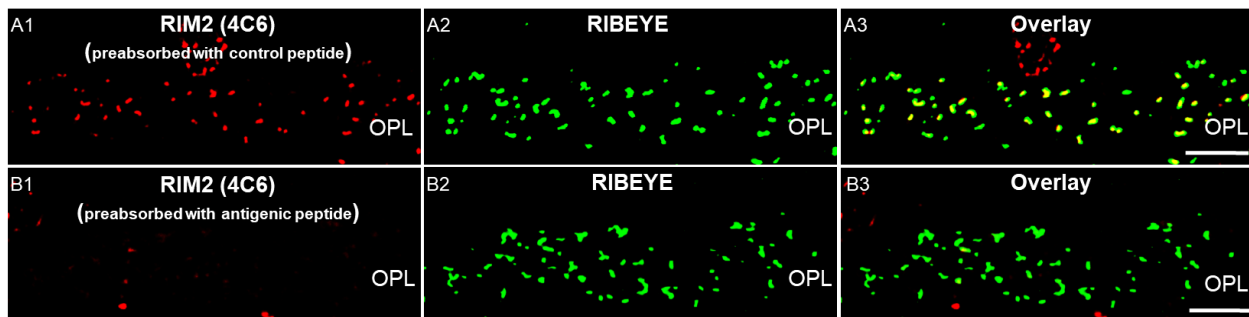


Figure 49: RIM2 (4C6) blocked with control and antigenic peptide is co-immunolabeled with polyclonal anti-RIBEYE antibody on WT mice retinal sections

RIM2 (4C6) preincubated with control peptide on staining with donkey anti-mouse Alexa 568 (A1) gave punctate labeling at the ribbons marked out by the anti-RIBEYE antibody with goat anti-rabbit Alexa 647 (A2). On being blocked with the antigenic RIM2 peptide, RIM2 (4C6) loses its labeling with donkey anti-mouse Alexa 568 (B1) while anti-RIBEYE antibody with goat anti-rabbit Alexa 647 (B2) acts as an internal control for the section. A3 and B3 are the merged images for A1/A2 and B1/B2 respectively. Abbreviations: OPL-outer plexiform layer; Scale bar = 5 μ m (A, B).

RESULTS

3.7.4 RIM1,2 rabbit polyclonal antibody

To prove the specificity of RIM1,2 antibody, RIM2-PCMV (Wang et al., 1997) and RIM2-mCherry N1 (Alpadi et al., 2008) plasmids were overexpressed in HEK cells. The untransfected and transfected HEK cell lysates were then immune blotted with the antibody. The antibody detected the antigen in the RIM2 transfected HEK cell lysates blot at ~190 kDa; the shift in size of RIM2 from predicted molecular weight of 160 kDa could be because of some post translational modifications. The antibody also recognized a band at ~220 kDa for the RIM2/mCherry lane, the additional weight of mCherry of 28.8 kDa resulting into an upward shift of the band. However, RIM1,2 showed no band in the untransfected HEK cell lysates blot thus proving its specificity. To check for the loading control we incubated the blot with fodrin after stripping it. Fodrin bands at ~260 kDa showed that the loading was more or less equal in all the three lanes (Fig. 50).

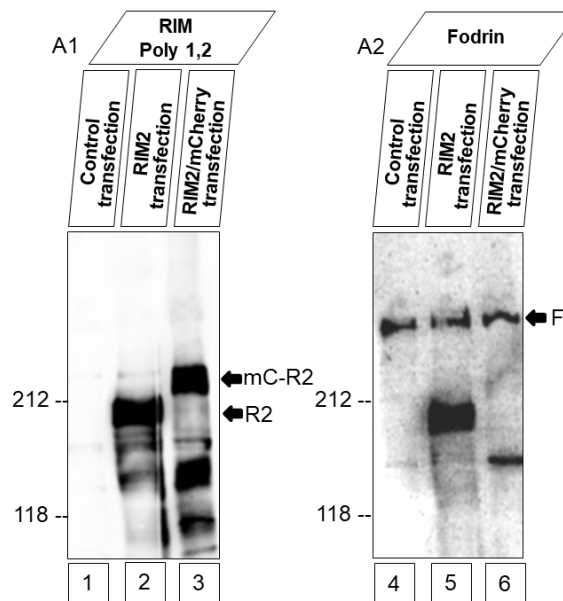


Figure 50: Western blot of RIM1,2 polyclonal antibody on RIM2 transfected HEK293T cell lysates

A1 depicts the blot lanes for the untransfected HEK293T cell lysate (1), RIM2 PCMV plasmid transfected HEK293T cell lysate (2) and RIM2 mCherry N1 plasmid transfected HEK293T cell lysates. The RIM1,2 antibody detects a ~190 kDa band in lane2 (marked by arrow R2) and a ~220 kDa band in lane 3 (marked by arrow mC-R2), showing upward migration of RIM2 band on being expressed in fusion with mCherry. Lane1 (A1) shows no band thus exhibiting specificity of the RIM1,2 polyclonal antibody. A2 shows fodrin incubation of the very same same blot strip (A1) after stripping. The lanes 4, 5 and 6 correspond to the lanes 1, 2 and 3 respectively. Equal loading is manifested through the equally strong fodrin bands (marked out by arrow F) in lanes 4, 5 and 6 at ~260 kDa mark. The proteins were separated by a 5% acrylamide SDS PAGE. Abbreviations: R2-RIM2, mC-mCherry, F-Fodrin. RIM2 mCherry N1 cloning was performed by Dr. Mayur Dembla.

4 DISCUSSION

Retinal pathology in MS has gained importance over the last decade. Inflammatory changes in the eye like optic neuritis, uveitis or retinal phlebitis have long been associated with multiple sclerosis (Calabresi et al., 2010; Kale, 2016). However, retinal nerve fiber layer (RNFL) and ganglion cell-inner plexiform layer (GC-IPL) thinning in MS is relatively a new finding (Green et al., 2010). Many groups have observed these retinal changes occurring in MS patients independent of demyelination of the optic nerve (Fisher et al., 2006; Oberwahrenbrock et al., 2013; Petracca et al., 2017). Therefore, it rules out the theory of trans-synaptic retrograde neurodegeneration behind it and bolsters the hypothesis of a common neuropathologic degenerative process bringing about lesions in the grey matter and neuronal loss in the retina (Calabresi et al., 2010; Petracca et al., 2017). Some of the optical coherence studies have also showed the involvement of the outer retinal layers, the outer and inner nuclear layers (ONL, INL) in the disease process independent of optic neuritis (Saidha et al., 2011; Behbahani et al., 2017). These retinal neuronal changes have even been claimed to be the harbinger of a more aggressive form of the disease (Saidha et al., 2011; Behbahani et al., 2017). Another interesting fact is that the retina is an unmyelinated tissue. Thus, the antigenic target for the disease can no longer be confined to myelin (Calabresi et al., 2010; Dendrou et al., 2015). These findings show that understanding retinal pathology in MS and its animal models can take us a long way into understanding the disease itself.

In my PhD work I have analyzed whether the calcium homeostasis machinery in rod photoreceptor ribbon synapses is affected in experimental autoimmune encephalitis (EAE) preclinical phase. EAE is a well-established animal model for multiple sclerosis. (Dembla et al., 2018) showed that in EAE mice synaptic activity of the photoreceptor synapses is significantly compromised at day 9 after induction, before alterations in the optic nerve develop. Since exocytosis in photoreceptor synapses is a Ca^{2+} mediated process (Heidelberger et al., 2005; Thoreson, 2007), I wanted to explore for possible malfunctions in calcium signaling in photoreceptor synapses of EAE mice in its preclinical stage.

Synaptic transmission through tonic glutamate neurotransmitter release in rod photoreceptor ribbon synapses is brought about by sustained calcium entry at the base of the ribbons via the L-type $Ca_v1.4$ channels (Cho & Von Gersdorff, 2012). $\alpha1F$ forms the pore forming subunit of $Ca_v1.4$ channels (Baumann et al., 2004), along with $\beta2$ and $\alpha2\delta4$ as its auxiliary subunits (Ball & Gregg,

DISCUSSION

2002; Wycisk, et al., 2006a). My initial work was focused on analyzing the expression of Ca_v1.4 channel subunits in EAE photoreceptor synapses at a preclinical phase on day 9 after EAE induction. This is because proper co-expression and functional interactions of α 1F, β 2 and α 2 δ 4 subunits of Ca_v1.4 are vital to correct localization and functioning of the Ca_v1.4 channels in rod photoreceptor ribbon synapses (Mansergh et al., 2005; Wycisk et al., 2006b; Lee et al., 2014; Katiyar et al., 2015; Wang et al., 2017). Mutations in CACNA1F gene encoding the α 1F subunit are known to be responsible for incomplete X-linked congenital stationary blindness (CSNB) and X-linked cone rod dystrophy (CORDX3) in humans (Wutz et al., 2002; Doering et al., 2007).

I found significant reduction in overall intensity of immunosignals of the α 1F subunit in EAE mice retinal sections but the cluster count remained similar to that in the control (CFA). To find an answer to the decreased fluorescence I took my investigation to a higher resolution level. Using 3D SR-SIM I observed that the mean contour length of the punctate immunosignals of Ca_v1.4 α 1F in EAE mice retina was significantly shorter than that in the control. Each Ca_v1.4 channel punctate labeling at the base of a horse shoe shaped ribbon, is actually composed of hundreds of Ca_v1.4 channels in a cluster (Raviola & Gilula, 1975; Doering et al., 2005). Thus, the decreased contour length of Ca_v1.4 α 1F punctas in EAE meant that the number of Ca_v channels contributing to each Ca_v1.4 cluster was lower in EAE, though the number of clusters remained unaltered. My results were also supported by light microscopy studies using Ca_v β 2 antibodies at a higher resolution level. Immunofluorescence expression of Ca_v β 2 (Ball et al., 2002), changed similarly as Ca_v1.4 α 1F. Immunofluorescence intensity of Ca_v β 2 signals and mean cluster length of Ca_v1.4 channel as delineated by the Ca_v β 2 antibodies were significantly reduced in EAE mice photoreceptor synapses. But there was no significant reduction in the count of the Ca_v β 2 punctas in EAE compared to the control.

Besides the reduction in their synaptic enrichment, western blot analyses were performed to investigate the total protein content of the two Ca_v1.4 subunits in MOG/CFA mice retina. Interestingly, while total protein expression level of Ca_v β 2 in MOG/CFA mice retinal lysates showed a significant reduction compared to its control (CFA), Ca_v1.4 α 1F showed no change. Ca_v β 2 is responsible for membrane trafficking of the pore-forming α 1F subunits to the membrane (Ball et al., 2002). As a result, a significant decrease in its total protein content in EAE retina could explain the reduction in synaptic enrichment of the Ca_v1.4 α 1F subunits with no significant loss in its total expression level. The difference in total protein expression levels of the two Ca_v1.4 subunits in EAE retinas can perhaps be explained by the finding of Belkacemi et al., 2018, that β subunits have additional functions beyond their role as a Ca_v channel subunit. Hence it can be postulated that the

DISCUSSION

change in expression level of $\text{Ca}_v\beta 2$ in preclinical phase of EAE is not limited to its role as a $\text{Ca}_v1.4$ subunit. In support of this proposal, the groups of Prof. Dr. Veit Flockerzi, Saarland University and Prof. Dr. Ricarda Diem are exploring potential roles of $\text{Ca}_v\beta$ in EAE mice, independent of its channel function.

Besides the diminished vesicular cycling in EAE photoreceptor synapses at a preclinical phase (Dembla et al., 2018), declusterification of $\text{Ca}_v1.4$ channels at light microscopy can also be linked to the decrease in fluorescence of RIBEYE in EAE retina (Dembla et al., 2018). Ribbons along with their tethered synaptic vesicles and L-type $\text{Ca}_v 1.4$ channels in photoreceptor terminals make up a tightly coupled exocytic machinery (Mercer & Thoreson, 2011; Vaithianathan & Matthews, 2014). Previous studies in zebrafish hair ribbon synapses have shown that optimal RIBEYE expression is necessary for proper expression and localization of $\text{Ca}_v1.3$ channels (Sheets et al., 2011; Lv et al., 2012). Not only that, mice knock outs of $\text{Ca}_v1.4 \alpha 1\text{F}$ and $\text{Ca}_v\beta 2$ have been observed to produce dot like unanchored ribbons in rod photoreceptor terminals while their bipolar ribbon synapses remain unaltered (Liu et al., 2013; Katiyar et al., 2015).

I observed very strong reduction in synaptic enrichment of $\text{Ca}_v1.4 \alpha 1\text{F}$ and $\text{Ca}_v \beta 2$ proteins at the active zone of EAE rod photoreceptor synapses at a preclinical stage. These significant morphological changes of $\text{Ca}_v1.4$ channels in EAE mice encouraged me to investigate whether they were being translated into alterations in depolarization evoked calcium influx as well. FURA2-AM Ca^{2+} imaging experiments showed that depolarization evoked Ca^{2+} influx in EAE photoreceptor synapses, on day9 after induction, was diminished not only in its amplitude but also exhibited slower kinetics compared to its control (CFA) counterpart. The calcium imaging data thus proved that the deficit in $\text{Ca}_v1.4$ channel clustering resulted into reduced depolarization-evoked calcium influx in EAE photoreceptor synapses. This could explain the decreased synaptic vesicle release in EAE photoreceptor synapses, as observed by Dembla et al., 2018.

Though inactivation of $\text{Ca}_v1.4$ channels is almost negligible physiologically (Baumann et al., 2004; McRory et al., 2004; Wahl-Schott et al., 2006), strong depolarization for a sufficiently long time as in case of my studies could result into inactivation of the $\text{Ca}_v1.4$ channels. The difference in the calcium influx amplitudes could mean that EAE calcium channels have a lower threshold for inactivation compared to the control.

In our model of EAE, clinical symptoms such as limp tail, paralyzed hind limbs develop from about day 10 after induction (Day 0 being the day of induction) (Fairless et al., 2012; Bittner et al., 2014) (Fig. 16). In order to better understand how Ca^{2+} influx was affected in the preclinical phase,

DISCUSSION

besides measuring Ca^{2+} influx on day 9 after immunization, I measured it on earlier days as well. FURA2-AM recordings showed similar difference in Ca^{2+} influx in EAE compared to CFA on days 7 and 8, as on day 9. Thus, I could see that in EAE alterations of physiological significance started occurring as early as day 7 after induction and did not worsen by day 9. It would be interesting to find out how early these changes start developing but would require bigger cohorts for study. Furthermore, I wanted to rule out the possibility that some unknown contamination in our self-made CFA and MOG injectable emulsions was responsible for the observed phenotypes. So, I repeated all my calcium imaging investigations in mice immunized with a commercial EAE induction kit (Hooke's Laboratories), obtaining similar results as in the self-made emulsion injected ones.

RIMs interact with Ca_v channels, tethering them to the active zone in conventional as well as ribbon synapses (Hibino et al., 2002; Schoch et al., 2006; Kiyonaka et al., 2007; Kaeser et al., 2011; Gandini & Felix, 2011). Moreover, they also positively regulate Ca_v channel function through their gating properties (Kiyonaka et al., 2007; Gebhart et al., 2010; Gandini et al., 2011; Grabner et al., 2015). Therefore, the dysregulated Ca_v channel clustering and diminished depolarization-evoked Ca^{2+} influx in EAE photoreceptor synapses encouraged me to determine how RIM expression was influenced in EAE photoreceptor synapses preclinically. RIMs exist in two different compartments in photoreceptor ribbon synapses, the ribbon associated compartment comprised of RIM1 and the active zone compartment of RIM2 (Dieck et al., 2005). I concentrated primarily on the analyses of RIM2 because of its stronger expression (Grabner et al., 2015) and localization at the active zone of photoreceptors along with $\text{Ca}_v1.4$ channels (Dieck et al., 2005).

Immunoanalysis of RIM 2 at light microscopy level with two independent antibodies exhibited a significant reduction in its expression in EAE mice photoreceptor synapses. However the puncta count in both CFA and MOG/CFA groups remained similar. The subsequent question was whether RIM2 expression was reduced at a total protein level in EAE retinas. Since, the RIM2 monoclonal antibodies failed to work on western blots of mice retinal lysates, I used a well characterized rabbit polyclonal RIM1,2 antibody (Schoch et al., 2006). I observed a highly significant reduction in the total protein content of both the RIMs in EAE mice retina. RIM1 in EAE retina was decreased by $\approx 25\%$ and RIM2 by $\approx 40\%$. This reduction in total expression levels of RIMs 1 and 2, particularly RIM2 along with the deficit in synaptic enrichment of $\text{Ca}_v1.4$ channels could most likely be the primary reasons behind the diminished depolarized-evoked Ca^{2+} influx and synaptic activity in EAE photoreceptor terminals.

DISCUSSION

The finding that EAE photoreceptor terminals exhibit reduced expression of RIBEYE (Dembla et al., 2018), RIM2 and $\text{Ca}_v1.4$ channels along with diminished Ca^{2+} influx and synaptic vesicle release (Dembla et al., 2018) is intriguing. Previous studies have also provided evidences for a very tight coupling between RIM2, Ca_v channels and RIBEYE in Ca^{2+} triggered exocytosis in ribbon synapses, where loss of one of the three proteins adversely affects the expression of the other two. While adult $\text{Ca}_v1.4$ deficient mice were observed to exhibit altered expression and localization of RIM2 and RIBEYE at the outer plexiform layer (Zabouri & Haverkamp, 2013), reduction in expression of RIBEYE in photoreceptor terminals of zebrafish led to shorter ribbons, reduced expression of RIM2 and declustering of CACNA1F (Lv et al., 2012). Besides that, RIM2 α deficient IHCs have been shown to cluster fewer $\text{Ca}_v1.3$ calcium channels at its active zone, resulting in reduced Ca^{2+} entry and Ca^{2+} evoked release in the synapses (Jung et al., 2015). RIM1,2 conditional double knockouts in photoreceptor synapses were also reported to severely impair Ca^{2+} influx and Ca^{2+} triggered exocytosis, but with no change in the number of ribbons and Ca_v channel units (Grabner et al., 2015). Interestingly, EAE photoreceptor synapses also demonstrate reduced depolarization-evoked Ca^{2+} influx and exocytosis with no change in the number of $\text{Ca}_v1.4$ channel clusters at a preclinical stage.

Besides, finding alterations in the Ca^{2+} influx machinery, I had observed that the baseline ratiometric (340/380) fluorescence of FURA2 loaded MOG/CFA retinal slices was significantly higher than that of CFA. Thus, it can be construed that in ex vivo physiological conditions, basal intracellular calcium concentration was higher in MOG/CFA photoreceptor terminals. The higher basal intracellular calcium concentration in EAE photoreceptor terminals could also adversely affect the chemical component of the electrochemical gradient across which calcium ions enter the terminals through the high voltage gated Ca_v channels, resulting into lower Ca^{2+} influx. To account for this dysregulated calcium homeostasis, I wanted to explore the Ca^{2+} efflux machinery in EAE photoreceptor terminals. Since PMCA is the principal mode of Ca^{2+} extrusion in photoreceptor terminals (Morgans et al., 1998), as a preliminary study I focussed on analyzing their expression. Of the two most abundant retinal isoforms of PMCA (Duncan et al., 2006), PMCA2 showed significantly decreased expression in both of the retinal synaptic layers. Amongst all the PMCA isoforms, it has the highest calcium affinity (Hilfiker et al., 1994) and has also been observed to be the fastest Ca^{2+} pump to be activated in response to an increase in intracellular calcium (Caride et al., 2001; Brini et al., 2003). The reduced synaptic expression of PMCA2 could be the cause of higher basal calcium concentration in EAE photoreceptor terminals. Alterations in expression or activity of PMCA2 and

DISCUSSION

NCX have been implicated in multiple sclerosis and its animal models by affecting calcium homeostasis and inducing calcium mediated apoptosis of cells (Kurnellas et al., 2007). Significant reduction in PMCA2 transcript level has also been reported in early spinal-cord neuropathology during acute and chronic EAE. On the other hand, expression of other ions pumps including NCX and SERCA were reduced at much later stages of the diseases. Interestingly, the other PMCA isoforms (eg. PMCA1) remained unaltered during the entire disease course (Nicot et al., 2003; Nicot et al., 2005). My investigations also showed that PMCA1 expression in EAE retinas remain unaltered at a preclinical phase. The nature of alteration of PMCA expressions can be regarded as a common point in neuropathology of myelinated and unmyelinated neurons in EAE.

Besides PMCA1, PSD95—a presynaptic scaffold protein of photoreceptor synapses (Koulen et al., 1998; Maxeiner et al., 2016) also remains unaltered in EAE retina at OPL and IPL both. Thus, I observed that all protein expressions do not change in EAE retina at a preclinical phase. PMCA1 and PSD95, both of which are membrane bound proteins were unaltered in the EAE mice retina. PSD95 being a marker for synaptic strength (Ehrlich et al., 2007; Chen et al., 2011) affirms that structural integrity of photoreceptor synapses in EAE mice remains intact at the preclinical phase. PSD95 expression has been seen to undergo profound loss in lumbo-sacral spinal cord (LSSC) and hippocampal neurons in acute episodes of EAE but not in its preclinical phase (Zhu et al., 2003; Bellizzi et al., 2016). Therefore, photoreceptor synapses remain morphologically whole and active in preclinical EAE, although functionally compromised.

Decrease in expression of (I) $Ca_v1.4$ channel proteins, (II) RIMs and (III) PMCA2, along with (IV) reduced depolarization-induced calcium influx and (V) increased basal calcium concentration in photoreceptor terminals of EAE mice demonstrate that the calcium homeostatic environment is severely disturbed in EAE. Furthermore, this research opens up various other promising areas of research. Ca^{2+} influx through L-type $Ca_v1.4$ channels is absolutely essential for neurotransmitter release. Nevertheless, normal sustained glutamate release in rod photoreceptor synapses also requires Ca^{2+} release from internal ER stores through CICR (calcium induced calcium release) (Suryanarayanan & Slaughter, 2006; Cadetti et al., 2006; Babai et al., 2010). Further, endogenous Ca^{2+} buffering (Krizaj & Copenhagen, 2002; Van Hook & Thoreson, 2014) and other Ca^{2+} clearance mechanisms (Morgans et al., 1998; Krizaj, 2005) also play crucial roles in maintaining a calcium homeostatic environment in photoreceptor synapses. Thus, to have a holistic understanding of Ca^{2+} homeostatic changes in EAE photoreceptor synapses, one can explore these additional mechanisms.

DISCUSSION

The most important finding from my thesis is that several regulatory proteins of Ca^{2+} homeostasis and synaptic Ca^{2+} inflow are adversely affected in photoreceptor terminals of EAE mice at a preclinical phase. This could be the primary reason behind the altered synaptic function in EAE mice photoreceptor terminals as observed by Dembla et al., 2018. EAE is a very well established animal model for multiple sclerosis. Very recent electrophysiological studies of Hanson et al., 2018; You et al., 2018 have shown relatively poor synaptic functioning of the outer retina in multiple sclerosis patients at an early time point independent of optic neuritis. This thesis is one of the first attempts in understanding the pathophysiological changes of outer retinal synaptic calcium signaling in a multiple sclerosis animal model (EAE) at a preclinical stage. It takes a vital step forward in discerning a more widespread form of MS pathology other than targeting of myelinated tissues.

5 REFERENCES

- Al-Louzi, O. A., Bhargava, P., Newsome, S. D., Balcer, L. J., Frohman, E. M., Crainiceanu, C., Calabresi, P. A., Saidha, S. (2016). Outer retinal changes following acute optic neuritis. *Multiple Sclerosis Journal*, *22*, 362-372.
- Alpadi, K., Magupalli, V. G., Käppel, S., Köblitz, L., Schwarz, K., Seigel, G. M., Sung, C.-H., Schmitz, F. (2008). RIBEYE recruits Munc119, a mammalian ortholog of the *Caenorhabditis elegans* protein unc119, to synaptic ribbons of photoreceptor synapses. *Journal of Biological Chemistry*, *283*, 26461-26467.
- Alvarez, J. I., Cayrol, R., & Prat, A. (2011). Disruption of central nervous system barriers in multiple sclerosis. *Biochimica et Biophysica Acta (BBA)-Molecular Basis of Disease*, *1812*, 252-264.
- Andrews-Zwilling, Y. S., Kawabe, H., Reim, K., Varoqueaux, F., & Brose, N. (2006). Binding to Rab3A-interacting molecule RIM regulates the presynaptic recruitment of Munc13-1 and ubMunc13-2. *Journal of Biological Chemistry*, *281*, 19720-19731.
- Anjum, R., Ayoubian, H., & Schmitz, F. (2014). Differential synaptic distribution of the scaffold proteins Cask and Caskin1 in the bovine retina. *Molecular and Cellular Neuroscience*, *62*, 19-29.
- Atkins, E. J., Biousse, V., & Newman, N. J. (2006). The natural history of optic neuritis. *Reviews in neurological diseases*, *3*, 45-56.
- Babai, N., Morgans, C. W., & Thoreson, W. B. (2010). Calcium-induced calcium release contributes to synaptic release from mouse rod photoreceptors. *Neuroscience*, *165*, 1447-1456.
- Ball, S. L., & Gregg, R. G. (2002). Using mutant mice to study the role of voltage-gated calcium channels in the retina. In *Photoreceptors and Calcium* (pp. 439-450). Springer.
- Ball, S. L., Powers, P. A., Shin, H.-S., Morgans, C. W., Peachey, N. S., & Gregg, R. G. (2002). Role of the $\beta 2$ subunit of voltage-dependent calcium channels in the retinal outer plexiform layer. *Investigative ophthalmology & visual science*, *43*, 1595-1603.
- Barnes, S., & Kelly, M. E. (2002). Calcium channels at the photoreceptor synapse. In *Photoreceptors and calcium* (pp. 465-476). Springer.
- Barreto-Chang, O. L., & Dolmetsch, R. E. (2009). Calcium imaging of cortical neurons using Fura-2 AM. *Journal of visualized experiments: JoVE*.
- Baumann, L., Gerstner, A., Zong, X., Biel, M., & Wahl-Schott, C. (2004). Functional characterization of the L-type Ca^{2+} channel Cav1.4 $\alpha 1$ from mouse retina. *Investigative ophthalmology & visual science*, *45*, 708-713.

REFERENCES

- Bech-Hansen, N. T., Naylor, M. J., Maybaum, T. A., Pearce, W. G., Koop, B., Fishman, G. A., Mets, M., Musarella, M. A., Boycott, K. M. (1998). Loss-of-function mutations in a calcium-channel α 1-subunit gene in Xp11.23 cause incomplete X-linked congenital stationary night blindness. *Nature genetics*, *19*, 264.
- Becker, L., Schnee, M. E., Niwa, M., Sun, W., Maxeiner, S., Talaei, S., Kachar, B., Rutherford, M. A., Ricci, A. J. (2018). The presynaptic ribbon maintains vesicle populations at the hair cell afferent fiber synapse. *eLife*, *7*, e30241.
- Behbehani, R., Al-Hassan, A. A., Al-Salahat, A., Sriraman, D., Oakley, J. D., & Alroughani, R. (2017). Optical coherence tomography segmentation analysis in relapsing remitting versus progressive multiple sclerosis. *PloS one*, *12*, e0172120.
- Belkacemi, A., Hui, X., Wardas, B., Laschke, M. W., Wissenbach, U., Menger, M. D., Lipp, P., Beck, A., Flockerzi, V. (2018). IP3 receptor-dependent cytoplasmic Ca^{2+} signals are tightly controlled by CaV β 3. *Cell reports*, *22*, 1339-1349.
- Bellizzi, M. J., Geathers, J. S., Allan, K. C., & Gelbard, H. A. (2016). Platelet-activating factor receptors mediate excitatory postsynaptic hippocampal injury in experimental autoimmune encephalomyelitis. *Journal of Neuroscience*, *36*, 1336-1346.
- Berntson, A. K., & Morgans, C. W. (2003). Distribution of the presynaptic calcium sensors, synaptotagmin I/II and synaptotagmin III, in the goldfish and rodent retinas. *Journal of vision*, *3*, 3-3.
- Berridge, M. J. (1998). Neuronal calcium signaling. *Neuron*, *21*, 13-26.
- Betz, A., Thakur, P., Junge, H. J., Ashery, U., Rhee, J.-S., Scheuss, V., Rosenmund, C., Rettig, J., Brose, N. (2001). Functional interaction of the active zone proteins Munc13-1 and RIM1 in synaptic vesicle priming. *Neuron*, *30*, 183-196.
- Bittner, S., Afzali, A. M., Wiendl, H., & Meuth, S. G. (2014). Myelin oligodendrocyte glycoprotein (MOG35-55) induced experimental autoimmune encephalomyelitis (EAE) in C57BL/6 mice. *Journal of visualized experiments: JoVE*.
- Bloomfield, S. A., & Dacheux, R. F. (2001). Rod vision: pathways and processing in the mammalian retina. *Progress in retinal and eye research*, *20*, 351-384.
- Bost, A., Pasche, M., Schirra, C., & Becherer, U. (2013). Super-resolution microscopy in studying neuroendocrine cell function. *Frontiers in neuroscience*, *7*, 222.
- Brini, M., Coletto, L., Pierobon, N., Kraev, N., Guerini, D., & Carafoli, E. (2003). A comparative functional analysis of plasma membrane Ca^{2+} pump isoforms in intact cells. *Journal of Biological Chemistry*, *278*, 24500-24508.
- Buckley, K., & Kelly, R. B. (1985). Identification of a transmembrane glycoprotein specific for secretory vesicles of neural and endocrine cells. *The Journal of cell biology*, *100*, 1284-1294.

REFERENCES

- Cadetti, L., Bryson, E. J., Ciccone, C. A., Rabl, K., & Thoreson, W. B. (2006). Calcium-induced calcium release in rod photoreceptor terminals boosts synaptic transmission during maintained depolarization. *European Journal of Neuroscience*, *23*, 2983-2990.
- Calabresi, P. A., Balcer, L. J., & Frohman, E. M. (2010). Retinal pathology in multiple sclerosis: insight into the mechanisms of neuronal pathology. *Brain*, *133*, 1575-1577.
- Camello, C., Lomax, R., Petersen, O. H., & Tepikin, A. V. (2002). Calcium leak from intracellular stores_the enigma of calcium signalling. *Cell calcium*, *32*, 355-361.
- Cameron, M., Kékesi, O., Morley, J. W., Tapson, J., Breen, P. P., Schaik, A., Buskila, Y. (2016). Calcium imaging of AM dyes following prolonged incubation in acute neuronal tissue. *PloS one*, *11*, e0155468.
- Caride, A. J., Filoteo, A. G., Penheiter, A. R., Paszty, K., Enyedi, A., & Penniston, J. T. (2001). Delayed activation of the plasma membrane calcium pump by a sudden increase in Ca^{2+} : fast pumps reside in fast cells. *Cell calcium*, *30*, 49-57.
- Castellano-Muñoz, M., & Ricci, A. J. (2014). Role of intracellular calcium stores in hair-cell ribbon synapse. *Frontiers in cellular neuroscience*, *8*, 162.
- Catterall, W. A. (2011). Voltage-gated calcium channels. *Cold Spring Harbor perspectives in biology*, *3*, a003947.
- Catterall, W. A., & Few, A. P. (2008). Calcium channel regulation and presynaptic plasticity. *Neuron*, *59*, 882-901.
- Catterall, W. A., Perez-Reyes, E., Snutch, T. P., & Striessnig, J. (2005). International Union of Pharmacology. XLVIII. Nomenclature and structure-function relationships of voltage-gated calcium channels. *Pharmacological reviews*, *57*, 411-425.
- Chang, J., Voorhees, T. J., Liu, Y., Zhao, Y., & Chang, C.-H. (2010). Interleukin-23 production in dendritic cells is negatively regulated by protein phosphatase 2A. *Proceedings of the National Academy of Sciences*, *107*, 8340-8345.
- Chen, C., & Okayama, H. (1987). High-efficiency transformation of mammalian cells by plasmid DNA. *Molecular and cellular biology*, *7*, 2745-2752.
- Chen, M., Van Hook, M. J., & Thoreson, W. B. (2015). Ca^{2+} diffusion through endoplasmic reticulum supports elevated intraterminal Ca^{2+} levels needed to sustain synaptic release from rods in darkness. *Journal of Neuroscience*, *35*, 11364-11373.
- Chen, X., & Oppenheim, J. J. (2014). Th17 cells and Tregs: unlikely allies. *Journal of leukocyte biology*, *95*, 723-731.
- Chen, X., Nelson, C. D., Li, X., Winters, C. A., Azzam, R., Sousa, A. A., Leapman, R. D., Gainer, H., Sheng, M., Reese, T. S. (2011). PSD-95 is required to sustain the molecular organization of the postsynaptic density. *Journal of Neuroscience*, *31*, 6329-6338.

REFERENCES

- Chen, X., Winkler-Pickett, R. T., Carbonetti, N. H., Ortaldo, J. R., Oppenheim, J. J., & Howard, O. M. (2006). Pertussis toxin as an adjuvant suppresses the number and function of CD4⁺ CD25⁺ T regulatory cells. *European journal of immunology*, *36*, 671-680.
- Cho, S., & Gersdorff, H. (2012). Ca²⁺ influx and neurotransmitter release at ribbon synapses. *Cell calcium*, *52*, 208-216.
- Choi, S.-Y., Jackman, S., Thoreson, W. B., & Kramer, R. H. (2008). Light regulation of Ca²⁺ in the cone photoreceptor synaptic terminal. *Visual neuroscience*, *25*, 693-700.
- Constantinescu, C. S., Farooqi, N., O'brien, K., & Gran, B. (2011). Experimental autoimmune encephalomyelitis (EAE) as a model for multiple sclerosis (MS). *British journal of pharmacology*, *164*, 1079-1106.
- Cooper, B., Hemmerlein, M., Ammermüller, J., Imig, C., Reim, K., Lipstein, N., Kalla, S., Kawabe, H., Brose, N., Brandstätter, J. H., Varoqueaux, F. (2012). Munc13-independent vesicle priming at mouse photoreceptor ribbon synapses. *Journal of Neuroscience*, *32*, 8040-8052.
- Cribbs, D. H., Ghochikyan, A., Vasilevko, V., Tran, M., Petrushina, I., Sadzikava, N., Babikyan, D., Kesslak, P., Kieber-Emmons, T., Cotman, C. W., Agadjanyan, M. G. (2003). Adjuvant-dependent modulation of Th1 and Th2 responses to immunization with β -amyloid. *International immunology*, *15*, 505-514.
- Cua, D. J., Sherlock, J., Chen, Y. I., Murphy, C. A., Joyce, B., Seymour, B., Lucian, L., To, W., Kwan, S., Churakova, T., Zurawski, S., Wiekowski, M., Lira, S. A., Gorman, D., Kastelein, R. A., Sedgwick, J. D. (2003). Interleukin-23 rather than interleukin-12 is the critical cytokine for autoimmune inflammation of the brain. *Nature*, *421*, 744.
- Dartt, D. A. (2010). *Encyclopedia of the Eye* (Vol. 1). Academic Press.
- Davies, J. N., & Zamponi, G. W. (2008). Old proteins, developing roles: The regulation of calcium channels by synaptic proteins. *Channels*, *2*, 130-138.
- De Winter, J. C. (2013). Using the Student's t-test with extremely small sample sizes. *Practical Assessment, Research & Evaluation*, *18*.
- Dembla, M., Kesharwani, A., Natarajan, S., Fecher-Trost, C., Fairless, R., Williams, S. K., Flockerzi, V., Diem, R., Schwarz, K., Schmitz, F. (2018). Early auto-immune targeting of photoreceptor ribbon synapses in mouse models of multiple sclerosis. *EMBO molecular medicine*, *10*, e8926.
- Dembla, M., Wahl, S., Katiyar, R., & Schmitz, F. (2014). ArfGAP3 is a component of the photoreceptor synaptic ribbon complex and forms an NAD (H)-regulated, redox-sensitive complex with RIBEYE that is important for endocytosis. *Journal of Neuroscience*, *34*, 5245-5260.
- Dendrou, C. A., Fugger, L., & Friese, M. A. (2015). Immunopathology of multiple sclerosis. *Nature Reviews Immunology*, *15*, 545.

REFERENCES

- Dieck, S., & Brandstätter, J. H. (2006). Ribbon synapses of the retina. *Cell and tissue research*, 326, 339-346.
- Dieck, S., Altmann, W. D., Kessels, M. M., Qualmann, B., Regus, H., Brauner, D., Fejtová, A., Bracko, O., Gundelfinger, E. D., Brandstätter, J. H. (2005). Molecular dissection of the photoreceptor ribbon synapse: physical interaction of Bassoon and RIBEYE is essential for the assembly of the ribbon complex. *The Journal of cell biology*, 168, 825-836.
- Dieckmann-Schuppert, A., & Schnittler, H.-J. (1997). A simple assay for quantification of protein in tissue sections, cell cultures, and cell homogenates, and of protein immobilized on solid surfaces. *Cell and tissue research*, 288, 119-126.
- Doering, C. J., Hamid, J., Simms, B., McRory, J. E., & Zamponi, G. W. (2005). Cav1. 4 encodes a calcium channel with low open probability and unitary conductance. *Biophysical journal*, 89, 3042-3048.
- Doering, C. J., Peloquin, J. B., & McRory, J. E. (2007). The CaV1. 4 calcium channel: more than meets the eye. *Channels*, 1, 4-11.
- Dolphin, A. C. (2013). The $\alpha 2\delta$ subunits of voltage-gated calcium channels. *Biochimica Et Biophysica Acta (BBA)-Biomembranes*, 1828, 1541-1549.
- Dolphin, A. C. (2016). Voltage-gated calcium channels and their auxiliary subunits: physiology and pathophysiology and pharmacology. *The Journal of physiology*, 594, 5369-5390.
- Dowling, J. E. (1987). *The retina: an approachable part of the brain*. Harvard University Press.
- Dowling, J. E., & Werblin, F. S. (1971). Synaptic organization of the vertebrate retina. *Vision research*, 11, 1--12.
- Drenckhahn, D., & Franz, H. (1986). Identification of actin-, alpha-actinin-, and vinculin-containing plaques at the lateral membrane of epithelial cells. *The Journal of Cell Biology*, 102, 1843-1852.
- Duncan, J. L., Yang, H., Doan, T., Silverstein, R. S., Murphy, G. J., Nune, G., Liu, X., Copenhagen, D., Tempel, B. L., Rieke, F., Krizaj, D. (2006). Scotopic visual signaling in the mouse retina is modulated by high-affinity plasma membrane calcium extrusion. *Journal of Neuroscience*, 26, 7201-7211.
- Dutta, D. (2000). Mechanism of store-operated calcium entry. *Journal of biosciences*, 25, 397-404.
- Ehrlich, I., Klein, M., Rumpel, S., & Malinow, R. (2007). PSD-95 is required for activity-driven synapse stabilization. *Proceedings of the National Academy of Sciences*, 104, 4176-4181.
- Eich, M.-L., Dembla, E., Wahl, S., Dembla, M., Schwarz, K., & Schmitz, F. (2017). The calcineurin-binding, activity-dependent splice variant dynamin1xb is highly enriched in synapses in various regions of the central nervous system. *Frontiers in molecular neuroscience*, 10, 230.

REFERENCES

- Fain, G., & Sampath, A. P. (2018). Rod and cone interactions in the retina. *F1000Research*, 7.
- Fairless, R., Williams, S. K., Hoffmann, D. B., Stojic, A., Hochmeister, S., Schmitz, F., Storch, M. K., Diem, R. (2012). Preclinical retinal neurodegeneration in a model of multiple sclerosis. *Journal of Neuroscience*, 32, 5585-5597.
- Farooqi, N., Gran, B., & Constantinescu, C. S. (2010). Are current disease-modifying therapeutics in multiple sclerosis justified on the basis of studies in experimental autoimmune encephalomyelitis? *Journal of neurochemistry*, 115, 829-844.
- Fisher, J. B., Jacobs, D. A., Markowitz, C. E., Galetta, S. L., Volpe, N. J., Nano-Schiavi, M. L., Baier, M. L., Frohman, E. M., Winslow, H., Frohman, T. C., Calabresi, P. A., Maguire, M. G., Cutter, G. R., Balcer, L. J. (2006). Relation of visual function to retinal nerve fiber layer thickness in multiple sclerosis. *Ophthalmology*, 113, 324-332.
- Frank, T., Rutherford, M. A., Strenzke, N., Neef, A., Pangršič, T., Khimich, D., Fejtova, A., Gundelfinger, E. D., Liberman, M. C., Harke, B., Bryan, K. E., Lee, A., Egner, A., Riedel, D., Moser, T. (2010). Bassoon and the synaptic ribbon organize Ca²⁺ channels and vesicles to add release sites and promote refilling. *Neuron*, 68, 724-738.
- Frohman, E. M., Racke, M. K., & Raine, C. S. (2006). Multiple sclerosis_the plaque and its pathogenesis. *New England Journal of Medicine*, 354, 942-955.
- Gandini, M. A., & Felix, R. (2011). Functional interactions between voltage-gated Ca²⁺ channels and Rab3-interacting molecules (RIMs): New insights into stimulus--secretion coupling. *Biochimica et Biophysica Acta (BBA)-Biomembranes*, 1818, 551-558.
- Garrett, B., Dmytriw, A. A., & Maxner, C. (2016). Acute optic neuritis in multiple sclerosis. *CMAJ*, 188, E199--E199.
- Gebhart, M., Juhasz-Vedres, G., Zuccotti, A., Brandt, N., Engel, J., Trockenbacher, A., Kaur, G., Obermair, G. J., Knipper, M., Koschak, A., Striessnig, J., (2010). Modulation of Cav 1.3 Ca²⁺ channel gating by Rab3 interacting molecule. *Molecular and Cellular Neuroscience*, 44, 246-259.
- Glenney Jr, J. R., & Glenney, P. (1983). Fodrin is the general spectrin-like protein found in most cells whereas spectrin and the TW protein have a restricted distribution. *Cell*, 34, 503-512.
- Grabner, C. P., Gandini, M. A., Rehak, R., Le, Y., Zamponi, G. W., & Schmitz, F. (2015). RIM1/2-mediated facilitation of Cav1.4 channel opening is required for Ca²⁺-stimulated release in mouse rod photoreceptors. *Journal of Neuroscience*, 35, 13133-13147.
- Green, A. J., McQuaid, S., Hauser, S. L., Allen, I. V., & Lyness, R. (2010). Ocular pathology in multiple sclerosis: retinal atrophy and inflammation irrespective of disease duration. *Brain*, 133, 1591-1601.

REFERENCES

- Gustafsson, M. G., Shao, L., Carlton, P. M., Wang, C. J., Golubovskaya, I. N., Cande, W. Z., Agard, D. A., Sedat, J. W. (2008). Three-dimensional resolution doubling in wide-field fluorescence microscopy by structured illumination. *Biophysical journal*, *94*, 4957-4970.
- Hanson, J. V., Hediger, M., Manogaran, P., Landau, K., Hagenbuch, N., Schippling, S., Gerth-Kahlert, C. (2018). Outer retinal dysfunction in the absence of structural abnormalities in multiple sclerosis. *Investigative ophthalmology & visual science*, *59*, 549-560.
- Hegedüs, L., Padányi, R., Molnár, J., Pászty, K., Varga, K., Kenessey, I., Sárközy, E., Wolf, M., Grusch, M., Hegyi, Z., Homolya, L., Aigner, C., Garay, T., Hegedüs, B., Tímár, J., Kállay, E., Enyedi, Á. (2017). Histone Deacetylase Inhibitor Treatment Increases the Expression of the Plasma Membrane Ca²⁺Pump PMCA4b and Inhibits the Migration of Melanoma Cells Independent of ERK. *Frontiers in oncology*, *7*, 95.
- Heidelberger, R. (2001). ATP is required at an early step in compensatory endocytosis in synaptic terminals. *Journal of Neuroscience*, *21*, 6467-6474.
- Heidelberger, R., Thoreson, W. B., & Witkovsky, P. (2005). Synaptic transmission at retinal ribbon synapses. *Progress in retinal and eye research*, *24*, 682-720.
- Hein, K., Gadjanski, I., Kretschmar, B., Lange, K., Diem, R., Sättler, M. B., Bähr, M. (2012). An optical coherence tomography study on degeneration of retinal nerve fiber layer in rats with autoimmune optic neuritis. *Investigative ophthalmology & visual science*, *53*, 157-163.
- Herchuelz, A., Kamagate, A., Ximenes, H., & Van Eylen, F. (2007). Role of Na/Ca Exchange and the Plasma Membrane Ca²⁺-Atpase in β Cell Function and Death. *Annals of the New York Academy of Sciences*, *1099*, 456-467.
- Hibino, H., Pironkova, R., Onwumere, O., Vologodskaya, M., Hudspeth, A. J., & Lesage, F. (2002). RIM binding proteins (RBPs) couple Rab3-interacting molecules (RIMs) to voltage-gated Ca²⁺ channels. *Neuron*, *34*, 411-423.
- Hilfiker, H., Guerini, D., & Carafoli, E. (1994). Cloning and expression of isoform 2 of the human plasma membrane Ca²⁺ ATPase. Functional properties of the enzyme and its splicing products. *Journal of Biological Chemistry*, *269*, 26178-26183.
- Hirano, A. A., Morgans, C. W., & Brecha, N. C. (2007). Synaptotagmin-4 Expression in Mouse Horizontal Cells. *Investigative Ophthalmology & Visual Science*, *48*, 2798-2798.
- Hobom, M., Storch, M. K., Weissert, R., Maier, K., Radhakrishnan, A., Kramer, B., Bähr, M., Diem, R. (2004). Mechanisms and time course of neuronal degeneration in experimental autoimmune encephalomyelitis. *Brain pathology*, *14*, 148-157.
- Hofstetter, H. H., Shive, C. L., & Forsthuber, T. G. (2002). Pertussis toxin modulates the immune response to neuroantigens injected in incomplete Freund's adjuvant: induction of Th1 cells and experimental autoimmune encephalomyelitis in the presence of high frequencies of Th2 cells. *The Journal of Immunology*, *169*, 117-125.

REFERENCES

- Høglund, R. A., & Maghazachi, A. A. (2014). Multiple sclerosis and the role of immune cells. *World journal of experimental medicine*, 4, 27.
- Horstmann, L., Schmid, H., Heinen, A. P., Kurschus, F. C., Dick, H. B., & Joachim, S. C. (2013). Inflammatory demyelination induces glia alterations and ganglion cell loss in the retina of an experimental autoimmune encephalomyelitis model. *Journal of neuroinflammation*, 10, 888.
- Hundgeburth, L. C., Wunsch, M., Rovituso, D., Recks, M. S., Addicks, K., Lehmann, P. V., Kuerten, S. (2013). The complement system contributes to the pathology of experimental autoimmune encephalomyelitis by triggering demyelination and modifying the antigen-specific T and B cell response. *Clinical Immunology*, 146, 155-164.
- Hurley, J. B. (2014). *Vertebrate photoreceptors: functional molecular bases*. Springer.
- Jeong, J., VanHouten, J. N., Dann, P., Kim, W., Sullivan, C., Yu, H., Liotta, L., Espina, V., Stern, D. F., Friedman, P. A., Wysolmerski, J. J. (2016). PMCA2 regulates HER2 protein kinase localization and signaling and promotes HER2-mediated breast cancer. *Proceedings of the National Academy of Sciences of the United States of America*, 113(3), E282-90.
- Joiner, M. A., & Lee, A. (2015). Voltage-gated Cav1 channels in disorders of vision and hearing. *Current molecular pharmacology*, 8, 143-148.
- Jung, S., Oshima-Takago, T., Chakrabarti, R., Wong, A. B., Jing, Z., Yamanbaeva, G., Picher, M. M., Wojcik, S. M., Göttfert, F., Predoehl, F., Michel, K., Hell, S. W., Schoch, S., Strenzke, N., Wichmann, C., Moser, T. (2015). Rab3-interacting molecules 2 α and 2 β promote the abundance of voltage-gated CaV1.3 Ca²⁺ channels at hair cell active zones. *Proceedings of the National Academy of Sciences*, 112, E3141--E3149.
- Kaesler, P. S., & Südhof, T. C. (2005). RIM function in short-and long-term synaptic plasticity. Portland Press Limited.
- Kaesler, P. S., Deng, L., Wang, Y., Dulubova, I., Liu, X., Rizo, J., Südhof, T. C. (2011). RIM proteins tether Ca²⁺ channels to presynaptic active zones via a direct PDZ-domain interaction. *Cell*, 144, 282-295.
- Kaesler, P. S., Kwon, H.-B., Chiu, C. Q., Deng, L., Castillo, P. E., & Südhof, T. C. (2008). RIM1 α and RIM1 β are synthesized from distinct promoters of the RIM1 gene to mediate differential but overlapping synaptic functions. *Journal of Neuroscience*, 28, 13435-13447.
- Kale, N. (2016). Optic neuritis as an early sign of multiple sclerosis. *Eye and brain*, 8, 195.
- Katiyar, R., Weissgerber, P., Roth, E., Dörr, J., Sothilingam, V., Garrido, M. G., Beck, S. C., Seeliger, M. W., Beck, A., Schmitz, F., Flockerzi, V. (2015). Influence of the β 2-subunit of L-type voltage-gated Cav channels on the structural and functional development of photoreceptor ribbon synapses. *Investigative ophthalmology & visual science*, 56, 2312-2324.

REFERENCES

- Kawamoto, E. M., Vivar, C., & Camandola, S. (2012). Physiology and pathology of calcium signaling in the brain. *Frontiers in pharmacology*, 3, 61.
- Kim, M.-H., Li, G.-L., & Von Gersdorff, H. (2013). Single Ca²⁺ channels and exocytosis at sensory synapses. *The Journal of physiology*, 591, 3167-3178.
- Kiyonaka, S., Wakamori, M., Miki, T., Uriu, Y., Nonaka, M., Bito, H., Beedle, A. M., Mori, E., Hara, Y., De Waard, M., Kanagawa, M., Itakura, M., Takahashi, M., Campbell, K. P., Mori, Y. (2007). RIM1 confers sustained activity and neurotransmitter vesicle anchoring to presynaptic Ca²⁺ channels. *Nature neuroscience*, 10, 691.
- Klapper, S. D., Swiersy, A., Bamberg, E., & Buskamp, V. (2016). Biophysical properties of optogenetic tools and their application for vision restoration approaches. *Frontiers in systems neuroscience*, 10, 74.
- Kolb, H. (1995). Simple anatomy of the retina.
- Kolb, H. (2007). Gross anatomy of the eye.
- Kong, S. K., & Lee, C. Y. (1995). The use of fura 2 for measurement of free calcium concentration. *Biochemical Education*, 23, 97-98.
- Koulen, P., Fletcher, E. L., Craven, S. E., Brecht, D. S., & Wässle, H. (1998). Immunocytochemical localization of the postsynaptic density protein PSD-95 in the mammalian retina. *Journal of Neuroscience*, 18, 10136-10149.
- Krishnamoorthy, G., & Wekerle, H. (2009). EAE: an immunologist's magic eye. *European journal of immunology*, 39, 2031-2035.
- Krizaj, D. (2005). Serca isoform expression in the mammalian retina. *Experimental eye research*, 81, 690-699.
- Križaj, D. (2012). Calcium stores in vertebrate photoreceptors. In *Calcium Signaling* (pp. 873-889). Springer.
- Krizaj, D., & Copenhagen, D. R. (2002). Calcium regulation in photoreceptors. *Frontiers in bioscience: a journal and virtual library*, 7, d2023.
- Krizaj, D., Demarco, S. J., Johnson, J., Strehler, E. E., & Copenhagen, D. R. (2002). Cell-specific expression of plasma membrane calcium ATPase isoforms in retinal neurons. *Journal of Comparative Neurology*, 451, 1-21.
- Kuerten, S., & Lehmann, P. V. (2011). The immune pathogenesis of experimental autoimmune encephalomyelitis: lessons learned for multiple sclerosis? *Journal of Interferon & Cytokine Research*, 31, 907-916.

REFERENCES

- Kurnellas, M. P., Donahue, K. C., & Elkabes, S. (2007). Mechanisms of neuronal damage in multiple sclerosis and its animal models: role of calcium pumps and exchangers. Portland Press Limited.
- Laemmli, U. K. (1970). Cleavage of structural proteins during the assembly of the head of bacteriophage T4. *nature*, 227, 680.
- Lagnado, L., & Schmitz, F. (2015). Ribbon synapses and visual processing in the retina. *Annual review of vision science*, 1, 235-262.
- Lee, A., Wang, S., Williams, B., Hagen, J., Scheetz, T. E., & Haeseleer, F. (2014). Characterization of Cav1. 4 Complexes ($\alpha 1.4$, $\beta 2$, $\alpha 2\delta 4$) in HEK293T cells and in the Retina. *Journal of Biological Chemistry*, jbc--M114.
- Lenzi, D., & Von Gersdorff, H. (2001). Structure suggests function: the case for synaptic ribbons as exocytotic nanomachines. *Bioessays*, 23, 831-840.
- Li, W., Keung, J. W., & Massey, S. C. (2004). Direct synaptic connections between rods and OFF cone bipolar cells in the rabbit retina. *Journal of Comparative Neurology*, 474, 1-12.
- Liu, X., Kerov, V., Haeseleer, F., Majumder, A., Artemyev, N., Baker, S. A., Lee, A. (2013). Dysregulation of Cav1. 4 channels disrupts the maturation of photoreceptor synaptic ribbons in congenital stationary night blindness type 2. *Channels*, 7, 514-523.
- Livesey, F. J., & Cepko, C. L. (2001). Vertebrate neural cell-fate determination: lessons from the retina. *Nature Reviews Neuroscience*, 2, 109.
- LoGiudice, L., & Matthews, G. (2009). The role of ribbons at sensory synapses. *The Neuroscientist*, 15, 380-391.
- LoGiudice, L., Sterling, P., & Matthews, G. (2008). Mobility and turnover of vesicles at the synaptic ribbon. *Journal of Neuroscience*, 28, 3150-3158.
- Luo, F., Bacaj, T., & Südhof, T. C. (2015). Synaptotagmin-7 is essential for Ca^{2+} -triggered delayed asynchronous release but not for Ca^{2+} -dependent vesicle priming in retinal ribbon synapses. *Journal of Neuroscience*, 35, 11024-11033.
- Luo, F., Liu, X., Südhof, T. C., & Acuna, C. (2017). Efficient stimulus-secretion coupling at ribbon synapses requires RIM-binding protein tethering of L-type Ca^{2+} channels. *Proceedings of the National Academy of Sciences*, 114, E8081--E8090.
- Lv, C., Gould, T. J., Bewersdorf, J., & Zenisek, D. (2012). High-resolution optical imaging of zebrafish larval ribbon synapse protein RIBEYE, RIM2, and CaV 1.4 by stimulation emission depletion microscopy. *Microscopy and Microanalysis*, 18, 745-752.
- Lv, C., Stewart, W. J., Akanyeti, O., Frederick, C., Zhu, J., Santos-Sacchi, J., Sheets, L., Liao, J. C., Zenisek, D. (2016). Synaptic ribbons require ribeye for electron density, proper synaptic localization, and recruitment of calcium channels. *Cell reports*, 15, 2784-2795.

REFERENCES

- Magupalli, V. G., Schwarz, K., Alpadi, K., Natarajan, S., Seigel, G. M., & Schmitz, F. (2008). Multiple RIBEYE--RIBEYE interactions create a dynamic scaffold for the formation of synaptic ribbons. *Journal of Neuroscience*, *28*, 7954-7967.
- Mansergh, F., Orton, N. C., Vessey, J. P., Lalonde, M. R., Stell, W. K., Tremblay, F., Barnes, S., Rancourt, D. E., Bech-Hansen, N. T. (2005). Mutation of the calcium channel gene *Cacna1f* disrupts calcium signaling, synaptic transmission and cellular organization in mouse retina. *Human molecular genetics*, *14*, 3035-3046.
- Martínez-Lapiscina, E. H., Sanchez-Dalmau, B., Fraga-Pumar, E., Ortiz-Perez, S., Tercero-Urbe, A. I., Torres-Torres, R., Villoslada, P. (2014). The visual pathway as a model to understand brain damage in multiple sclerosis. *Multiple Sclerosis Journal*, *20*, 1678-1685.
- Masland, R. H. (2001). The fundamental plan of the retina. *Nature neuroscience*, *4*, 877.
- Matsui, M. (2008). Multiple sclerosis immunology for clinicians. *Neurology Asia*, *13*, 195-198.
- Matthews, G., & Fuchs, P. (2010). The diverse roles of ribbon synapses in sensory neurotransmission. *Nature Reviews Neuroscience*, *11*, 812.
- Matthews, P. M., Roncaroli, F., Waldman, A., Sormani, M. P., De Stefano, N., Giovannoni, G., Reynolds, R. (2016). A practical review of the neuropathology and neuroimaging of multiple sclerosis. *Practical neurology*, *16*, 279-287.
- Mauleon, G., Lo, J. F., Peterson, B. L., Fall, C. P., & Eddington, D. T. (2013). Enhanced loading of Fura-2/AM calcium indicator dye in adult rodent brain slices via a microfluidic oxygenator. *Journal of neuroscience methods*, *216*, 110-117.
- Maxeiner, S., Luo, F., Tan, A., Schmitz, F., & Südhof, T. C. (2016). How to make a synaptic ribbon: RIBEYE deletion abolishes ribbons in retinal synapses and disrupts neurotransmitter release. *The EMBO journal*, *35*, 1098-1114.
- Mayor, H. D., Hampton, J. C., & Rosario, B. (1961). A simple method for removing the resin from epoxy-embedded tissue. *The Journal of biophysical and biochemical cytology*, *9*, 909.
- McRory, J. E., Hamid, J., Doering, C. J., Garcia, E., Parker, R., Hamming, K., Chen, L., Hildebrand, M., Beedle, A. M., Feldcamp, L., Zamponi, G. W., Snutch, T. P. (2004). The *CACNA1F* gene encodes an L-type calcium channel with unique biophysical properties and tissue distribution. *Journal of Neuroscience*, *24*, 1707-1718.
- Mecha, M., Carrillo-Salinas, F. J., Mestre, L., Feliu, A., & Guaza, C. (2013). Viral models of multiple sclerosis: neurodegeneration and demyelination in mice infected with Theiler's virus. *Progress in neurobiology*, *101*, 46-64.
- Mehling, M., Johnson, T. A., Antel, J., Kappos, L., & Bar-Or, A. (2011). Clinical immunology of the sphingosine 1-phosphate receptor modulator fingolimod (FTY720) in multiple sclerosis. *Neurology*, *76*, S20--S27.

REFERENCES

- Mercer, A. J., & Thoreson, W. B. (2011). The dynamic architecture of photoreceptor ribbon synapses: cytoskeletal, extracellular matrix, and intramembrane proteins. *Visual neuroscience*, *28*, 453-471.
- Miller, S. D., Karpus, W. J., & Davidson, T. S. (2007). Experimental autoimmune encephalomyelitis in the mouse. *Current protocols in immunology*, *88*, 15-1.
- Minagar, A., & Alexander, J. S. (2003). Blood-brain barrier disruption in multiple sclerosis. *Multiple Sclerosis Journal*, *9*, 540-549.
- Mix, E., Meyer-Rienecker, H., Hartung, H.-P., & Zettl, U. K. (2010). Animal models of multiple sclerosis potentials and limitations. *Progress in neurobiology*, *92*, 386-404.
- Molnar, T., Barabas, P., Birnbaumer, L., Punzo, C., Kefalov, V., & Križaj, D. (2012). Store-operated channels regulate intracellular calcium in mammalian rods. *The Journal of physiology*, *590*, 3465-3481.
- Morgans, C. W. (2000). Neurotransmitter release at ribbon synapses in the retina. *Immunology and cell biology*, *78*, 442.
- Morgans, C. W. (2001). Localization of the $\alpha 1F$ calcium channel subunit in the rat retina. *Investigative Ophthalmology & Visual Science*, *42*, 2414-2418.
- Morgans, C. W., Bayley, P. R., Oesch, N. W., Ren, G., Akileswaran, L., & Taylor, W. R. (2005). Photoreceptor calcium channels: insight from night blindness. *Visual neuroscience*, *22*, 561-568.
- Morgans, C. W., El Far, O., Berntson, A., Wässle, H., & Taylor, W. R. (1998). Calcium extrusion from mammalian photoreceptor terminals. *Journal of Neuroscience*, *18*, 2467-2474.
- Moser, T., Brandt, A., & Lysakowski, A. (2006). Hair cell ribbon synapses. *Cell and tissue research*, *326*, 347-359.
- Mukherjee, K., Yang, X., Gerber, S. H., Kwon, H.-B., Ho, A., Castillo, P. E., Liu, X., Südhof, T. C. (2010). Piccolo and bassoon maintain synaptic vesicle clustering without directly participating in vesicle exocytosis. *Proceedings of the National Academy of Sciences*, *107*, 6504-6509.
- Neher, E., & Sakaba, T. (2008). Multiple roles of calcium ions in the regulation of neurotransmitter release. *Neuron*, *59*, 861-872.
- Nicot, A., Kurnellas, M., & Elkabes, S. (2005). Temporal pattern of plasma membrane calcium ATPase 2 expression in the spinal cord correlates with the course of clinical symptoms in two rodent models of autoimmune encephalomyelitis. *European Journal of Neuroscience*, *21*, 2660-2670.
- Nicot, A., Ratnakar, P. V., Ron, Y., Chen, C.-C., & Elkabes, S. (2003). Regulation of gene expression in experimental autoimmune encephalomyelitis indicates early neuronal dysfunction. *Brain*, *126*, 398-412.

REFERENCES

- Oberwahrenbrock, T., Ringelstein, M., Jentschke, S., Deuschle, K., Klumbies, K., Bellmann-Strobl, J., Harmel, J., Ruprecht, K., Schippling, S., Hartung, H. P., Aktas, O., Brandt, A. U., Paul, F. (2013). Retinal ganglion cell and inner plexiform layer thinning in clinically isolated syndrome. *Multiple Sclerosis Journal*, *19*, 1887-1895.
- Ortiz, G. G., Pacheco-Moisés, F. P., Macías-Islas, M. Á., Flores-Alvarado, L. J., Mireles-Ramírez, M. A., González-Renovato, E. D., Hernández-Navarro, V. E., Sánchez-López, A. L., Alatorre-Jiménez, M. A. (2014). Role of the blood--brain barrier in multiple sclerosis. *Archives of medical research*, *45*, 687-697.
- Pang, J.-J., Yang, Z., Jacoby, R. A., & Wu, S. M. (2018). Cone synapses in mammalian retinal rod bipolar cells. *Journal of Comparative Neurology*.
- Pangrsic, T., Singer, J. H., & Koschak, A. (2018). Voltage-gated calcium channels: Key players in sensory coding in the retina and the inner ear. *Physiological reviews*, *98*, 2063-2096.
- Parsons, T. D., & Sterling, P. (2003). Synaptic ribbon: conveyor belt or safety belt? *Neuron*, *37*, 379-382.
- Petracca, M., Cordano, C., Cellerino, M., Button, J., Krieger, S., Vancea, R., Ghassemi, R., Farrell, C., Miller, A., Calabresi, P. A., Lublin, F., Inglese, M. (2017). Retinal degeneration in primary-progressive multiple sclerosis: a role for cortical lesions? *Multiple Sclerosis Journal*, *23*, 43-50.
- Petzold, A., Balcer, L. J., Calabresi, P. A., Costello, F., Frohman, T. C., Frohman, E. M., Martinez-Lapiscina, E. H., Green, A. J., Kardon, R., Outteryck, O., Paul, F., Schippling, S., Vermersch, P., Villoslada, P., Balk, L. J., ERN-EYE IMSVISUAL. (2017). Retinal layer segmentation in multiple sclerosis: a systematic review and meta-analysis. *The Lancet Neurology*, *16*, 797-812.
- Popova, E. (2014). ON-OFF Interactions in the Retina: Role of Glycine and GABA. *Current neuropharmacology*, *12*, 509-526.
- Punge, A., Rizzoli, S. O., Jahn, R., Wildanger, J. D., Meyer, L., Schönle, A., Kastrop, L., Hell, S. W. (2008). 3D reconstruction of high-resolution STED microscope images. *Microscopy research and technique*, *71*, 644-650.
- Purves, D., Augustine, G. J., Fitzpatrick, D., Katz, L. C., LaMantia, A.-S., McNamara, J. O., Williams, S. M. (2001). *Neuroscience*. Sunderland, MA: Sinauer Associates.
- Rabl, K., & Thoreson, W. B. (2002). Calcium-dependent inactivation and depletion of synaptic cleft calcium ions combine to regulate rod calcium currents under physiological conditions. *European Journal of Neuroscience*, *16*, 2070-2077.
- Raviola, E., & Gilula, N. B. (1975). Intramembrane organization of specialized contacts in the outer plexiform layer of the retina. A freeze-fracture study in monkeys and rabbits. *The Journal of Cell Biology*, *65*, 192-222.

REFERENCES

- Regus-Leidig, H., Ott, C., Löhner, M., Atorf, J., Fuchs, M., Sedmak, T., Kremers, J., Fejtová, A., Gundelfinger, E. D., Brandstätter, J. H. (2013). Identification and immunocytochemical characterization of Piccolino, a novel Piccolo splice variant selectively expressed at sensory ribbon synapses of the eye and ear. *PLoS One*, *8*, e70373.
- Rieke, F., & Schwartz, E. A. (1996). Asynchronous transmitter release: control of exocytosis and endocytosis at the salamander rod synapse. *The Journal of Physiology*, *493*, 1-8.
- Robinson, A. P., Harp, C. T., Noronha, A., & Miller, S. D. (2014). The experimental autoimmune encephalomyelitis (EAE) model of MS: utility for understanding disease pathophysiology and treatment. In *Handbook of clinical neurology* (Vol. 122, pp. 173-189). Elsevier.
- Saidha, S., Syc, S. B., Ibrahim, M. A., Eckstein, C., Warner, C. V., Farrell, S. K., Oakley, J. D., Durbin, M. K., Meyer, S. A., Balcer, L. J., Frohman, E. M., Rosenzweig, J. M., Newsome, S. D., Ratchford, J. N., Nguyen, Q. D., Calabresi, P. A. (2011). Primary retinal pathology in multiple sclerosis as detected by optical coherence tomography. *Brain*, *134*, 518-533.
- Sakai, H., & Naka, K.-I. (1983). Synaptic organization involving receptor, horizontal and on-and off-center bipolar cells in the catfish retina. *Vision research*, *23*, 339-351.
- Schermelleh, L., Heintzmann, R., & Leonhardt, H. (2010). A guide to super-resolution fluorescence microscopy. *The Journal of cell biology*, *190*, 165-175.
- Schmitz, F. (2009). The making of synaptic ribbons: how they are built and what they do. *The Neuroscientist*, *15*, 611-624.
- Schmitz, F. (2014). Presynaptic [Ca²⁺] and GCAPs: aspects on the structure and function of photoreceptor ribbon synapses. *Frontiers in molecular neuroscience*, *7*, 3.
- Schmitz, F., Königstorfer, A., & Südhof, T. C. (2000). RIBEYE, a component of synaptic ribbons: a protein's journey through evolution provides insight into synaptic ribbon function. *Neuron*, *28*, 857-872.
- Schmitz, Y., & Witkovsky, P. (1997). Dependence of photoreceptor glutamate release on a dihydropyridine-sensitive calcium channel. *Neuroscience*, *78*, 1209-1216.
- Schoch, S., Mittelstaedt, T., Kaeser, P. S., Padgett, D., Feldmann, N., Chevaleyre, V., Castillo, P. E., Hammer, R. E., Han, W., Schmitz, F., Lin, W., Südhof, T. C. (2006). Redundant functions of RIM1 α and RIM2 α in Ca²⁺-triggered neurotransmitter release. *The EMBO journal*, *25*, 5852-5863.
- Sheets, L., Trapani, J. G., Mo, W., Obholzer, N., & Nicolson, T. (2011). Ribeye is required for presynaptic CaV1.3 channel localization and afferent innervation of sensory hair cells. *Development*, *138*, 1309-1319.

REFERENCES

- Shibasaki, T., Sunaga, Y., Fujimoto, K., Kashima, Y., & Seino, S. (2003). Interaction of ATP sensor, cAMP sensor, Ca²⁺ sensor, and voltage-dependent calcium channel in insulin granule exocytosis. *Journal of Biological Chemistry*.
- Shichida, Y., & Matsuyama, T. (2009). Evolution of opsins and phototransduction. *Philosophical Transactions of the Royal Society B: Biological Sciences*, 364, 2881-2895.
- Shindler, K. S., Ventura, E., Dutt, M., & Rostami, A. (2008). Inflammatory demyelination induces axonal injury and retinal ganglion cell apoptosis in experimental optic neuritis. *Experimental eye research*, 87, 208-213.
- Skundric, D. S. (2005). Experimental models of relapsing-remitting multiple sclerosis: current concepts and perspective. *Current neurovascular research*, 2, 349-362.
- Spiwoks-Becker, I., Maus, C., Tom Dieck, S., Fejtová, A., Engel, L., Wolloscheck, T., Wolfrum, U., Vollrath, L., Spessert, R. (2008). Active zone proteins are dynamically associated with synaptic ribbons in rat pinealocytes. *Cell and tissue research*, 333, 185.
- Stenkamp, D. L. (2015). Development of the vertebrate eye and retina. In *Progress in molecular biology and translational science* (Vol. 134, pp. 397-414). Elsevier.
- Sterling, P., & Matthews, G. (2005). Structure and function of ribbon synapses. *Trends in neurosciences*, 28, 20-29.
- Stojic, A., Bojcevski, J., Williams, S. K., Diem, R., & Fairless, R. (2018). Early nodal and paranodal disruption in autoimmune optic neuritis. *Journal of Neuropathology & Experimental Neurology*, 77, 361-373.
- Striessnig, J., Pinggera, A., Kaur, G., Bock, G., & Tuluc, P. (2014). L-type Ca²⁺ channels in heart and brain. *Wiley Interdisciplinary Reviews: Membrane Transport and Signaling*, 3, 15-38.
- Strom, T. M., Nyakatura, G., Apfelstedt-Sylla, E., Hellebrand, H., Lorenz, B., Weber, B. H., Wutz, K., Gutwillinger, N., Rüther, K., Drescher, B., Sauer, C., Zrenner, E., Meitinger, T., Rosenthal, A., Meindl, A. (1998). An L-type calcium-channel gene mutated in incomplete X-linked congenital stationary night blindness. *Nature genetics*, 19, 260.
- Südhof, T. C. (2012). Calcium control of neurotransmitter release. *Cold Spring Harbor perspectives in biology*, 4, a011353.
- Südhof, T. C. (2012). The presynaptic active zone. *Neuron*, 75, 11-25.
- Sung, C.-H., & Chuang, J.-Z. (2010). The cell biology of vision. *The Journal of cell biology*, 190, 953-963.
- Suryanarayanan, A., & Slaughter, M. M. (2006). Synaptic transmission mediated by internal calcium stores in rod photoreceptors. *Journal of Neuroscience*, 26, 1759-1766.

REFERENCES

- Szikra, T., & Križaj, D. (2006). The dynamic range and domain-specific signals of intracellular calcium in photoreceptors. *Neuroscience*, *141*, 143-155.
- Szikra, T., & Križaj, D. (2007). Intracellular organelles and calcium homeostasis in rods and cones. *Visual neuroscience*, *24*, 733-743.
- Szikra, T., Barabas, P., Bartoletti, T. M., Huang, W., Akopian, A., Thoreson, W. B., Krizaj, D. (2009). Calcium homeostasis and cone signaling are regulated by interactions between calcium stores and plasma membrane ion channels. *PLoS One*, *4*, e6723.
- Tahoun, I. S. (2015). Automatic Discrimination of Color Retinal Images using the Bag of Words Approach.
- Tatomir, A., Talpos-Caia, A., Anselmo, F., Kruszewski, A. M., Boodhoo, D., Rus, V., Rus, H. (2017). The complement system as a biomarker of disease activity and response to treatment in multiple sclerosis. *Immunologic research*, *65*, 1103-1109.
- Thoreson, W. B. (2007). Kinetics of synaptic transmission at ribbon synapses of rods and cones. *Molecular neurobiology*, *36*, 205-223.
- Thoreson, W. B., Rabl, K., Townes-Anderson, E., & Heidelberger, R. (2004). A highly Ca²⁺-sensitive pool of vesicles contributes to linearity at the rod photoreceptor ribbon synapse. *Neuron*, *42*, 595-605.
- Tigno-Aranjuez, J. T., Jaini, R., Tuohy, V. K., Lehmann, P. V., & Tary-Lehmann, M. (2009). Encephalitogenicity of complete Freund's adjuvant relative to CpG is linked to induction of Th17 cells. *The Journal of Immunology*, *183*, 5654-5661.
- Torkildsen, Ø., Brunborg, L. A., Myhr, K.-M., & Bø, L. (2008). The cuprizone model for demyelination. *Acta Neurologica Scandinavica*, *117*, 72-76.
- Trapp, B. D., & Nave, K.-A. (2008). Multiple sclerosis: an immune or neurodegenerative disorder? *Annu. Rev. Neurosci.*, *31*, 247-269.
- Ullrich, B., & Südhof, T. C. (1994). Distribution of synaptic markers in the retina: implications for synaptic vesicle traffic in ribbon synapses. *Journal of Physiology-Paris*, *88*, 249-257.
- Vaithianathan, T., & Matthews, G. (2014). Visualizing synaptic vesicle turnover and pool refilling driven by calcium nanodomains at presynaptic active zones of ribbon synapses. *Proceedings of the National Academy of Sciences*, *111*, 8655-8660.
- Van Hook, M. J., & Thoreson, W. B. (2014). Endogenous calcium buffering at photoreceptor synaptic terminals in salamander retina. *Synapse*, *68*, 518-528.
- Van Hook, M. J., & Thoreson, W. B. (2015). Weak endogenous Ca²⁺ buffering supports sustained synaptic transmission by distinct mechanisms in rod and cone photoreceptors in salamander retina. *Physiological reports*, *3*.

REFERENCES

- Verkhatsky, A. (2002). The endoplasmic reticulum and neuronal calcium signalling. *Cell calcium*, *32*, 393-404.
- Von Gersdorff, H. (2001). Synaptic ribbons: versatile signal transducers. *Neuron*, *29*, 7-10.
- Von Gersdorff, H., & Mathews, G. (1994). Dynamics of synaptic vesicle fusion and membrane retrieval in synaptic terminals. *Nature*, *367*, 735.
- Von Kriegstein, K., Schmitz, F., Link, E., & Südhof, T. C. (1999). Distribution of synaptic vesicle proteins in the mammalian retina identifies obligatory and facultative components of ribbon synapses. *European Journal of Neuroscience*, *11*, 1335-1348.
- Wahl, S., Katiyar, R., & Schmitz, F. (2013). A local, periaxial zone endocytic machinery at photoreceptor synapses in close vicinity to synaptic ribbons. *Journal of Neuroscience*, *33*, 10278-10300.
- Wahl, S., Magupalli, V. G., Dembla, M., Katiyar, R., Schwarz, K., Köblitz, L., Alpadi, K., Krause, E., Rettig, J., Sung, C. H., Goldberg, A. F., Schmitz, F. (2016). The disease protein Tulp1 is essential for periaxial zone endocytosis in photoreceptor ribbon synapses. *Journal of Neuroscience*, *36*, 2473-2493.
- Wahl-Schott, C., Baumann, L., Cuny, H., Eckert, C., Griessmeier, K., & Biel, M. (2006). Switching off calcium-dependent inactivation in L-type calcium channels by an autoinhibitory domain. *Proceedings of the National Academy of Sciences*, *103*, 15657-15662.
- Wallace, V. A. (2011). Concise review: making a retina from the building blocks to clinical applications. *Stem Cells*, *29*, 412-417.
- Wan, L., Almers, W., & Chen, W. (2005). Two ribeye genes in teleosts: the role of Ribeye in ribbon formation and bipolar cell development. *Journal of Neuroscience*, *25*, 941-949.
- Wang, Y., & Südhof, T. C. (2003). Genomic definition of RIM proteins: evolutionary amplification of a family of synaptic regulatory proteins. *Genomics*, *81*, 126-137.
- Wang, Y., Fehlhaber, K. E., Sarria, I., Cao, Y., Ingram, N. T., Guerrero-Given, D., Throesch, B., Baldwin, K., Kamasawa, N., Ohtsuka, T., Sampath, A. P., Martemyanov, K. A. (2017). The auxiliary calcium channel subunit $\alpha 2\delta 4$ is required for axonal elaboration, synaptic transmission, and wiring of rod photoreceptors. *Neuron*, *93*, 1359-1374.
- Wang, Y., Okamoto, M., Schmitz, F., Hofmann, K., & Südhof, T. C. (1997). Rim is a putative Rab3 effector in regulating synaptic-vesicle fusion. *Nature*, *388*, 593.
- Wässle, H. (2004). Parallel processing in the mammalian retina. *Nature Reviews Neuroscience*, *5*, 747.
- Wigler, M., Silverstein, S., Lee, L.-S., Pellicer, A., Cheng, Y.-c., & Axel, R. (1977). Transfer of purified herpes virus thymidine kinase gene to cultured mouse cells. *Cell*, *11*, 223-232.

REFERENCES

- Williams, S. K., Fairless, R., Weise, J., Kalinke, U., Schulz-Schaeffer, W., & Diem, R. (2011). Neuroprotective effects of the cellular prion protein in autoimmune optic neuritis. *The American journal of pathology*, *178*, 2823-2831.
- Willoughby, C. E., Ponzin, D., Ferrari, S., Lobo, A., Landau, K., & Omid, Y. (2010). Anatomy and physiology of the human eye: effects of mucopolysaccharidosis disease on structure and function--a review. *Clinical & Experimental Ophthalmology*, *38*, 2-11.
- Wohrer, A. (2008). *The vertebrate retina: A functional review*. Ph.D. dissertation, INRIA.
- Wu, S. M. (2010). Synaptic organization of the vertebrate retina: general principles and species-specific variations: the Friedenwald lecture. *Investigative ophthalmology & visual science*, *51*, 1264-1274.
- Wutz, K., Sauer, C., Zrenner, E., Lorenz, B., Alitalo, T., Broghammer, M., Hergersberg, M., de la Chapelle, A., Weber, B. H., Wissinger, B., Meindl, A., Pusch, C. M. (2002). Thirty distinct CACNA1F mutations in 33 families with incomplete type of XLCSNB and Cacna1f expression profiling in mouse retina. *European Journal of Human Genetics*, *10*, 449.
- Wycisk, K. A., Budde, B., Feil, S., Skosyrski, S., Buzzi, F., Neidhardt, J., Glaus, E., Nürnberg, P., Ruether, K., Berger, W. (2006). Structural and functional abnormalities of retinal ribbon synapses due to Cacna2d4 mutation. *Investigative ophthalmology & visual science*, *47*, 3523-3530.
- Wycisk, K. A., Zeitz, C., Feil, S., Wittmer, M., Forster, U., Neidhardt, J., Wissinger, B., Zrenner, E., Wilke, R., Kohl, S., Berger, W. (2006). Mutation in the auxiliary calcium-channel subunit CACNA2D4 causes autosomal recessive cone dystrophy. *The American Journal of Human Genetics*, *79*, 973-977.
- Xing, W., Akopian, A., & Križaj, D. (2012). Trafficking of presynaptic PMCA signaling complexes in mouse photoreceptors requires Cav1.4 α 1 subunits. In *Retinal Degenerative Diseases* (pp. 739-744). Springer.
- Yang, J., Pawlyk, B., Wen, X.-H., Adamian, M., Soloviev, M., Michaud, N., Zhao, Y., Sandberg, M. A., Makino, C. L., Li, T. (2007). Mpp4 is required for proper localization of plasma membrane calcium ATPases and maintenance of calcium homeostasis at the rod photoreceptor synaptic terminals. *Human molecular genetics*, *16*, 1017-1029.
- Yau, K.-W., & Hardie, R. C. (2009). Phototransduction motifs and variations. *Cell*, *139*, 246-264.
- You, Y., Graham, E. C., Shen, T., Yiannikas, C., Parratt, J., Gupta, V., Barton, J., Dwyer, M., Barnett, M. H., Fraser, C. L., Graham, S. L., Klistorner, A. (2018). Progressive inner nuclear layer dysfunction in non-optic neuritis eyes in MS. *Neurology-Neuroimmunology Neuroinflammation*, *5*, e427.
- Young, R. W. (1985). Cell differentiation in the retina of the mouse. *The Anatomical Record*, *212*, 199-205.

REFERENCES

- Zabouri, N., & Haverkamp, S. (2013). Calcium channel-dependent molecular maturation of photoreceptor synapses. *PLoS One*, *8*, e63853.
- Zanazzi, G., & Matthews, G. (2009). The molecular architecture of ribbon presynaptic terminals. *Molecular neurobiology*, *39*, 130-148.
- Zenisek, D., & Matthews, G. (2000). The role of mitochondria in presynaptic calcium handling at a ribbon synapse. *Neuron*, *25*, 229-237.
- Zenisek, D., Davila, V., Wan, L., & Almers, W. (2003). Imaging calcium entry sites and ribbon structures in two presynaptic cells. *Journal of Neuroscience*, *23*, 2538-2548.
- Zhu, B., Luo, L., Moore, G. R., Paty, D. W., & Cynader, M. S. (2003). Dendritic and synaptic pathology in experimental autoimmune encephalomyelitis. *The American journal of pathology*, *162*, 1639-1650.
- Ziemssen, T., & Ziemssen, F. (2005). The role of the humoral immune system in multiple sclerosis (MS) and its animal model experimental autoimmune encephalomyelitis (EAE). *Autoimmunity reviews*, *4*, 460-467.

6 LIST OF FIGURES

Figure 1: Section through the adult human eye.....	6
Figure 2: Histological image and schematic diagram of retinal layers of an adult mammalian retina	8
Figure 3: Phototransduction cascade in vertebrate rod photoreceptors.....	9
Figure 4: Rod and cone synaptic pathways in mammalian retina (on/off pathways)	11
Figure 5: Rod photoreceptor ribbon synapses.....	12
Figure 6: Various types of ribbons	13
Figure 7: Detailed schematic diagrams of rod photoreceptor terminal	14
Figure 8: Molecular architecture of a retinal ribbon synapse.....	16
Figure 9: Molecular structure of RIM proteins.....	18
Figure 10: Molecular architecture of Ca_v channel complex	19
Figure 11: Domain structure of $Ca_v\beta$ and $Ca_v\alpha2\delta$ subunits.....	20
Figure 12: Key players of calcium homeostasis maintenance at ribbon presynaptic terminals.....	22
Figure 13: Immunopathogenesis of multiple sclerosis (MS).....	24
Figure 14: Illustration of type of Th cells and cytokines induced by neuroantigens in various adjuvants.....	26
Figure 15: EAE induction through neuroantigen mediated differentiation of CD4+ T cells	27
Figure 16: Time course of EAE (days post immunization vs average clinical EAE score)	30
Figure 17: $Ca_v1.4\alpha$ C-term expression in retinal sections of CFA and MOG/CFA injected mice	55
Figure 18: Immunolabeling of $Ca_v1.4\alpha$ N-term in retinal sections of CFA- and MOG/CFA-injected mice	56
Figure 19: Quantification of $Ca_v1.4$ N-term in retinal sections of CFA- and MOG/CFA-injected mice	57
Figure 20: Contour length analyses of $Ca_v1.4\alpha$ C-term punctas in CFA and MOG/CFA injected mice retina.....	58
Figure 21: Western blot analyses for $Ca_v1.4$ N-term in CFA and MOG/CFA injected mice retinal lysates.....	59
Figure 22: $Ca_v\beta2$ (No.1) immunolabeling and analyses in CFA and MOG/CFA mice retinal sections	61
Figure 23: Analyses of $Ca_v\beta2$ (No.2) in CFA and MOG/CFA injected mice retinal sections	62
Figure 24: SR-SIM images of $Ca_v\beta2$ (No.1) punctas in CFA and MOG/CFA injected mice retinal sections.....	63
Figure 25: Contour-length analyses of $Ca_v\beta2$ (No.1) punctas in CFA and MOG/CFA mice retinal sections.....	64

LIST OF FIGURES

Figure 26: Western blot analyses for Ca _v β2 (No.2) antibody in EAE mice retinal lysates	65
Figure 27: Fura2-AM recordings of CFA and MOG/ CFA mice retinal slices on day 9 after injection	66
Figure 28: Fura2-AM analyses of CFA and MOG/CFA mice retinal slices on day 9 after immunization	67
Figure 29: Fura2-AM measurements in CFA and MOG/CFA injected mice retina on day 7 after injection.....	68
Figure 30: Fura2-AM measurements in CFA and MOG/CFA mice retinal slices on day 8 after injection.....	69
Figure 31: Comparison of Ca ²⁺ influx amplitudes and kinetics in MOG/CFA injected mice retinal slices over days 7 to 9 after immunization	70
Figure 32: Depolarization–evoked Ca ²⁺ influx measurements in commercial CFA and MOG/CFA injected mice retinal slices.....	71
Figure 33: Fura2-AM measurements in commercial CFA and MOG/CFA injected mice retinas on days 7, 8 and 9 after immunization.....	72
Figure 34: Comparing Ca ²⁺ influx amplitudes and kinetics in Hooke’s MOG ₃₅₋₅₅ injected mice retinal slices over days 7 to 9 after injection	73
Figure 35: Immunolabeling of RIM2 (4F7) and PSD95 in EAE retinal sections	75
Figure 36: Quantification of RIM2 (4F7) and PSD95 immunosignals in CFA and MOG/CFA mice retinas.....	76
Figure 37: RIM2 (4C6) immunolabeling and quantification in CFA and MOG/CFA mice retinal sections	77
Figure 38: Western blot analyses of RIM1,2 on EAE mice retinal lysates.....	79
Figure 39: Baseline ratiometric (340/380) FURA2 fluorescence comparison between self-made MOG/CFA and CFA-injected mice retinal slices	80
Figure 40: Comparing baseline ratiometric (340/380) fluorescence of FURA2 in retinal slices of mice induced with Hooke’s laboratories EAE induction kit	81
Figure 41: PMCA1/ PSD95 double immunolabeling in CFA and MOG/CFA injected mice retinal sections	82
Figure 42: PMCA2/PSD95 coimmunolabeled on CFA and MOG/CFA injected mice retinal sections	83
Figure 43: Quantification of PMCA1 and PMCA2 immunosignals in CFA and MOG/CFA retinal sections.....	84
Figure 44: Ca _v 1.4 alpha N-term is coimmunolabeled with monoclonal anti-RIBEYE antibody on WT and Ca _v 1.4 KO mice retinal sections	85

LIST OF FIGURES

Figure 45: Double immunolabeling of Ca _v 1.4 alpha C-term with monoclonal RIBEYE antibody on WT and Ca _v 1.4 KO mice retinal sections	86
Figure 46: Double immunolabeling of Ca _v β2 (No.1) and SV2 on WT and Ca _v β2 KO mice retinal sections	87
Figure 47: Immunolabeling of Ca _v β2 (No.2) and SV2 on WT and Ca _v β2 KO mice retinal sections	88
Figure 48: RIM2 (4F7) blocked with control and antigenic peptide is co-immunolabeled with polyclonal anti-RIBEYE antibody on WT mice retinal sections	89
Figure 49: RIM2 (4C6) blocked with control and antigenic peptide is co-immunolabeled with polyclonal anti-RIBEYE antibody on WT mice retinal sections	89
Figure 50: Western blot of RIM1,2 polyclonal antibody on RIM2 transfected HEK293T cell lysates	90

7 LIST OF ABBREVIATIONS

μl	microlitre
μM	micromolar
μm	micrometre
°C	degree Celsius
a/ A	amacrine cells
ad	arciform density
AID	α-interacting domain
AM	acetoxy-methyl group
AON	acute optic neuritis
APC	antigen presenting cells
APS	ammonium persulphate
AZ	active zone
b/ B	bipolar cells
BBB	blood brain barrier
BSA	bovine serum albumin
C	terminal carboxyl group/ cone photoreceptor cells
Ca ²⁺	calcium-ion
CaBP	calcium binding protein
CAST1	CAZ-associated structural protein 1
CAZ	cytomatrix active zone
CBC	cone bipolar cells
CD	cluster of differentiation
CFA	complete Freund's adjuvant
CICR	calcium induced calcium release
CMV	cytomegalovirus
CNS	central nervous system
CtBP1	C-terminal Binding Protein 1
CtBP2	C-terminal Binding Protein 2
DDSA	Dodecanyl Succinic Anhydride
DMEM	Dulbecco's modified Eagle's medium
DMSO	dimethyl sulphoxide

LIST OF ABBREVIATIONS

DTH	delayed type hypersensitivity
EAE	experimental autoimmune encephalitis
ECL	Enhanced chemoluminescence
ERC2	ELKS/Rab6-interacting/CAST family member 2
EDTA	ethylene diamine tetra-acetic acid
ELKS	Rab6-interacting/CAST family member 2
ER	endoplasmic reticulum
ERG	electroretinogram
GC	ganglion cell
GCL	ganglion cell layer
cGMP	cyclic guanosine monophosphate
GMP/ GDP/ GTP	guanosine mono/ di/ tri-phosphate
GM-CSF	granulocyte/monocyte colony-stimulating factor
h/ H/ HC	horizontal cells
HBBS	Hank's balanced salt solution
HEPES	(4-(2-hydroxyethyl)-1-piperazineethanesulfonic acid
HRP	horseradish peroxidase
HVA	high voltage activated
i-CSNB	incomplete congenital stationary blindness
IFA	incomplete Freund's adjuvant
IFN	interferon
IL	interleukin
INL	inner nuclear layer
igluR	ionotropic glutamate receptor
IPL	inner plexiform layer
IP3R	inositol 1,4,5-triphosphate receptor
IS	inner segments
iTreg	induced T regulatory cells
KCl	potassium chloride
KIF	kinesin family member
KO	knock out
LCS	low calcium solution
LVA	low voltage activated

LIST OF ABBREVIATIONS

m/ M	müller glial cells
Mac	macrophage
MBP	myelin basic protein
MCP	macrophage/monocyte chemoattractant protein
MHC	major histocompatibility complex
MOG	myelin oligodendrocytic glycoprotein
mg	milligramm
mV	millivolt
mgluR	metabotropic glutamate receptor
Munc 119	Mammalian Uncoordinated 119
MS	multiple sclerosis
Na	sodium
NCX	sodium/ calcium exchanger
NF	nerve fibre layer
NK	natural killer cells
NPG	n-Propylgallate
NSF	N-ethylmaleimide sensitive fusion protein
nm	nano metre
OCT	optical coherence tomography
OLG	oligodendrocytes
ONL	outer nuclear layer
ON	optic neuritis
OPL	outer plexiform layer
OS	outer segments
PBS	phosphate buffer saline
PBST	phosphate buffer saline-Tween
PDE	phosphodiesterase
PLP	proteolipid protein
pm	presynaptic plasma membrane
PMCA	plasma membrane calcium ATPases
PMT	photo multiplier tube
PPMS	primary progressive multiple sclerosis
pre	presynaptic terminal

LIST OF ABBREVIATIONS

PTX	pertussis toxin
r/ R	rod photoreceptor cells
RBC	rod bipolar cells
RGC	retinal ganglion cell
RGCl	retinal ganglion cell layer
RIM	Rab3 interacting molecule
RNFL	retinal nerve fibre layer
ROI	region of interest
RPE	retinal pigment epithelium
RRMS	relapsing remitting MS
RRP	readily releasable pool
RS	resting solution
RyR	ryanodine receptors
SDS	sodium do-decyl sulfate
SERCA	smooth endoplasmic reticulum calcium ATPases
SOCE	store operated calcium entry
SPMS	secondary progressive multiple sclerosis
SRP	slow releasable pool
SV	synaptic vesicle
SR	synaptic ribbon
SR-SIM	super resolution structured illumination microscopy
STIM	Stromal interaction molecule
t	time constant
T	transducin
Th	T helper cells
TNFR	tumor necrosis factor receptor
TRPC	transient receptor potential <u>cation channels</u>
t-SNARE	target-Soluble (<u>NSF</u> Attachment Protein) receptor
v	voltage
VEP	visual evoked potential
VGCC	voltage gated calcium channel
v-SNARE	vesicle-Soluble (<u>NSF</u> Attachment Protein) receptor
Wt	Wild type

For data protection reasons, the curriculum vitae will not be published in the electronic version of the dissertation.

Day of Promotion: 24.10.2019

Dean: Prof. Dr. M.D. Menger

Reviewers: Prof. Dr. J. Rettig

Prof. Dr. F. Schmitz